Measuring Radio Emission from Cosmic Ray Air Showers with a Digital Radio Telescope

Dissertation

zur

Erlangung des Doktorgrades (Dr. rer. nat.)

der

Mathematisch-Naturwissenschaftlichen Fakultät

der

Rheinischen Friedrich-Willhelms-Universität Bonn

vorgelegt von

Andreas Horneffer

aus

Koblenz

Bonn 2006

Angefertigt mit Genehmigung der Mathematisch-Naturwissenschaftlichen Fakultät
der Rheinischen Friedrich-Wilhelms-Universität Bonn.

1. Referent: Prof. Dr. Heino Falcke
2. Referent: Prof. Dr. Uli Klein

Tag der Promotion: 29. 5. 2006
Erscheinungsjahr: 2006

Abstract

The earth is continously bombarded by highly energetic particles, the cosmic radiation. Even 90 years after their discovery the origin and acceleration of the highest energy particles is still unknown. Air showers from cosmic rays are known to emit radio pulses since these pulses were detected in 1965. In the 1970 ties the measurement of these radio pulses ceased almost completely mostly due to difficulties with radio interference, uncertainty about the interpretation of the results and the success of other methods.

The measurement of radio pulses from air showers has a number of advantages: It gives a much higher duty cycle than measuring optical light, it is complementary to measuring the particles that reach the ground level, and with radio one can get a good direction estimate for the air shower. The advent of fast digital computers and high bandwidth, high dynamic range ADCs enables us to use digital filtering and beam forming to suppress the radio interference.

To test this technology we set up LOPES a prototype digital radio telescope in the scope of this thesis. It consists of 30 single polarisation antennas (10 in the first phase) that are set up at the site of the KASCADE-Grande experiment, an existing air shower array. It directly samples the radio signal in the frequency range from 40 to 80 MHz and stores 0.82 ms of raw data every time it was triggered by KASCADE-Grande. For the analysis the data is offline correlated with data from the KASCADE array, radio interference is digitally filtered, and a beam in the direction given by the KASCADE array is formed.

With this we have been able to reliably pick out radio pulses from air showers. The data from the first phase of LOPES are also analysed. By making cuts on the shower size (e.g. on the number of muons measured by KASCADE-Grande) and on the angle to the geomagnetic field one can select events so that each has a detected air shower radio pulse. The height of the radio pulse shows a nearly linear dependence on the shower size (with a power law index slightly smaller than one), an exponential decline with the distance of the antennas to the shower axis, and a monotonic rise with the angle of the air shower to the geomagnetic field. The latter dependence is a discrepancy to the current theoretical predictions. This has to be studied with better theoretical models and further measurements, e.g. of the polarisation characteristics.

We have shown that digital radio telescopes can measure radio pulses from air showers and give reproducible results. This is the first step to establish radio measurements of air showers as an additional method of cosmic ray research.

Contents

Chapter 1

Introduction

The study of cosmic rays is one of the most active fields in astroparticle physics. Their origin, acceleration, and transport to the earth has been one of the unsolved problems in astrophysics for nearly 100 years. To resolve these questions, larger detectors with higher duty cycles and which combine multiple detection techniques are needed. We have investigated an alternative way to study cosmic rays: measuring the radio emission from cosmic ray air showers. It is unaffected by attenuation, has a high duty cycle, gives calorimetric measurements, and provides high directional accuracy, promising to help solving the mystery of the cosmic rays.

Radio pulses from cosmic ray air showers were first discovered by Jelley et al. in 1965 at 44 MHz [Jelley65]. The results were soon verified and in the late 1960's emission from 2 MHz up to 520 MHz was found. In the following years these activities ceased almost completely mostly due to difficulties with radio interference, uncertainty about the interpretation of the results and the success of other methods.

Measuring the radio pulses from air showers has a number of advantages. If one can deal with the RFI[1] it allows for round the clock measurements, giving a much higher duty cycle than e.g. measuring fluorescence light. The signal is integrated over the whole air shower evolution, making it complementary to measuring the particles that reach the ground level. And because the radio pulse is not quantised like the particle signal one can get a better direction estimate for the air shower.

The advent of high bandwidth, high dynamic range ADCs allows us to digitise the whole radio frequency waveform and process the data with digital computers. This enables us to use digital filtering and digital beam forming to suppress the RFI and pick out air shower pulses. LOFAR the **Lo**w **F**requency **Ar**ray is a new digital radio telescope designed to take advantage of the new technology. It will work in the frequency range of 10 to 270 MHz and which is in the range of interest for cosmic ray measurements.

To test the technology of LOFAR and demonstrate its ability to measure radio pulses from air showers we built LOPES a **LO**FAR **P**rototyp**e** **S**tation. It is set up at the site of the existing air shower array KASCADE-Grande. Working together

[1] Short form of **r**adio **f**requency **i**nterference (see glossary).

with a well tested air shower experiment eases the development process and allows us to calibrate the radio signal.

After giving an introduction into cosmic rays, air showers and the relevant experiments, I present the instrument and the software that were developed as part of this thesis, discuss the RFI at the LOPES site, and show the scientific results of the first year of cosmic ray measurements.

1.1 Cosmic Rays

The earth is continously bombarded by highly energetic rays from outside the earth's atmosphere. This cosmic radiation was discovered by Victor Hess during balloon experiments. He detected that the intensity of ionising radiation above 1000 m height rises with increasing height and accounted this to radiation from outside the earth's atmosphere [Hess12]. It primarily consists of atomic nuclei with masses ranging from hydrogen (protons) to iron. Electrons and γ-quanta make up less than 1 % of the flux. The energy range of cosmic ray particles reaches over several decades from some MeV to more than 10^{20} eV. The arrival directions of the cosmic rays are distributed uniformly over the sky, only little anisotropy has been found at the highest energies.

Up to now there is no universally accepted theory for the origin of the primary particles at high energies, their acceleration, or their reactions in the interstellar medium during their transport to earth. Finding the sources of cosmic rays and understanding the mechanism that accelerates them to such high energies is one of the unsolved mysteries of astronomy.

When a cosmic ray particle hits a nucleus of an atom of the earth's atmosphere it undergoes a nuclear reaction and produces several secondary particles. These secondary particles can again react with atmospheric nuclei and produce more secondary particles. Together these particles form an extensive air shower. If the energy of the primary particle was high enough this air shower can be measured at ground level. At the highest energies the energies of these interactions are much larger than the energies reachable with current or future, earth bound accelerators. Thus air showers can be a laboratory for new particle physics.

Cosmic rays are also of concern for the public. The secondary particles of air showers form a significant fraction of the natural radioactivity on earth. Neutrons in air showers produce the radioactive ^{14}C isotope that is used for archaeological age determination. It has also been proposed that cosmic rays affect the weather and thus can play a role in climate changes [Shaviv05]. So the study of cosmic rays, their arrival directions, energy spectrum, and chemical composition is of interest for a number of branches of physics.

1.1.1 Energy Spectrum

Over a wide range the primary cosmic ray flux follows a simple power law $\frac{dN}{dE} \propto E^{-\gamma}$. At 10^{11} eV about one particle per second and square meter hits the earth, this

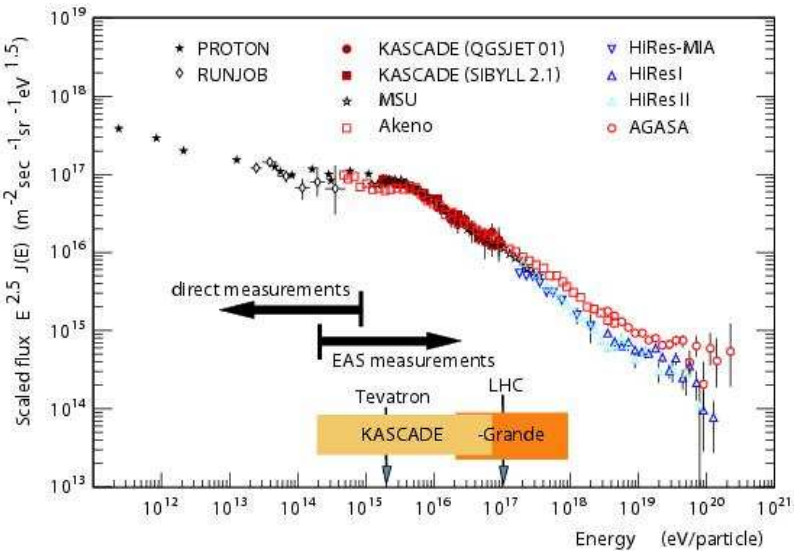

Figure 1.1: Spectrum of the cosmic ray flux, taken from [Haungs04]. The flux has been multiplied by a factor of $E^{2.5}$. This emphasis the so called *knee* at $\sim 5 \cdot 10^{15}$ eV and the *ankle* at $\sim 2 \cdot 10^{19}$ eV in the spectrum.

changes to approx. one particle per year and square meter at $5 \cdot 10^{15}$ eV, and above 10^{19} eV only about one particle per century and square kilometre hits the earth.

Figure 1.1 shows that the power law index γ changes at $\sim 5 \cdot 10^{15}$ eV, going from $\gamma \approx 2.7$ to $\gamma \approx 3.1$. This feature is called the *knee* of the cosmic ray spectrum. The probable cause for the knee are different acceleration mechanisms for energies below and above the knee (see section 1.1.4). But effects during the transport through the interstellar medium, or different reactions in the atmosphere are also possible.

At the highest energies above 10^{19} eV there is a flattening of the spectrum. This *ankle* could be caused by the Greisen–Zatsepin-Kutz'min effect ([Greisen66], [Zatsepin66]). This describes that high energy protons above $\sim 5 \cdot 10^{19}$ eV loose energy by producing pions in reactions with photons of the cosmic microwave background. This accumulates protons that had been accelerated to higher energies at energies below the reaction threshold.

At energies below 10^{10} eV the flux and direction of cosmic rays is affected by the solar wind and the magnetic fields of the earth and the sun. At higher energies these effects can be neglected.

Direct measurements of the primary cosmic rays with satellite or balloon borne experiments are possible up to $\sim 10^{15}$ eV. Above this energy the flux is too low, so it is not feasible any more to put suitable detectors on a balloon or satellite. On the other hand measurements of cosmic ray induced air showers are possible starting at this energy range.

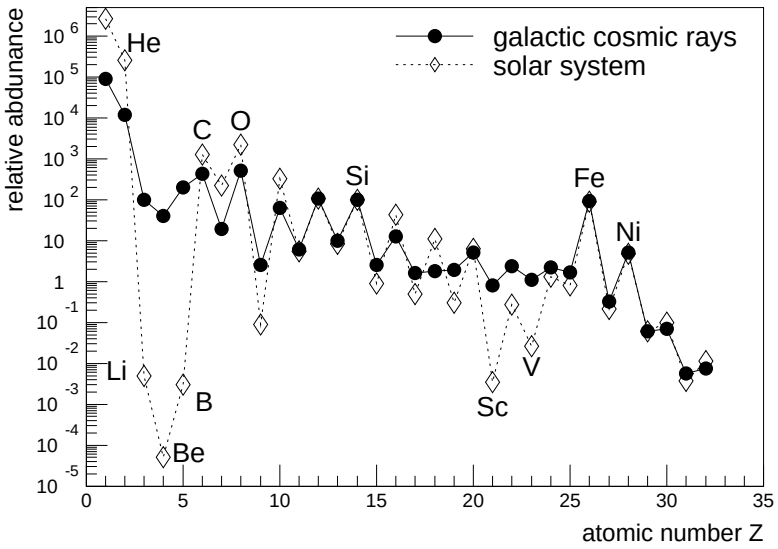

Figure 1.2: Chemical composition of the cosmic radiation with less than 2 GeV/nucleon compared to the composition in the solar system. Normalised to Si=100 [Wefel91].

1.1.2 Chemical Composition

With direct measurements it is possible to make a detailed measurement of the chemical composition of the cosmic radiation. Figure 1.2 shows the relative abundance of the different chemical elements for cosmic rays with less than 2 GeV/nucleon compared to the composition in the solar system.

The chemical composition of the solar system and the cosmic radiation agree to a large extent. This points to a common origin of the matter in the solar system and the matter in the cosmic radiation. Two discrepancies remain:

- The light elements hydrogen and helium are less common in the cosmic radiation, than in the solar system. This is probably due to the high ionisation energy of these elements, that suppress the initial acceleration of those elements.

- Lithium, beryllium, and boron as well as the elements from scandium to manganese are more common in the cosmic radiation. These elements are produced during the transport of the cosmic rays by spallation of nuclei from the CNO or the iron group .

At higher energies the chemical composition can only be deduced by comparing the results of air shower measurements to the results of simulations of air showers. As air showers have high statistical fluctuations and the simulations have large

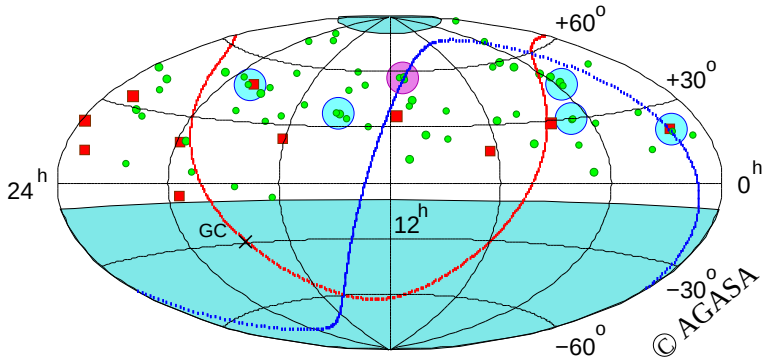

Figure 1.3: Arrival directions of cosmic rays with energies above $4 \cdot 10^{19}$ eV as measured by the AGASA experiment. Green circles represent events with E > 4×10^{19} eV, and red squares those with E > 10^{20} eV. Shaded circles indicate event clustering within the angular resolution of 2.5°. From [Takeda99].

uncertainties, the indirect determination has larger errors than the direct measurements. Nevertheless these measurements are of great interest as e.g. the knee in the cosmic ray spectrum falls into this regime. The analysis of KASCADE-Grande data shows that the knee in the total spectrum is caused by a knee of the different elemental groups at different energies [Ulrich05], [Antoni05]. It also suggests that the positions of the knees scale with the atomic number (Z) of the elements. The latter would exclude most theories of the knee being caused by different nuclear reactions in the atmosphere.

At the highest energies the chemical composition is still largely unknown. It is unlikely that the highest energy cosmic rays are caused by photons. Due to the fact that the determination of the chemical composition is based on interpreting air shower data with the help of interaction models it is unclear whether highest energy cosmic rays are mainly protons or heavy nuclei [Watson06].

1.1.3 Anisotropy

The arrival direction of charged cosmic rays is remarkably isotropic. The cosmic rays are deflected by the Galactic magnetic fields. This confines the particles in the Galaxy and homogenises their arrival directions. E.g. at energies up to 10^{15} eV the gyration radius of a cosmic ray is less than 1 pc, assuming a field strength of 1.4 μG. Measurements of large scale anisotropies for energies up to 10^{17} eV were either consistent with the assumption of total isotropy or showed only low statistical significance for deviations from it.

At higher energies the gyration radius increases, at 10^{18} eV it is a few hundred parsec. In the energy range around 10^{18} eV the AGASA experiment has reported a 3 σ excess from the direction of the Galactic centre [Hayashida99].At even higher

energies the cosmic rays can point back to their sources. In events above 4×10^{19} eV the AGASA experiment has seen a clustering of five doublets and one triplet, and the chance probability of observing such clustering under an isotropic distribution is less than 1% (see fig. 1.3) [Takeda99]. Due to the low flux at high energies both findings could neither been confirmed nor rebutted by other experiments. But large experiments will allow to collect the event rate to do astronomy with cosmic rays.

1.1.4 Origin, Acceleration, and Transport

Up to energies of a few MeV the cosmic rays are of solar origin. The astronomical objects that produce the high energy cosmic rays are largely unknown. The great energy range and the features in the energy spectrum suggest that different kinds of sources are responsible for the cosmic radiation at different energies. Possible sources are supernova remnants, supernova explosions into the wind of other supernovae, pulsars, magnetars, or active galactic nuclei. Another possible source is the decay of heavy particles, e.g. topological defects or relics from phase transitions of the early universe. The former group is called bottom–up models as a cosmic ray particle starts at low energy and is then accelerated, similarly the latter group is called top–down models.

In the bottom–up models the acceleration is due to electromagnetic forces. This can be a direct acceleration that requires strong electromagnetic fields or a stochastic acceleration. The primary model for stochastic acceleration is the first order Fermi-acceleration [Fermi49]. In this model a charged particle is scattered by magnetic fields and repeatedly traverses a shock front in the interstellar medium. On average it gains an energy of $\frac{\Delta E}{E} \propto \beta$ (with $\beta = \frac{v}{c}$ the speed of the shock front) at each crossing. The second order Fermi-acceleration is less effective. In this model a charged particle is scattered repeatedly at statistically distributed magnetic clouds and gains on average $\frac{\Delta E}{E} \propto \beta^2$ in every cycle.

The charged particles of the cosmic radiation are deflected by magnetic fields in the Milky Way. This confines cosmic rays with energies $< 10^{18}$ eV to the Milky Way and its halo. From the relative abundances of radioactive isotopes one can infer the elapsed time since nucleosynthesis or spallation. With this, the average age of the cosmic rays is estimated to $\sim 10^7$ years. From the relative abundances of the spallation products one can estimate the traversed matter density of the cosmic rays to $\sim 5\,\mathrm{g/cm^2}$. This entails that the cosmic rays stay mostly in the halo outside of the galactic disc.

1.2 Air Showers

When a cosmic ray particle enters the earth's atmosphere it sooner or later reacts with an atomic nucleus of the air. Due to the composition of the air this is usually a nitrogen nucleus. In this reaction a multitude of secondary particles is formed, which in turn react with atoms in the air and produce more secondary particles. This is done not only by hadronic interactions but also by electromagnetic interactions with

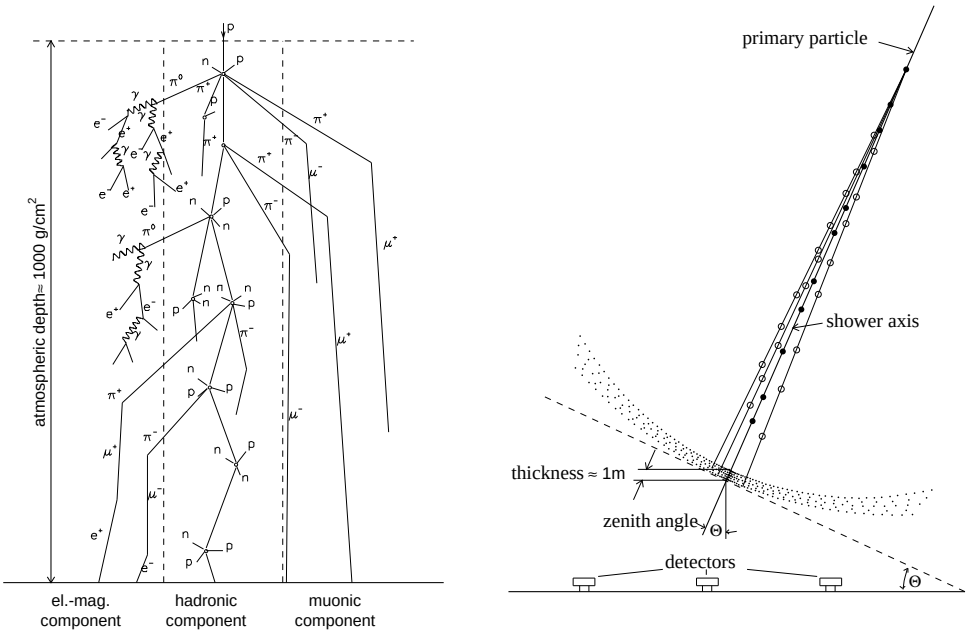

Figure 1.4: Schematic view of an extensive air shower [Alkhofer75].

atoms or electrons and by the decay of unstable particles. Eventually this cascade contains a large number of different particles which can even reach the earth's surface if the energy of the primary particle was large enough. This is called an extensive air shower.

The particles in such an air shower form a disc with a few meters thickness and up to a some kilometres lateral extend that moves through the atmosphere with practically the speed of light. This disc is not completly flat, but has more the form of a cone with a very obtuse opening angle. In the centre the disc is thin but increases in thickness with increasing distance (see fig, 1.4).

In the beginning of the evolution of an air shower the total number of particles rises due to the production of secondary particles. After the average energy per particle drops below the threshold for the production of new particles the absorption of particles in the air starts to dominate and the total number drops exponentially with the atmospheric depth (see fig, 1.5).

1.2.1 Components of an Air Shower

The particles in an air shower can be grouped into a hadronic, an electromagnetic and a muonic component. Neutrinos are usually not taken into account as they do not produce further secondary particles and are too difficult to measure. Similarly radiation in the UV, optical and at radio wavelength is referred to as being emitted by and not as being part of the air shower.

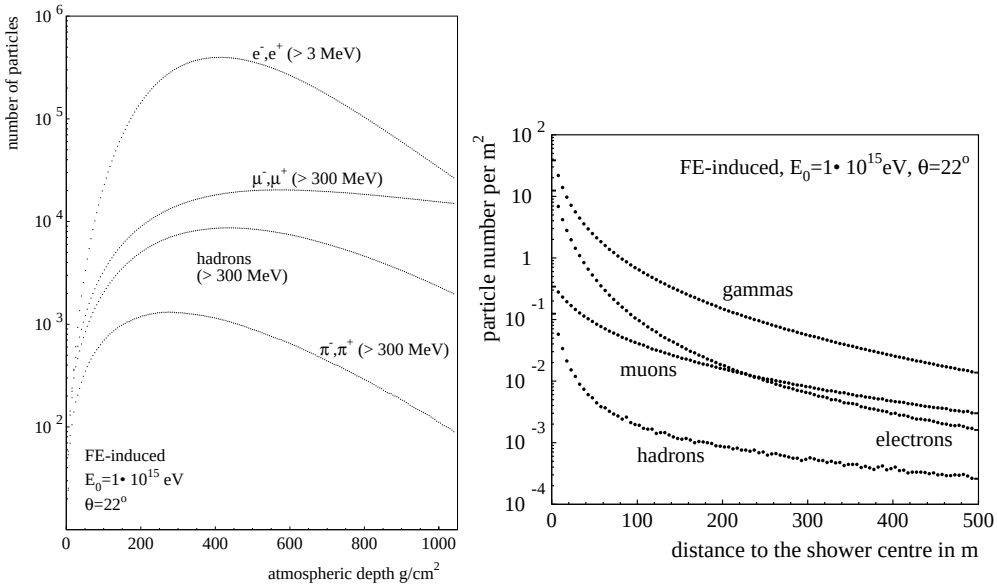

Figure 1.5: Longitudinal and lateral particle distribution in an extensive air shower. Averages over 1000 simulations of an air shower induced by a 10^{15} eV iron nucleus at a zenith angle of 22°, [Glasstetter01].

Hadronic Component

Every air shower that is initiated by an atomic nuclei as primary particle starts from its hadronic component. The hadronic component consists of the strong interacting particles in the air shower, i.e. fragments of nuclei, single nucleons, mesons etc. In this pions are the most common kind of particles. On average their transversal impulse is rather low compared to their total impulse. So, high energy hadrons are concentrated in a radius of only a few tens of meters around the shower axis.

New hadrons are produced in high energy collisions of hadrons. When the energy of a hadron is too low for the production of pions it looses energy through ionisation until it decays or is stopped.

At the high energies of the primary particles the nucleons of a nucleus can be considered as free particles. So an iron induced air shower can be be considered as the superposition of 56 proton induced air showers each with the 56th part of the total energy. The proton–air cross section above 100 GeV rises only logarithmic with energy, so the iron–air interaction length is about 4 times smaller than the proton–air interaction length [Geich-Gimbel89]. This makes iron induced air showers evolve earlier and faster in the atmosphere than proton induced ones.

Electromagnetic Component

The electromagnetic component of an air shower consists of electrons, positrons and photons. It is being generated mostly by the decay of uncharged pions. The highly energetic particles then produce electromagnetic cascades in which they convert into each other by pair production and bremsstrahlung. The cascade starts with no average charge but it "picks up" atmospheric electrons (by acceleration of atmospheric electrons, e.g. through compton recoil, or $e^+ - e^-$ annihilation) and thus develops a negative charge excess. The average energy per particle drops by 1/e for every radiation length that has been crossed. Once the energy of the electrons/positrons drops below the critical energy ($E_{crit,air} = 84.2\,\mathrm{MeV}$) they loose, on average, more energy by ionisation than by bremsstrahlung. Then they do not produce new γ-quanta and the electromagnetic cascade dies out.

Air showers that have been initiated by an electron or photon consist nearly solely out of one electromagnetic cascade. The electromagnetic component of a hadron induced air shower consist of the superposition of many electromagnetic cascades.

The electromagnetic component of a hadronic air shower is generated from decaying pions, these pions have a short life time, and the electromagnetic component is strongly absorbed in air. So it has its maximum in the longitudinal development between those of the hadronic and of the muonic component (see fig. 1.5).

The lateral distribution of an electromagnetic cascade can be parametrised by the NKG-function [Kamata58], [Greisen56]:

$$\rho_e(r) = C(s) \cdot \frac{N_e}{2\pi r^2} \cdot (\frac{r}{r_m})^{s-2} \cdot (1 + \frac{r}{r_m})^{s-4.5} \tag{1.1}$$

with: ρ_e=electron density per m^2, N_e=number of electrons, r=distance to the shower centre, $C(s) = \frac{\Gamma(4.5-s)}{\Gamma(s)\Gamma(4.5-s)}$=normalising factor, s=shower age, and r_m=Moliére radius. The shower age is a parameter for the evolution of the shower, it is $s = 0$ at the shower start, $s = 1$ at the maximum number of particles, and $s = 2$ when the shower has less than one particle left. The NGK-function is valid for the range $0.8 < s < 1.6$. At sea level the Moliére radius is $r_m = 79\,\mathrm{m}$.

The lateral distribution of the electromagnetic component of a hadronic air shower can also be parametrised by the NKG-function, although s and r_m have lost their original meaning. E.g. the KASCADE air shower reconstruction uses $r_m = 89\,\mathrm{m}$ and uses s as a fit parameter for the steepness [Antoni03].

Muonic Component

The muons in an air shower are produced by the decay of charged pions and kaons. The muons themselves decay into electrons/positrons and neutrinos. Compared to pions their life time is about 100 times longer. Compared to electrons the scattering and bremsstrahlung is a factor of $(m_\mu/m_e)^2 \approx 4300$ smaller. Moreover the range of the muons in the laboratory rest frame is extended by relativistic time dilatation. Hence most muons reach the earth's surface.

The lateral distribution of the muons is mostly caused by the angular distribution and the height of their production. It can also be parametrised by the NKG-function (eq. 1.1). However the lateral distribution of the muons is flatter than the one of the electromagnetic component. The KASCADE air shower reconstruction accounts for this with a larger Moliére radius, $r_{m,muons} = 420\,\mathrm{m}$ [Antoni03].

1.2.2 Measurement Techniques

There are currently three different, established methods in use to measure air showers:

Air Cherenkov A charged particle with a speed larger than the speed of light in air (i.e. with $\beta > \frac{1}{n_{\mathrm{air}}}$) emits Cherenkov light. In clear, moonless nights this light can be measured by optical telescopes with photomultiplier cameras. The image obtained with these telescopes shows the track of the air shower. From this track the direction of the primary particle can be reconstructed. With two telescopes observing an air shower in stereo mode one can get an angular resolution on single air showers of less than 0.1° [Hinton04]. The Cherenkov radiation is strongly beamed into the forward direction, so the illuminated area on the ground is only a few hundred meters wide. Coupled with the little available measurement time this means that this method is only useful for energies below the knee where the flux is large enough. Examples are the Tunka array [Budnev05] and the AIROBICC array of the HEGRA experiment [Karle95]. The shape of the image of the air shower track is also useful to differentiate between hadron induced and photon induced air showers. Consequently this method is used for TeV–γ observatories like the H.E.S.S. experiment [Hinton04].

Air Fluorescence The ionising particles in an air shower excite the nitrogen molecules in air which in turn emit fluorescence light. By observing this light with optical telescopes one can image the track of the air shower in the atmosphere. This is only efficient for shower energies larger than $10^{17}\,\mathrm{eV}$, and like the air Cherenkov method this is only possible in clear, moonless nights, i.e. in about 10% of the time. The amount of light that is emitted allows a quantitative measurement of the complete air shower evolution. The angular resolution of the method is about 0.6° [Bonifazi05]. Only a small fraction of the energy of an air shower is emitted as fluorescence light, this makes this method usable for only the highest energies. The air shower with the highest energy was measured with this technique by the "Fly's Eye" experiment [Baltrusaitis88]. Other experiments using this method are the HiRes [Matthews01] experiment and the fluorescence detectors of the Pierre Auger Observatory [Kampert04].

Particle Detector Arrays Above about $10^{14}\,\mathrm{eV}$ an air shower has enough energy for a large number of particles to reach the earth's surface. These particles can then be measured with particle detectors. The detectors are distributed uniformly over the measurement area. The spacing between two

adjacent detectors determines the low energy threshold of the experiment (e.g. KASCADE array: 13 m, $\sim 10^{14.6}$ eV, and Auger 1.5 km, $\sim 10^{18.3}$ eV [Antoni03], [Kampert04]), and the size of the covered area determines the highest energy at which one has a reasonable count rate (e.g. KASCADE array: $4 \cdot 10^4$ m^2, $\sim 10^{17}$ eV, and Auger: $3 \cdot 10^9$ m^2, $> 10^{20}$ eV). From the arrival times of the particles in the detectors one can determine the direction of the air shower, and from the energy measured with the detectors one can get the number of particles. With suitable detectors it is possible to measure more shower parameters, e.g. separate measurements of electron and muon number. Examples of this technique are the AGASA experiment [Chiba92], the surface detectors of Auger and the KASCADE-Grande experiment (see section 1.5).

Having the earth's atmosphere between the primary cosmic ray and the air shower detectors on the surface has advantages and disadvantages compared to direct measurements. The biggest disadvantage is that the energy and type of the primary particle has to be determined from the measured air shower parameters. The advantage is that the atmosphere acts as a target and calorimeter for the cosmic ray so that the air shower parameters do contain the information of the primary particle energy and type. Only this makes cosmic ray measurements at this low fluxes economically feasible. To get the air shower parameters one needs only relatively few measurement points, e.g. the Auger surface detector covers an area of $3 \cdot 10^9$ m^2 with only $1600 * 11.3\,\text{m}^2 = 1.8 \cdot 10^4$ m^2 instrumented area.

1.2.3 Determination of Primary Particle Energy and Type

Determination of the primary particle energy from air Cherenkov or fluorescence data is relatively straight forward. Both methods can sample the track of the air shower through the atmosphere. So, by converting the measured light intensity into particle numbers and integrating over the whole shower evolution one can get a quasi bolometric measurement of the energy in the air shower and thus the primary particle energy. The only remaining uncertainty – apart from measurement errors – that cannot be measured in a laboratory is the fraction of energy that goes into unseen particles, e.g. neutrinos, but this can be expected to be small.

Getting the primary particle energy from particle array data is a bigger problem. A simple measure for this is the electron or muon number as measured on the ground. But these values are affected by air shower fluctuations and are dependent on the type of the primary particle.

The air Cherenkov method can distinguish between air showers from γ–rays and from hadrons (hadronic air showers give a more patchy image than γ induced ones), a suppression of the much more frequent hadronic air showers by a factor of 1:1000 and more is possible. For the distinction between different atomic nuclei the air fluorescence can use the height of the shower maximum or the fluctuations in the shower, while the particle arrays can, e.g., use the relation of the muon to the electron number. Among primary particles with the same energy the air showers

from heavier nuclei have their maximum higher in the air, show less fluctuations and have a higher muon to electron fraction.

For a detailed analysis, especially of particle array data, one has to compare the measured values with results from the simulation of air showers. These simulations are usually Monte-Carlo simulations in which the single particles are tracked from interaction to interaction and the results of these interactions are calculated by interaction models. To save computation time one can replace sub-showers with an analytical parametrisation (e.g. for electromagnetic sub-showers) or one can track only one particle out of many similar particles and have it represent the other particles in the final evaluation. For the different kinds of interactions (high and low energy hadronic interactions, electromagnetic interactions etc.) different kinds of interaction models can be used. Especially the high energy interaction models that are extrapolated into regions which are not accessible with particle accelerators, produce uncertainties in the simulation results. It is common that using a different model for the high energy interactions leads to somehow different results in the cosmic ray analysis. The usual energy resolution for these analyses is better than 20%, the mass determination is much more difficult [Haungs03b].

1.3 Radio Emission of Air Showers

Measuring the radio pulses from air showers has a number of advantages compared to the established measurement techniques. With effective RFI suppression one can measure even in relatively radio loud environments, i.e. close to cities which is not possible with optical telescopes. It is not much affected by observing conditions. Except during thunderstorm conditions which seem to amplify the radio signal emitted by air showers [Buitink05], [Buitink06] one can measure day and night. This gives it a much higher duty cycle than optical measurements.

Radio waves are only very little attenuated in the atmosphere. Thus, even though one cannot image the track of the air shower, the radio signal is a bolometric measurement from the whole air shower evolution. This gives less information than the measurement of the shower evolution as possible with fluorescence telescopes, but it is complementary to particle measurements on the ground. A hybrid instrument with particle detectors and radio antennas gives enough information for composition studies and has a much higher duty cycle than a hybrid experiment including optical telescopes.

The little attenuation of radio signals also makes it possible to measure highly inclined air showers whose particle component has already, mostly died out at the ground level [Petrovic05]. This is interesting for the study of air showers that are induced by high energy neutrinos, as it can help to distinguish between neutrino induced air showers and other air showers. Radio detectors can see air showers from any primary while particle detectors mainly detect those from neutrinos that had their first interaction close to the detectors.

The radio signal forms a continuous pulse front unlike the particle front that is

quantised. This makes it possible to measure the relative arrival times of the shower front at different positions with high precision and thus get a better estimate for the arrival direction of the cosmic ray than with particle detector arrays.

1.3.1 Early Experimental Data

In 1962 Askaryan predicted that particle showers in matter should emit radio signals [Askaryan62]. He proposed that particle showers develop a negative charge excess so that the showers can coherently emit Cherenkov radiation at radio frequencies. In 1965 Jelley et al. discovered that extensive air showers indeed produce radio pulses at 44 MHz [Jelley65]. In the following years emission from 2 MHz up to 520 MHz was found. Soon it was discovered that the signal strength in one polarisation direction depends on the angle of the air shower to the geomagnetic field, supporting theories that the radiation of air showers is caused by geomagnetic effects. Further studies showed that the polarisation of the radio signal is consistent with a geomagnetic emission process [Allan71].

These historical experiments were limited by the existing technology. They could only measure with a relatively small bandwidth of a few MHz and they were limited to total power receiving systems. The latter includes that the radio signal is integrated with a time constant on the order of hundreds of nanoseconds, which also smears out the air shower pulse. A system like this is susceptible to RFI, it is impossible to filter out transmitter stations that leak into the frequency band and one cannot distinguish air shower pulses from RFI pulses. Consequently measurements were often only done at night when commercial TV and radio stations were turned off and access to the site could be restricted.

In 1971 the results of the radio measurements were summarised in a review by Allan [Allan71]. His analysis led to an approximate formula relating the received voltage per unit bandwidth to other air shower parameters:

$$\epsilon_\nu = 20 \left(\frac{\mathrm{E_p}}{10^{17}\mathrm{eV}} \right) \sin\alpha \cos\theta \exp\left(\frac{-\mathrm{R}}{\mathrm{R_0}(\nu,\theta)} \right) \left[\frac{\mu\mathrm{V}}{\mathrm{m\,MHz}} \right] \tag{1.2}$$

(With: $\mathrm{E_p}$ is the primary particle energy, α the angle to the geomagnetic field, θ the zenith angle, R the distance to the shower axis, $\mathrm{R_0}$ a scale parameter , and ν is the observing frequency. $\mathrm{R_0}$ is around 110 m at $\nu = 55$ MHz and $\theta < 35°$ and becomes larger with increasing θ and decreasing ν.)

The $\sin\alpha$ term in this formula is not deducted from a quantitative measurement but is theoretically motivated from the fact that the polarisation measurements prefer a geomagnetic emission process. Some later works (e.g. [Prah71]) yielded much smaller values for the field strength. Part of this discrepancies may be due to errors in the calibration, e.g., of the primary particle energy [Atrashkevich78]. Additionally the documentation of the available data is not always precise, which makes direct comparisons complicated. Although comparisons of the absolute values are difficult, the trend in the dependence on the primary particle energy, the shower geometry, and the radial distance is fairly consistent in the historical data.

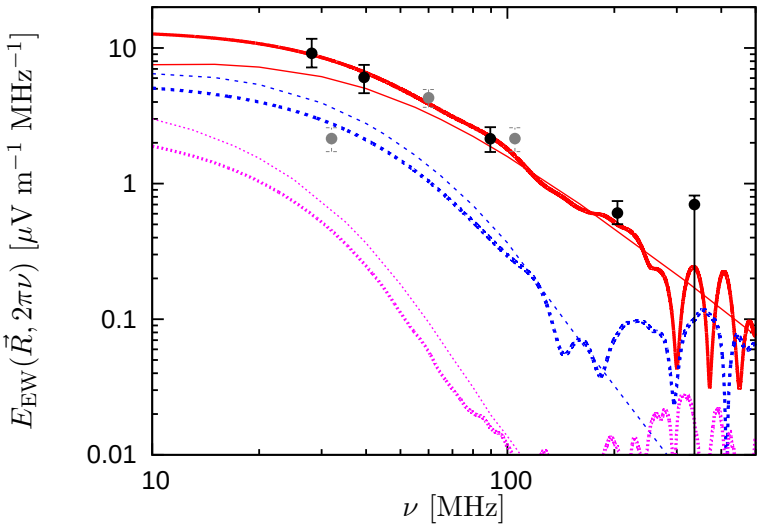

Figure 1.6: Comparison of historical data and calculated Spectra from a vertical, 10^{17} eV air shower. Comparison of historical data and theoretical modelling of the geosynchrotron emission. Thin lines: analytical calculations, thick lines: MC simulations; solid: shower centre, dashed: 100 m, dotted: 250 m north of shower centre. Data Points: Historical data for the shower centre from Prah [Prah71] and Spencer [Spencer69], rescaled to be consistent with the data from [Allan71] at 55 MHz. Taken from [Huege05a].

1.3.2 Theory

The first postulated process for radio emission from air showers was Cherenkov radiation. The particles in the air shower travel faster than the speed of light in air so they emit Cherenkov radiation. The physical size of an air shower is smaller than the wavelength at radio frequencies so the emission is coherent. In a neutral shower with as many positrons as electrons the emission from positrons and electrons would cancel each other out. Askaryan proposed that because the atmosphere or any other matter contains many electrons but no positrons an air shower develops a negative charge excess [Askaryan62], [Askaryan65]. The net charge then allows an air shower to emit Cherenkov radiation at radio wavelengths.

Another emission mechanism is due to the deflection of charged particles (mostly electrons and positrons) in the earth's magnetic field. There are two ways to look at this, both are expected to be equivalent. One interprets it as a separation of charges in the air shower which leads to transverse currents in the air shower which in turn emit dipole radiation [Kahn66]. Falcke & Gorham [Falcke03] interpreted this as synchrotron radiation of particles gyrating in the geomagnetic field.

As the experimental data shows a clear dependence of the radio emission on the angle to the geomagnetic field, the geomagnetic emission process has to be the

θ	E_θ [μV m^{-1} MHz^{-1}]	l_θ [m]	b_θ [m]
0°	12.33	135.30	219.41
15°	11.04	152.80	219.16
30°	8.33	202.09	254.23
45°	4.98	339.71	305.17
60°	2.53	873.54	590.03

Table 1.1: Parameters for the parametrisation of the Monte Carlo results according to equation 1.3.

dominant one in air showers. For radio emission from particle showers in dense media the charge excess mechanism seems to be dominant [Saltzberg01].

The most extensive modelling of radio emission from air showers was done in the PhD thesis of Tim Huege within the scope of the LOPES project [Huege04]. He started with an analytical calculation of the geosynchrotron radio emission from air showers [Huege03]. Then he made a Monte Carlo simulation of the process [Huege05a]. The results from these calculations show a good agreement with each other and with the historical data. Figure 1.6 shows spectra of the radio emission for a standard air shower from this calculations compared to historical data points that were rescaled to be consistent with the data from [Allan71] at 55 MHz. There is also a parametrisation of the results of the Monte Carlo simulation, giving the dependence of the electric field strength on some air shower parameters [Huege05b]:

$$\begin{aligned} \left|\vec{E}(\theta, l, \nu, E_\mathrm{p}, X_\mathrm{max})\right| &= f\ E_\theta\ \left(\frac{E_\mathrm{p}}{10^{17}\ \mathrm{eV}}\right)^{0.96} \exp\left[-\frac{\nu/\mathrm{MHz} - 10}{47.96\ \exp\left[-l/b_\theta\right]}\right] \\ &\quad \times \exp\left[-\frac{200\,\mathrm{m}\,(\alpha(X_\mathrm{max}) - 1) + l}{\alpha(X_\mathrm{max})\ l_\theta}\right] \\ \text{with :} \qquad \alpha(X_\mathrm{max}) &= 1.00636\ \left(\frac{X_\mathrm{max}}{631\ \mathrm{g\ cm^{-2}}}\right)^{-1.50519} \end{aligned} \tag{1.3}$$

and with X_max the depth of the shower maximum (in g/cm^2) , l the distance of the antenna to the shower axis, the values for E_θ, l_θ and b_θ taken from table 1.1, and $f = 1$ a fudge factor left for experimental verification.

One of the results is that the field strength rises nearly linearly with the primary particle energy, this means that the emitted power rises quadratically with primary energy. This shows that the emission is nearly totally coherent as incoherent emission would only result in a linear rise of the power with energy. Another result is that the total electric field strength only weakly depends on the angle of the shower to the geomagnetic field. What does depend on the angle to the geomagnetic field, is the polarisation. The emission is almost purely linearly polarised in the direction perpendicular to the magnetic field and the air shower axis. So one polarisation component has not a simple dependence on the angle to the geomagnetic field,

e.g., showers from due north or due south are both completely east-west polarised although they have different geomagnetic angles.

One limitation of these calculations is that they are based on an analytical model of the air shower. This model does not include air shower fluctuations, realistic pitch angle distributions of the particles, or spatial clumpiness of the particle density. As these can affect the coherence of the radio emission they may have a significant effect on the emitted field strength. To account for this the fudge factor f was introduced in eq. 1.3.

1.3.3 Recent Experiments

The first effort trying to measure radio emission from air showers with the help of fast ADCs was done by Green et al.[Green03]. They set up one antenna near the CASA/MIA array [Borione94] in Utah. Due to the limitations of the experiment and high levels of RFI they were not able to measure radio pulses from air showers. They found an upper limit for the emission strength of $\epsilon_\nu < 34 \frac{\mu\mathrm{V}}{\mathrm{m\,MHz}}$ at a primary particle energy of $\sim 10^{17}\,\mathrm{eV}$.

Another effort is the CODALEMA experiment [Ardouin05a]. This uses several antennas of the Nançay decametric array, together with a small number of scintillation detectors. The site is very radio quiet and the scintillation detectors are well shielded. With this they were able to measure radio pulses from air showers with field strengths around from a few to $25 \frac{\mu\mathrm{V}}{\mathrm{m\,MHz}}$ [Ardouin05b]. They also confirmed the limited footprint of the illuminated area on the ground of a few hundred meters and use it to distinguish between air shower pulses and RFI pulses. One limitation of this experiment is that it does not have access to a calibrated air shower array. So while having well calibrated radio data, the calibration of the air shower parameters depends on incidental measurements, e.g. estimating the primary energy from the trigger rate.

The LOPES experiment is designed to avoid this problem. By placing it at the site of an existing air shower array it has access to well calibrated air shower parameters. With this LOPES was the first experiment to unambiguously measure radio pulses from air showers with a digital radio telescope [Falcke05]. The disadvantage – but also an interesting challenge – of the site is that LOPES has to deal with significant RFI. So one of the goals of LOPES was to develop the techniques to suppress this RFI. Another goal was to calibrate the radio pulses with the air shower parameters from KASCADE-Grande. The techniques to suppress the RFI and the preliminary results of the calibration are presented in this thesis. So with LOPES and CODALEMA running in parallel both experiments complement each other.

1.4 LOFAR

LOFAR the **Lo**w **F**requency **Ar**ray is a new radio telescope that is currently being built in the Netherlands with the goal of (re-)opening the low frequency band from 10 MHz to 270 MHz for astrophysical research. It is the first so called digital

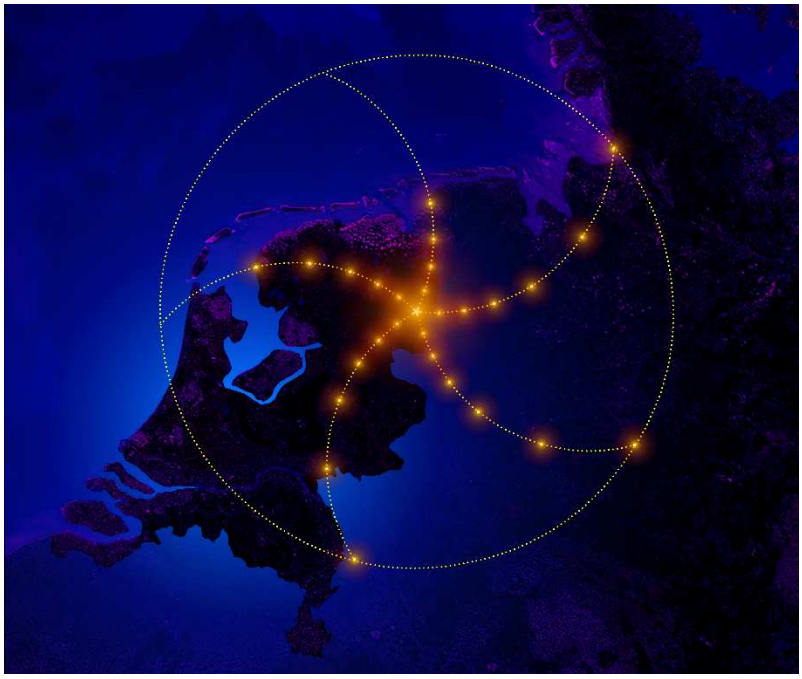

Figure 1.7: Artists impression of the placement of the LOFAR stations in the Netherlands and northern Germany. (From `http://www.lofar.nl/`.)

radio telescope. Instead of using a small number of high gain antennas as in conventional interferometers it uses a large number of quasi omnidirectional antennas, digitises the radio signal from each antenna and does all further processing with digital computers.

1.4.1 The LOFAR System

To reduce the amount of data that needs to be transmitted the antennas of LOFAR will be grouped into stations. The data from the antennas inside a station will be beamformed and only the formed beams are transmitted to the central processing facility. At the central computer the data can then be correlated or also be beamformed. This way LOFAR works similar to a classical interferometer with the stations replacing the traditional dishes. A new feature is the possibility to store for a short time the waveform signal from each antenna in digital memory. After a transient event, like an air shower, has been detected one can then download the data from all antennas to the central storage for offline processing.

The initial LOFAR array will consist of 77 stations. It will consist of 32 stations in the virtual core in the northern part of the Netherlands, and 45 remote stations with baselines up to 80 km, see fig. 1.7 for an artists impression of a full LOFAR array. All stations will have 100 low band antennas optimised for the 30 MHz - 80 MHz range,

Frequency	Point Source Sensitivity		Effective Collecting Area		Beam Size	
	VC	Full Array	VC	Full Array	VC	FA
30 MHz	4.8 mJy	2.0 mJy	$7.9 \cdot 10^4$ m^2	$1.9 \cdot 10^5$ m^2	21'	25"
75 MHz	3.3 mJy	1.3 mJy	$1.2 \cdot 10^4$ m^2	$3.0 \cdot 10^4$ m^2	8.3'	10"
120 MHz	0.17 mJy	0.07 mJy	$7.9 \cdot 10^4$ m^2	$1.9 \cdot 10^5$ m^2	5.2'	6.0"
200 MHz	0.15 mJy	0.06 mJy	$2.9 \cdot 10^4$ m^2	$6.9 \cdot 10^4$ m^2	3.1'	3.5"

Table 1.2: Sensitivity and beam size at different frequencies for the initial LOFAR array. Calculated for 4 MHz bandwidth and 1 h integration time. (VC = virtual core, FA = full array)

and 100 high band antenna tiles optimised for the 110 MHz - 240 MHz range. The low band antennas are described in section 2.1.1 as LOPES uses prototypes of them. A high band antenna tile consists of an 4×4 array of dipoles with analogue beam forming. Above 240 MHz and below 30 MHz the antennas are still usable, but with less efficency. Due to the strong RFI in the FM band the 90 MHz - 110 MHz range is excluded in the electronics. The signal is digitised in one of four frequency bands: 10–90 MHz, 110–190 MHz, 170–230 MHz, and 210–290 MHz. With the full array one can have 8 beams of 4 MHz bandwidth each. These beams can either be placed at independent positions inside the primary element beam, or a number of them can be combined to have fewer beams with more bandwidth inside the digitised band. If one uses only the stations of the virtual core then one has more total bandwidth available in independent beams of 4 MHz bandwidth each. Table 1.2 shows the sensitivity and beam size of the initial LOFAR array at different frequencies.

LOFAR is essentially a distributed sensor network connected to a fast computer. For radio astronomy the sensors used are radio antennas and the computer is used as a correlator. For other applications one can connect other sensors and run a different program on the computer. In the beginning there will also be geophones and microbarometers connected to the LOFAR stations for geophysical measurements. It is also planned to add agriculture sensor systems to measure the micro-climate of planted crops.

1.4.2 Key Science Projects

LOFAR has currently four key science projects: the epoch of reionisation, deep extragalactic surveys, transient sources, and cosmic rays [Bruyn02][2].

Epoch of Reionisation

After the period of recombination (which generated the cosmic microwave background) the matter in the universe was mostly neutral hydrogen. Most of the intergalactic medium is now ionised. Measurements of the cosmic microwave background

[2] An overview of the LOFAR science case can also be found at `http://www.lofar.org/`

suggest that this reionisation started at redshifts z ∼ 15-20. With LOFAR the redshifted 21 cm line of neutral hydrogen can be measured at redshifts from z = 11.4 (115 MHz) to z = 6 (180 MHz). The key questions this key project will address are:

- What is the redshift range in which the bulk of the neutral hydrogen became ionised? Can a clear single redshift of reionisation be identified or defined or are there multiple phases of reionisation?

- What are the characteristics of the spatial distribution of heated and still cold inter galactic medium and how do these evolve during the era of reionisation?

- Which objects or processes are responsible for re-ionising the Universe?

Deep Extragalactic Surveys

LOFAR is well suited for the creation of large sky surveys. Deep LOFAR surveys of the accessible sky at several frequencies will provide unique catalogues of radio sources. The LOFAR surveys will probe the sky in a largely unexplored frequency range with unprecedented resolution and sensitivity, so it is likely that they will discover new phenomena. Among the expected sources are:

- the most distant radio galaxies. Since distant radio galaxies pinpoint proto-clusters studying the environments of these distant galaxies will constrain the formation of galaxy clusters at the earliest epochs. Detecting such objects before the epoch of reionisation would not only yield important constraints on how and when massive black holes are formed, but it would also allow detailed studies of the ISM at these high redshifts through redshifted 21 cm absorption studies.

- diffuse emission in galaxy clusters. Clusters often contain diffuse radio sources that are shaped by the dynamics of the gas in which they are embedded. LOFAR will be able to detect and study diffuse emission in many thousands of clusters. Such studies will be very relevant for understanding the effects on the dynamics of cluster gas by cluster mergers, determining the origin of cluster magnetic fields, and constraining physical models for the origin of these sources.

- star-forming galaxies. Because of the large fields of view, surveys at the higher LOFAR frequencies will detect unprecedented numbers of star-forming galaxies, including galaxies at an epoch at which the bulk of galaxy formation is believed to occur. Together with sub-mm wave measurements the distance to these galaxies can be measured. Thus providing a census of the cosmic star-formation history unhindered by the effects of dust obscuration.

Transient Sources

The large instantaneous beam of LOFAR makes it uniquely suited to efficiently monitor a large fraction of the sky, allowing a sensitive unbiased survey of radio transients. Table 1.3 gives an overview of the classes of objects known or expected to exhibit variable radio emission.

Class of object	Time-scale	Expected	Maximum Distance
GRB afterglows (extragal.)	months	100/a	Observable universe
LIGO Events	ms – hours	a few ?	Observable universe
Radio Supernovae	days – months	$\sim$3/a	100 Mpc
Intermediate mass BH	days	1-5	30 Mpc
Flare Stars	ms – hours	100-1000	1 kpc
Exo-planets	min – hours	10-100	30 pc

Table 1.3: An overview of the classes of objects known or expected to exhibit variable radio emission detectable with LOFAR. Included are the variability time-scales, the number of objects/events that are expected to be observed and an estimate of the distances to which these objects can be seen.

Cosmic Rays

The goal of this key project is to use LOFAR as a cosmic ray detector. It is the continuation of the work that was started with the LOPES project, and is described in this thesis. The major difference between measuring air showers with LOPES and with LOFAR is that LOFAR does not have access to particle detector data. The biggest effect of this is that LOFAR needs a radio trigger for cosmic rays which also distinguishes between radio pulses from air showers and radio pulses from RFI.

1.5 KASCADE-Grande

KASCADE-Grande is an experiment for the measurement of cosmic ray air showers, situated at the Forschungszentrum Karlsruhe[3] in Germany [Antoni03], [Chiavassa03]. KASCADE-Grande was built by extending the existing KASCADE experiment to higher energies with detectors from the EAS-Top experiment [Aglietta90]. Its goals are to study the primary cosmic ray composition and the hadronic interactions in the primary particle energy range of $10^{16} - 10^{18}$ eV. It does this by measuring simultaneously many different parameters from the electromagnetic, muonic and hadronic components of air showers. For this it consists of diverse detector components which are optimised to measure different shower parameters. Figure 1.8 shows the layout of the different KASCADE-Grande components, they are:

[3]See `http://www.fzk.de`

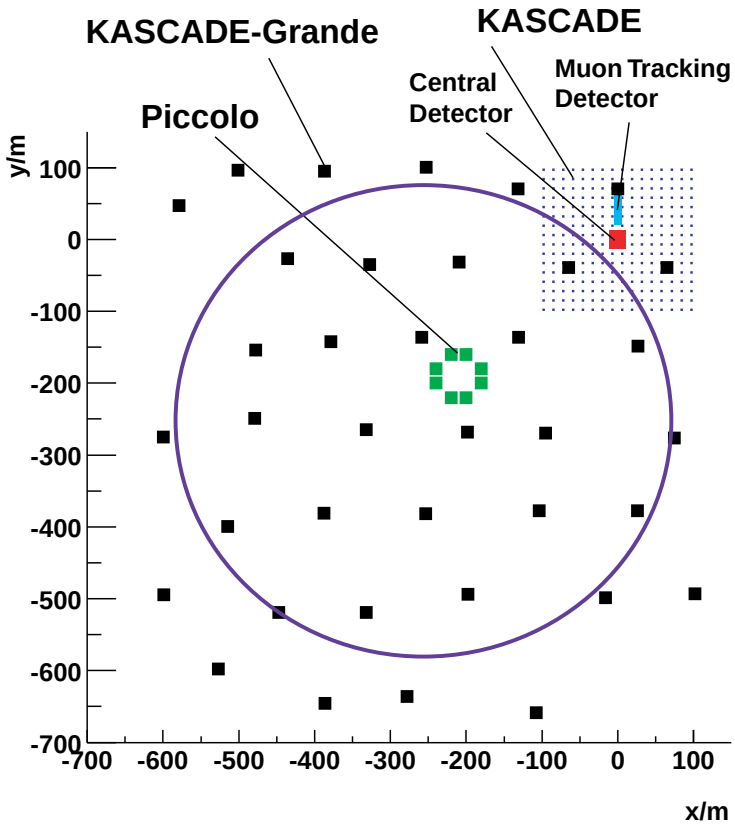

Figure 1.8: Layout and scheme of the KASCADE-Grande experiment with the original KASCADE experiment, the Grande array, and the Piccolo trigger array. The ring inside the Grande array marks the fiducial area for the analysis of Grande events. (From [Haungs03a])

- The KASCADE array[4], an array of detector stations on a $200 \times 200\,\mathrm{m}^2$ area with shielded and unshielded scintillation detectors measuring the electromagnetic and muonic component of an air shower.

- The central detector which is optimised for measuring the core of air showers. Its most prominent part is a large hadron calorimeter. It also contains muon detectors below the calorimeter, a trigger plane inside the calorimeter and detectors for the electromagnetic component above the calorimeter.

- The muon tracking detector, with position sensitive streamer tubes in a shielded tunnel, to measure the tracks of muons.

[4]If in the course of this thesis the term *Array* is mentioned without further reference, then it refers to the KASCADE array.

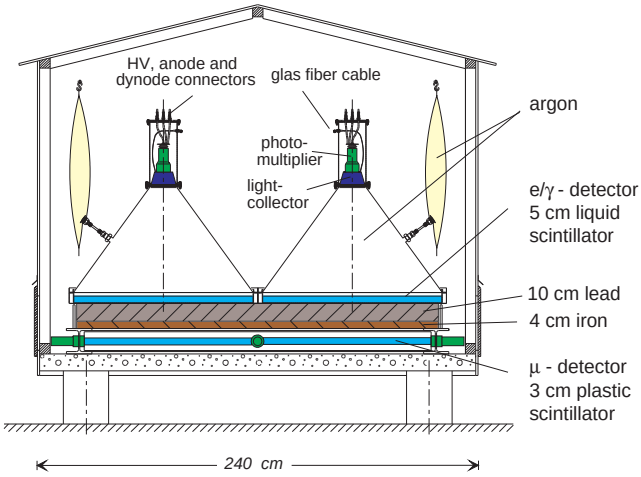

Figure 1.9: Schematic of a station of the KASCADE array. Two e/γ-detector cones are shown standing on top of the lead and iron shielding, below the shielding is the muon detector. (From [Schieler95])

- The Grande array[5], consisting of 37 detector stations covering an area of $0.52\,\mathrm{km}^2$ equipped with scintillation detectors.

- The Piccolo trigger array, a small array of scintillation detectors with the purpose of giving a fast trigger signal for coincidence measurements with all the components of KASCADE-Grande.

As the KASCADE array and to a lesser extend the Grande array are of particular importance to LOPES they are described in more detail.

1.5.1 The KASCADE Array

The KASCADE array consists of 252 detector stations divided into 16 so called clusters (see figure 2.5). The stations are arranged on a regular 16×16 grid with a grid spacing of 13 m, thus covering $\sim 200 \times 200\,\mathrm{m}^2$. At the place of the central detector four stations are missing, one from each of the inner clusters.

In the centre of every cluster there is an electronic container housing the cluster electronics. This electronics consist of frontend electronics, trigger logic, clock and trigger distribution, and controlling computers. The clusters run as individual experiments, each cluster can generate an internal trigger. These local triggers are distributed to all clusters and the other parts of KASCADE.

Figure 1.9 shows a schematic of one of the array stations. The stations of the inner clusters have four e/γ-detectors and no muon detector, while the stations of

[5]Similar to the Array, the term *Grande* is used to refer to the Grande array

the outer clusters have two e/γ-detectors and a muon detector below a shielding of 10 cm lead and 4 cm iron (i.e. 20 radiation lengths).

The casing of an e/γ-detector consists of a cone with a diameter of 1 m at its base, a cylinder on top of the cone, and a lid on top of the cylinder, all made from stainless steel. These three parts are separated by rubber rings and held together by screws to ensure that they are light tight. The inside of the cone is painted with reflecting paint, and the bottom is filled $\sim$ 5 cm high with a liquid scintillator. At the tip of the cone there is a plexiglass light collector on which the photomultiplier rests. This geometry ensures that the delay of the signal is independent of the position at which the particle hits the detector. To protect the scintillator the detector is filled with argon, an external argon bag is used for pressure equalisation. For testing purposes it is possible to input light into the detector via an optical fibre connector. This light is lead by a glass fibre cable onto the light collector.

The muon detectors consist of four quadratic sheets of plastic scintillator in a 2×2 grid, each 90 cm long and wide and 3 cm thick. They are read out with four photomultipliers via wave length shifters at every edge of the scintillator sheets.

1.5.2 The Grande Array

The Grande array covers an area of about $700 \times 750\,\mathrm{m}^2$. The positions of the detector stations are shown in figure 1.8. Each station has 16 unshielded scintillation detectors with a combined area of $10\,\mathrm{m}^2$. The signals are shaped and amplified at the stations and then transmitted to a central data acquisition station.

For the trigger generation the Grande array is logically divided into 18 hexagons of six outer and one central station. In case of a sevenfold coincidence in at least one hexagon a trigger is sent to all parts of KASCADE-Grande.

1.5.3 Air Shower Reconstruction

To be able to form a single datablock for each shower a 1 Hz clock and a 5 MHz clock are centrally generated and distributed to all experiment parts. With these clocks a counter with the number of seconds since 1.1.1970 and a counter with the number of 5 MHz ticks inside this second are formed. Each part of KASCADE-Grande attaches the time-stamp formed by these two values to the data it sends to the central event building software. With this information the eventbuilder can combine all the data from one air shower to a single event data block.

The event data can then be read by the KASCADE-Grande air shower reconstruction program. This program calculates air shower parameters from the raw data. It contains routines for all parts of KASCADE-Grande, so that an analysis can easily combine results from all parts.

From the KASCADE array data the reconstruction program calculates the number of electrons and muons, position of the shower centre, shower direction and a parameter for the steepness of the electron distribution (age-parameter, see eq. 1.1). This is done in three iterative steps. In each of those the number of electrons and

muons in every station and the above mentioned parameters are determined with increasing accuracy. The muon number is given as the total muon number and the so called truncated muon number, i.e. the number of muons in the distance range of 40-200 m from the shower axis. The latter has a smaller systematical error.

The data from just the Grande array yields the number of charged particles, the position of the shower centre, and the shower direction also for air showers that have their centre outside the KASCADE array. In combination with the data from the KASCADE array and/or other KASCADE-Grande parts it is possible to separate the electron and muon number. But while the reconstruction accuracy for the core position and shower direction with the KASCADE array is 1 m and 0.1°, it is only 4 m and 0.18° with the Grande array [Antoni03], [Maier03], [Badea05].

Chapter 2

The LOPES System

2.1 The Hardware of LOPES

The main task of this thesis was to design, build, and operate the LOPES experiment.

LOPES operates in the frequency range of 40 MHz to 80 MHz. This is a band with relatively little RFI (see chapter 4) in between the short-wave- and the FM-band. Additionally this frequency range is low enough that the emission from air showers is strong, but not so low that the background emission from the Galactic plane is too strong.

Although we chose a relatively quiet frequency band LOPES still has to deal with significant RFI (see section 4.1). But LOPES must also be able to detect faint radio pulses from air showers. This leads to two design goals for the hardware. The first is that the noise added by the hardware should be less than the background noise from the sky. As the average sky temperature in our frequency band ranges from 2000 K at 80 MHz to ∼10000 K at 40 MHz this goal is relatively easy to meet. The second goal is that the dynamic range of the system has to be large enough to handle both the RFI and the small signals, i.e. distortions of the signal caused by the RFI in our electronics should be also less than the background noise. This puts a significant restriction on the kind of ADCs we can use, i.e. we cannot use 8-bit ADCs. The availability of ADCs with a sufficient dynamic range limited the bandwidth to 40 MHz and thus prevented us from using the range between 40 MHz and the short-wave-band.

The outline of the hardware used for LOPES can be seen in figure 2.1. It samples the radio frequency signal after minimal analogue treatment without the use of a local oscillator. This approach will allow mass production at low costs in the future.

After determing the basic design, the antennas and the electronic modules were further developed and built at ASTRON as a prototype for LOFAR. As part of this thesis' work the individual parts were integrated into a working system, the data acquisition software was written, and the system integrated into the KASCADE-Grande experiment.

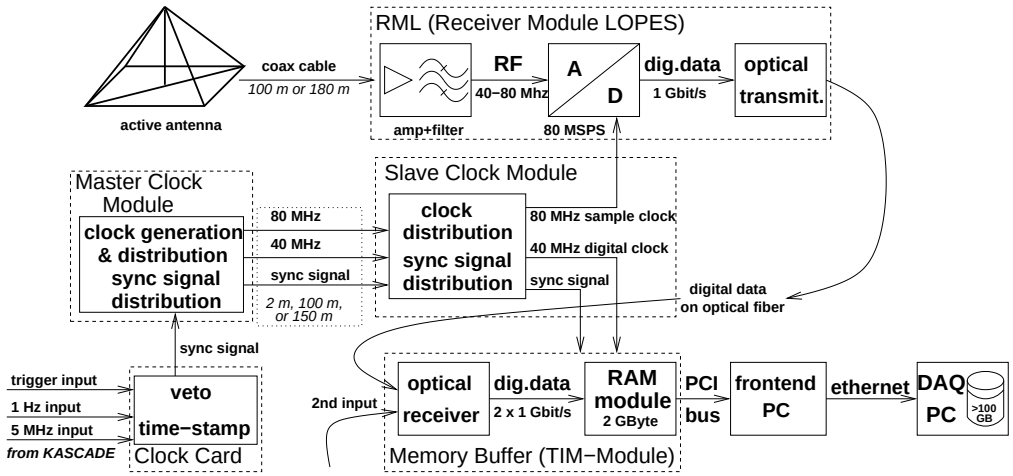

Figure 2.1: Outline of the LOPES hardware. The signal is picked up by the antenna, sent via a coaxial cable to the receiver module, digitised and sent to the memory module. From there it can be read out by the frontend PC and transmitted to the central data acquisition PC. The clock signals are generated by the master clock module and, together with the sync-signal, sent to the slave modules for further distribution.

Integration, test, and dvelopment proceeded in several iterarions. First a four antenna system with prototype electronics was set up at the Max-Planck-Institute für Radioastronomie in Bonn, then it was moved to the site of the Effelsberg telescope. The system for the first phase of LOPES was first set up at ASTRON and then moved to the KASCADE-Grande site. There it first ran with 8 antennas and finally with 10 antennas. For the second phase of LOPES 20 additional antennas were directly set up at the KASCADE-Grande site.

2.1.1 Antenna

The antennas for LOPES are short dipole antennas with an "inverted V" shape. One of the LOPES antennas at the KASCADE-Grande site is shown in figure 2.2. The visible parts are commercial PVC pipes holding the active parts in place, while being transparent to the radiation. The radiator consists of two copper cables extending from the top down two thirds of two opposing edges of the pyramid. The PVC exterior of the antenna resides on an aluminium pedestal. This acts as a ground screen and protects the antenna from being damaged by lawn mowers[1].

This geometry determines the antenna pattern of the single antenna. The pattern, as obtained from simulations [Arts05], is shown in figure 2.3. The half power beam width of the antenna ranges from $\sim 85°$ in the direction parallel to the dipole

[1]The LOFAR antennas will have a different ground screen that does not reside on a pedestal. This changes the antenna pattern slightly at low elevations.

Figure 2.2: One of the LOPES antennas at the KASCADE-Grande site. The active balun resides inside the container at the top of the antenna. The radiator consists of cables in two opposing edges of the pyramid. By choosing the east-west edges our antenna is sensitive to the east-west polarised component of the radiation.

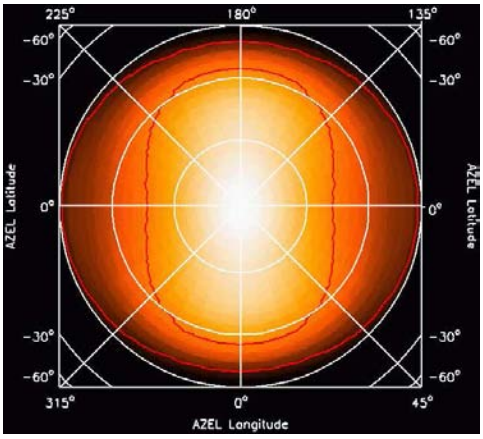

Figure 2.3: Gainpattern of a single LOPES antenna [Arts05]. The vertical direction (azimuth = 0° or = 180°) is the direction perpendicular to the dipole, the horizontal direction is the one parallel to the dipole. The contours are at the 50% and 10% levels.

(E-plane) to $\sim 130°$ in the direction perpendicular to the dipole (H-plane). The antenna pattern also has a minimum at a zenith angle of 90°. This helps suppressing man made RFI.

The four edges can be used for two orthogonal linear polarisations of the signal. If one measures both polarisation directions one can do full polarimetry of the signal. We oriented the diagonals of the antenna in east-west resp. north-south direction, so with one dipole per antenna we can receive either the east-west or the north-south polarised part of the signal. As the cost for the total system is dominated by the electronics, using two dipoles per antenna would mean either twice the cost or half the number of antennas (antenna positions).

Inside the container at the top resides the active balun. Its main functions are balanced to unbalanced conversion, amplification of the signal and transformation of the antenna impedance to the $50\,\Omega$ impedance of the cable. The amplifier is a negative feedback amplifier, with a passive feedback network. The feedback network is designed, so that the resulting input impedance is matched to the output impedance of the radiator over a wide frequency range. This gives sensitivity over a wide frequency range with good linearity and noise performance. The power to the active balun is fed via the signal cable. It is separated from the signal cable with an external (old version) or internal (new version) bias-tee.

2.1.2 Receiver Module

Figure 2.4 shows one of the receiver modules for LOPES (RML). It consists of an amplifier (left), band-pass filter (top), ADC-board (bottom right, partially covered) and an optical transmitter board for the digital data piggybacked onto the ADC-board.

The amplifier is needed to bring the signal level from the antenna to the level needed for the ADC-module. The high background from the Galactic noise and the low absolute power result in relaxed requirements for noise and intermodulation performance of the amplifier. We need at least 16 dB gain, a noise figure of less than 10.3 dB and an output intercept point OIP2 of more than +32 dBm. This can be achieved with a relatively cheap, commercially available amplifier.

Next in the signal path is the anti-aliasing and band-pass filter. This filter should provide the largest usable bandwidth, while suppressing the strong transmitters outside our band of interest. Usable bandwidth is defined as the bandwidth in which we have significant power in our band and where contributions from outside the band are suppressed below the noise level. To suppress contamination from outside our band (especially the FM-Band) a stopband attenuation of 60 dB is needed. Additionally the desire for high usable bandwidth makes steep edges necessary. The filter used for LOPES gives us a usable frequency band from 43 MHz to 76 MHz. (Figure 2.10 shows the shape of the filter in the curve of the receiver module gain.)

The last analogue device in the signal path is the A/D-converter board. It includes an amplifier, that matches the $50\,\Omega$ input impedance of the board to the impedance of the ADC. This amplifier is from the same manufacturer as the ADC

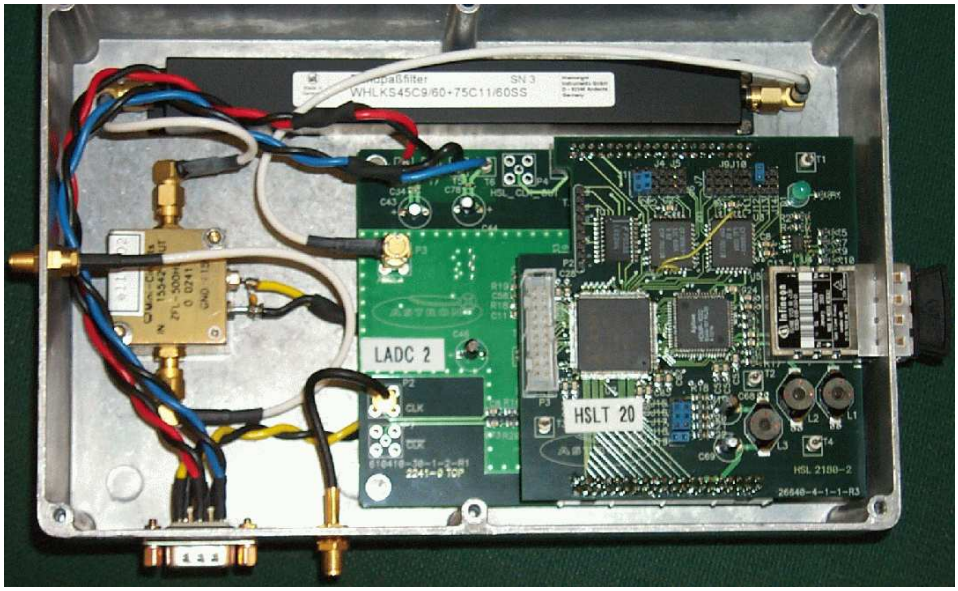

Figure 2.4: A LOPES receiver module with amplifier (left), band-pass filter (top) and A/D-converter board with an optical transmitter board piggybacked onto it (bottom right). The connectors are: signal input (left), power (bottom left), ADC-clock (bottom right) and digital data out (right).

and designed so that it does not distort a signal for the ADC more than the ADC can measure. To detect weak pulses while not saturating the ADC with radio interference we need a dynamic range of about 60 dB. This is achieved by using 12-bit ADCs. The ADCs are running at a converter clock of 80 MHz. Thus we are sampling the signal in the second Nyquist domain of the ADCs.

Piggybacked onto the A/D-converter board is an optical transmitter board. This changes the digital data of the ADCs from an electrical to an optical signal and transmits the data to the backend module.

2.1.3 Digital Backend and Clock Module

The digital data is transferred via fibre optics to the memory modules. These modules have standard PCI-connectors and fit into the front-end PCs. The modules use normal PC133–style computer memory. This makes it affordable to put 2 GByte of memory onto each module. A module has two inputs with ∼1.2 GBit/sec each. It can either read from both inputs simultaneously, or only from one input. This allows it to store up to 6.25 seconds of data using both inputs or even 12.5 seconds of data from one input. Several of these modules can be used together by synchronising them with a common synchronisation-signal. The modules can either start writing the data into their memory after a sync-signal or write data continuously into the

memory, wait for the sync-signal, and stop a predefined time after that signal is received.

To be able to do beam forming with the data, the ADCs have to use the same conversion clock. Even small differences in the frequency of the conversion clock lead to offsets of several samples during the time of one dataset. (E.g. 1 ppm frequency difference at 80 MHz leads to an offset of 80 samples every second.) Also the clock for the ADCs not only needs to be stable over long times, but also over short times. This is particularly true if one uses 2nd Nyquist sampling of the signal. Jitter on the sample-clock distributes part of the power from narrow band RFI over all frequency channels. Sending the clock signal over the optical transmission path adds too much jitter, thus we distribute the clock via coaxial cables. To achieve this the clock for the ADCs is generated with a low noise crystal on a central master clock module and then distributed via slave modules to the receiver modules. From this clock the master module also generates a synchronous clock for the memory modules, and it has an input for a synchronisation-signal. These two signals are also distributed via the slave modules.

To get a KASCADE-Grande style time-stamp a clock card is used that was produced by the Institute of Data Processing and Electronics at the Forschungszentrum Karlsruhe within the scope of this thesis [Kopmann05]. This card fits into a PCI slot, but is accessed via a firewire interface. It has inputs for the 1 Hz and 5 MHz clocks from KASCADE-Grande and for the trigger signal. After a trigger it automatically applies a veto to the trigger input until the event is acknowledged either per hardware or software. An accepted trigger is also given as the synchronisation-signal to the master clock module. It is also possible to generate a trigger via a software command.

2.2 LOPES at KASCADE-Grande

2.2.1 Layout

The layout of the LOPES antennas inside the KASCADE array can be seen in figure 2.5. In the first phase, named LOPES10, had 10 antennas in a cross like pattern around the electronics station with the receiver electronics. In the second phase, called LOPES30, we have 30 antennas, of which 26 are inside the KASCADE array and 4 are outside on a meadow next to the KASCADE array. The positions of the antennas are chosen to make maximum use of the existing cable conduits of the KASCADE array. Only for the antennas on the meadow new cable conduits had to be laid.

For the signal cable between the antennas an the receiver modules we chose RG 213 type cable. This is a standard cable but with a low attenuation[2]. In the first phase we decided to limit the length of the signal cables to 100 m. This limited antenna positions to clusters next to the cluster housing the electronics. The

[2] A datasheet is available at: `http://www.hubersuhner.com`

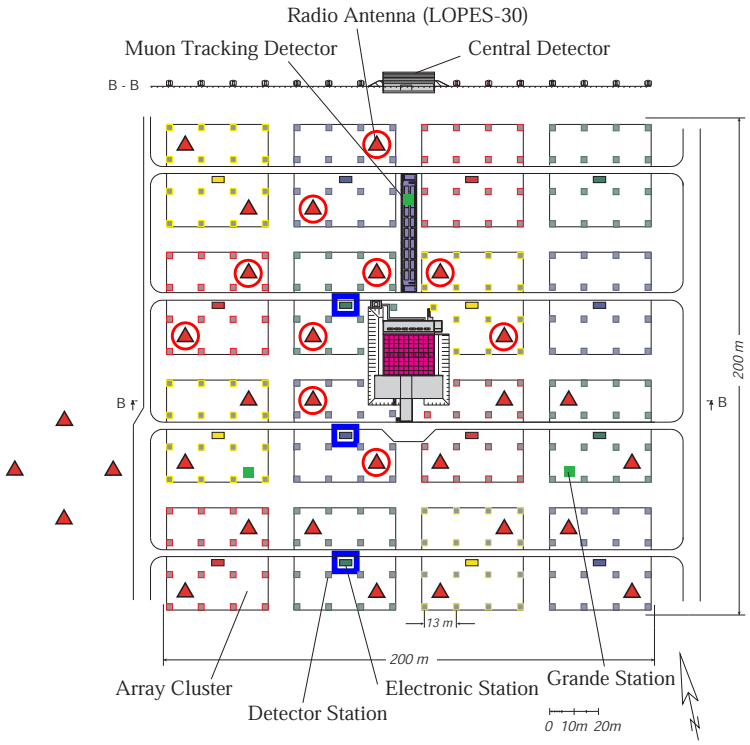

Figure 2.5: Layout of LOPES inside the KASCADE array. The triangles show the positions of the 30 LOPES antennas, the red circles highlight the 10 antennas of LOPES10. The blue squares mark the electronic stations that house the LOPES electronics, each station connecting to ten antennas. The upper station (from cluster 10) was the station used for LOPES10. It now holds the master clock module and the card for the KASCADE timestamp.

experience with the first phase showed that using longer signal cables do not cause noteworthy problems. Now the antennas in clusters next to their electronics are connected with 100 m cables and the antennas farther away are connected with 180 m cables.

The electronics are housed in three racks, each in the electronic station of a different cluster (in clusters 2, 6, and 10). Each station houses a slave clock module, ten receiver modules, five memory modules in three frontend PCs and support electronics (power supplies etc.). In the station of cluster 10 (the upper marked station in fig. 2.5) there is also the master clock module and the clock card for the KASCADE-Grande time-stamp. The clock and sync signals from the master module to the slave modules in the clusters 2 and 6 are transmitted over 100 m, resp. 150 m of RG 52 coaxial cable.

The position of the antennas in relation to each other has been measured with

Antenna	Meters North	Meters East	Meters above Ellipsoid
1	79,600 ±0,084	-45,771 ±0,067	126,159 ±0,092
2	111,415 ±0,018	-64,108 ±0,006	125,694 ±0,024
3	36,110 ±0,000	-84,535 ±0,000	125,812 ±0,000
4	54,611 ±0,065	-52,726 ±0,065	126,099 ±0,104
5	22,670 ±0,063	-34,404 ±0,069	126,079 ±0,084
6	40,831 ±0,071	-2,463 ±0,065	126,226 ±0,088
7	2,104 ±0,063	40,951 ±0,069	126,168 ±0,084
8	34,335 ±0,063	22,658 ±0,067	126,216 ±0,084
9	72,789 ±0,088	-20,850 ±0,074	126,072 ±0,092
10	91,011 ±0,088	11,155 ±0,073	125,968 ±0,094
11	-64,345 ±0,010	-112,076 ±0,008	125,883 ±0,016
12	-45,991 ±0,010	-79,854 ±0,008	125,919 ±0,016
13	-84,675 ±0,010	-36,610 ±0,006	125,965 ±0,016
14	-52,079 ±0,027	-54,421 ±0,010	127,701 ±0,033
15	-91,573 ±0,010	-11,433 ±0,004	126,013 ±0,016
16	-73,148 ±0,016	20,312 ±0,006	126,079 ±0,022
17	-112,227 ±0,024	63,594 ±0,012	126,325 ±0,039
18	-80,274 ±0,065	45,327 ±0,073	126,222 ±0,098
19	-34,731 ±0,025	-23,109 ±0,010	126,020 ±0,033
20	-2,723 ±0,024	-41,349 ±0,016	125,923 ±0,029
21	-13,871 ±0,018	-97,969 ±0,006	126,171 ±0,022
22	4,325 ±0,018	-66,075 ±0,006	126,161 ±0,024
23	-41,364 ±0,018	2,065 ±0,006	125,966 ±0,024
24	-23,055 ±0,008	34,108 ±0,004	125,853 ±0,014
25	-61,704 ±0,022	77,551 ±0,006	126,047 ±0,029
26	-29,850 ±0,010	59,024 ±0,004	125,887 ±0,016
27	-21,860 ±0,025	-152,363 ±0,008	125,808 ±0,031
28	-7,836 ±0,008	-127,748 ±0,006	125,980 ±0,014
29	16,836 ±0,010	-141,780 ±0,004	126,144 ±0,016
30	2,616 ±0,022	-166,447 ±0,008	125,760 ±0,027

Table 2.1: Positions of the LOPES antennas, as taken with the GPS system. The errors are the 95% confidence interval given by the software. The positions are all taken relative to antenna 3. Origin of the x- and y-axis is the centre of the KASCADE array. The height is above an ellipsoid representing sea level.

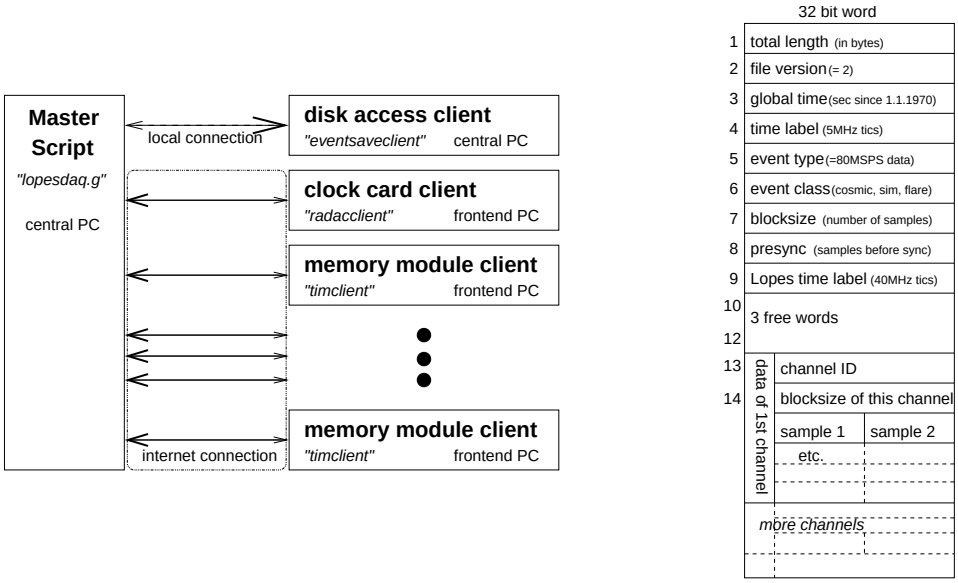

Figure 2.6: Left: Structure of the data acquisition software. Right: Structure of an event file.

high precision with a differential GPS system[3]. For the measurement first the two GPS receivers are initialised by putting them next to each other on a reference position (e.g. at one of the antennas). The one receiver stays at this position and the other is moved from antenna to antenna, recording the GPS data at each position for a while (e.g. 30 seconds). After that the data from both receivers is copied onto a PC, and the supplied software can calculate the relative positions. The positions are listed in table 2.1. The origin of the north and south coordinates is the centre of the KASCADE array, the directions are not aligned with the KASCADE array but point to the geographical north resp. east. The accuracy of this positions, as given by the software, is better than 10 cm with less error in the horizontal plane than in the height.

2.2.2 Data Acquisition

The frontend PCs and the central data acquisition PC are connected with a standard Ethernet. It consists of three switches in the electronic stations which are connected to each other and the central PC with gigabit Ethernet while the frontend PCs are connected with fast Ethernet.

All data acquisition PCs use Linux[4] as the operation system. The software consists of the master script and three types of clients, a client for the disk access, a client to access the clock card and clients to access the memory modules (see left

[3] A Promark2 system from Thales. `http://www.navtechgps.com/supply/promark2.asp`

[4] See e.g. `http://www.linux.org/`

side of figure 2.6). The master script and the disk access client run on the central PC, the other clients run on the frontend PCs. The master script is written in Glish, the script language used by the AIPS++ package [AIPS++]. The clients are programs written in C++ and structured as Glish clients. They can be started from the Glish interpreter and then a script can send and receive messages from them. Glish clients can run on the local computer or on any computer that is reachable via Internet connections. To start the clients without further interaction the (Linux-)user running the data acquisition has to be able to log into the frontend PCs without typing in a password. This is achieved by using ssh[5] and a password-less key pair.

Each event is written into a separate file. To have the data in a small file and to be able to read the event files with other software, the event files are not written with the Glish builtin functions, but an extra client. Event files contains the data in binary form as 32-bit integers for the headers and 16-bit integers (shorts) for the sample data. The structure of an event file can be seen in figure 2.6 on the right side. It consists of an event header that is 12 words long and the channel data. For each channel there is a two word header followed by the sample data with two 16-bit samples in one 32-bit word. For online correlation of events, the eventsaveclient can also handle connections from the central eventbuilder of KASCADE-Grande. To reduce the load on the eventbuilder, only the event header is sent.

The clock card is accessed by the clock card client. It uses a library that in turn uses the firewire interface of the operating system to access the hardware. During the initialisation the global time register on the card is set to the current time on the host computer.

The memory modules are accessed by another client. This client is run once for each memory module, so for 30 antennas 15 clients are used. At the hardware level the modules are accessed by a kernel module, which has to be loaded on the frontend PCs. With this the client can access the memory and the registers on the hardware, control the memory modules, and read out the data. After a module is activated for a measurement, the client waits for a signal from the module that the measurement is done, and then reads out the data and sends it to the master script.

On startup the master script first reads in two setup files. They define where and how to start the clients, how much data from each antenna is saved and where to put the event files. Finally all the clients are started and initialised in turn. In the main loop, first all memory boards are activated, and the veto is released. Then the script waits for a trigger, i.e. for data from the memory boards. After data from all memory boards has arrived the data is copied into the event record. The time stamp from the clock card is read out. A check is done whether all the data belongs to the same event, i.e. whether the data arrived inside a given time window. A good event is then written onto the harddisk, and the loop starts from the beginning.

Glish as an interpreted language is not very fast. Also the script waits untill the data is written onto hard disk before the next measurement is started. Both cause LOPES to have a relatively large dead time between two events. With the current

[5] See e.g. `http://www.openssh.com/`

setup this dead time is about 1.5 seconds.

In each of the three electronic stations there are three frontend PCs. Two PCs housing two memory modules and one PC only one. All frontend PCs are configured identical. At bootup they get their IP-address via dhcp from a server running on the central PC. As the daq-software identifies the frontend PCs by their IP-address all configuration files are concentrated on the central PC.

2.2.3 Setup & Trigger

To get good frequency resolution currently $2^{16} = 65536$ samples are saved per antenna for each event. This equals a total time of ~ 0.82 ms, giving a frequency resolution of ~ 1.2 kHz. The data is selected so that half the data is taken before the sync signal arrived at the frontend electronics and the other half after that. Thus the radio pulse from the air shower is expected in the middle of the data block. It arrives $1.5 - 2\,\mu$s before the sync signal.

The long block size also means that for each event 3.7 MByte are stored for 30 antennas. To not exceed the data handling capacity of the computers a low trigger rate is desirable. Additionally only the events at the highest energies of KASCADE-Grande are of interest for LOPES. For these reasons LOPES is triggered with a special large event trigger. Currently this trigger is formed, when 10 out of the 16 KASCADE array clusters had an internal trigger. This reduces the trigger rate from the 4-5 Hz of KASCADE-Grande to ~ 2 triggers per minute. It is also a compromise between triggering only the very largest events inside the KASCADE array and also triggering large events that have their core outside the KASCADE array but inside the Grande array. The arrival times of the events can be assumed to be Poisson distributed. So the fraction of lost events can be calculated by:

$$\text{fraction of lost events} = 1 - e^{-\,\text{deadtime} * \text{triggerrate}} \tag{2.1}$$

With a dead time of 1.5 seconds and 1/30 Hz trigger rate this means that about 5% of the events are lost.

Currently LOPES is not integrated into the KASCADE-Grande data acquisition system. Once this is done the eventbuilder of KASCADE-Grande will do an online correlation of the KASCADE-Grande and LOPES events. Up to now the correlation of events is done offline on the basis of the time stamps recorded with the KASCADE-Grande data and the LOPES data.

2.3 Delay Calibration

In order to be able to do beam forming, the instrumental signal delays of the different antennas has to be known with good accuracy. Even small errors in the relative delays of the antennas with respect to each other degrade the coherence (see fig. 2.7). The amount of this degradation depends on the specific data. It was shown that a shift of the relative delay by one tenth of a sample time can degrade the coherence

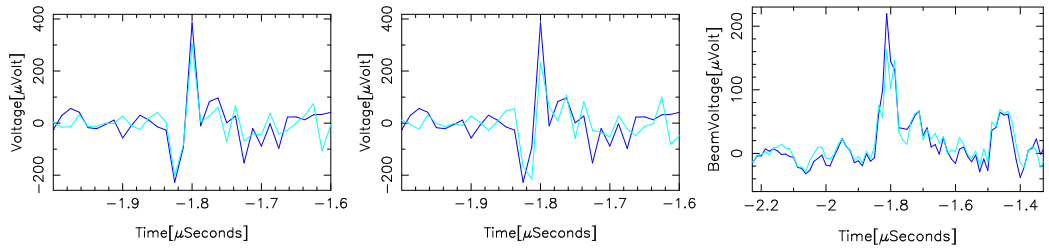

Figure 2.7: Coherence of a radio pulse in two antennas. Traces of the antennas after time shifting with correct delays (left), with an artifical offset of 0.1 sample times (middle), and the formed beam for both cases (right; correct delays in dark blue, with offset in light blue). With the offset the two traces do not fall onto each other anymore, so the coherence is degraded. After beam forming the resulting pulse is smaller, but still there.

by a significant amount, but still yields useful data (for LOPES: 1 sample time = 12.5 ns).

The first step to get a good delay calibration is the design of the system. All channels use the same electronics (amplifiers, filters etc.), so the delays introduced there should be about the same.[6] Wherever possible the length of the cables is the same, and where this is not the case the signal delay of the cable is measured and accounted for.

Tolerances of the electronics, unequal aging of the parts and different temperatures can cause a variation of the delay for the different channels. Additionally the digital electronics can cause the time index of a channel to be off by two samples, due to a glitch in the relative timing of the boards.

2.3.1 Calibration on the Sun

During solar bursts the sun becomes by far the brightest source in the sky at our frequencies. It can even become so bright, that only the strongest RFI sources are visible in a single antenna spectrum. Due to the low spatial resolution of LOPES the sun is seen as a single point. This allows us to use the bursting sun as a calibration source for the relative delays.

This is done by choosing one antenna as a reference, and then do the following for all remaining antennas:

1. Calculate the expected relative time delay to the reference from the positions of the antennas and the position of the sun.

2. Calculate the cross-correlation function for the time series of the antenna and the reference.

[6] Due to financial constraints the 10 antennas of LOPES10 and the 20 antennas of the expansion to LOPES30 have different filters. Whether this will be a problem for the delay calibration remains to be seen.

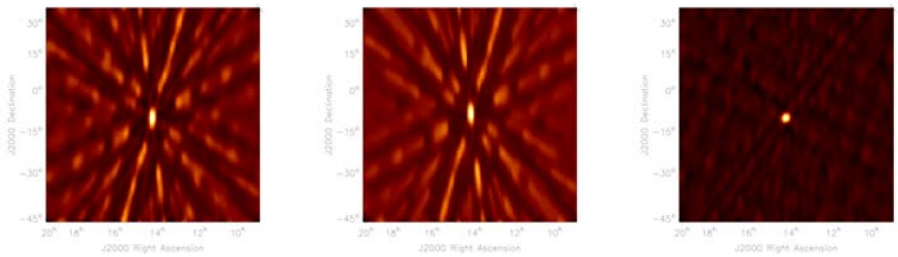

Figure 2.8: Map of the sun during a solar burst. Dirty map (left) in J2000 coordinates and SIN projection, simulation of a point source (middle), clean map (right). The clean map shows only a point source that means that the structure in the dirty map is due to the sidelobes of the antenna array.

3. Find the time delay, at which the cross-correlation function has its maximum.

4. The difference between this time delay and the calculated expected delay is the instrumental delay.

The success of this calibration can be tested by generating a map of the sun. Figure 2.8 shows a raw (dirty) map from 0.82 ms of data for a solar burst at the 28 October 2003 on the left side. The structures around the point in the middle are due to the sidelobes of the antenna array. The sidelobes are rather strong because of the large distances between our antennas. These sidelobes can be computed from the antenna positions with standard astronomical software, e.g., AIPS++ [AIPS++] (figure 2.8 middle). With this information one can reconstruct a clean map of the sun, e.g. with the CLEAN algorithm [Högbom74], where artifacts from the sidelobes are substracted (figure 2.8 right). The fact that the clean map shows only a single point source, shows us that our calibration method works. It can also be used to estimate the size of our beam, which is about 2° FWHM close to the zenith.

2.3.2 Calibration on a TV-Transmitter

By monitoring the relative phases of a TV transmitter we can monitor the phase stability of our system and get time delay calibration values for every day. As the position of the TV transmitter does not change, the relative delays and thus the relative phases of its signal in the different antennas remains constant. Additionally, its picture carrier and the two audio subcarriers are strong enough that they are visible in every antenna and can be easily identified.

The signal from the TV transmitter does not have enough fine structure to allow us to directly get the relative delay via the cross-correlation. Checking the relative phases of just a single frequency cannot detect larger shifts due to the ambiguousness of the phase. But by checking three frequencies this ambiguity can be reduced so

far that not only delays by a small fraction of a sample time but also shifts of an integer number of samples can be detected.

Unlike the calibration on the Sun this method uses the frequency domain data, i.e. the Fourier transformed time domain data. Again, the delays are measured relative to a reference antenna. For the other antennas the delay corrections are calculated in the following way:

1. Determine the exact frequencies of the three carrier signals, by looking for the bins with the most power in the given frequency ranges.
2. Calculate the relative phases for these frequencies.
3. Subtract the expected phases to get residual phases
4. If the absolute sum of these residual phases is big ($> 150°$ i.e. an equivalent delay of maximal 0.18 sample times) then shifts by an integer number of samples between -32 and +32 are tried.
5. If none of these shifts produces small residual phases the corresponding antenna is flagged as bad.
6. The residual phases are converted to time delays. The average over these values plus an applicable shift from step 4 is returned as the result.

The resulting delay corrections for one antenna over a few days are shown in figure 2.9. The three spikes belong to events where the algorithm failed. The delay-axis is given in sample times, so even without the correction the delay error stays within the ± 0.1 sample times range.

2.4 Gain Calibration

With a setup like LOPES the directly measured values are ADC-counts. The values of interest are the field strength of the radio pulse or the flux from a continuous astronomical source. To get from the recorded ADC-values to values for the field strength one has to consider the properties of the ADC, the gain and attenuation of the electronic parts in the signal chain and the gain of the antenna.

One way to measure the effects of these parts is to measure them all together. This can either be done by imaging a known astronomical source, or by measuring the signal from a transmitter with known power. The first method requires that the system and RFI noise is low enough, so that it is possible to image at least the strongest astronomical sources. For the second method one has to place a suitable transmitter in the desired direction far enough away from the antenna, so that it works in the far-field. In our case ($\lambda \approx 7\,\mathrm{m}$ and an antenna that looks upwards) this means placing a transmitter several meters above our antenna. The noise at the KASCADE-Grande site is too strong to get an image of even the brightest calibration sources. The second phase of LOPES is now calibrated by measuring a

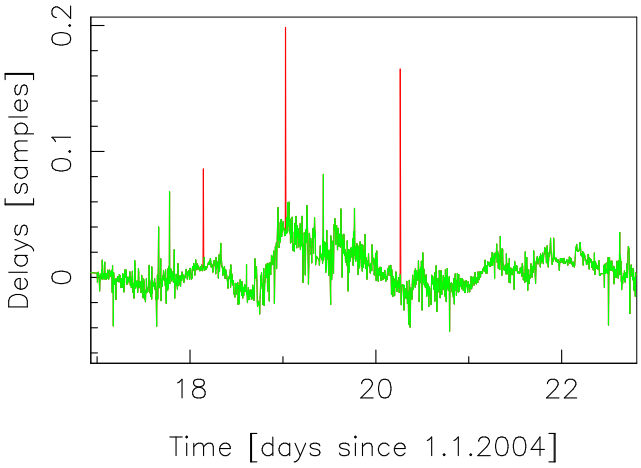

Figure 2.9: Time delay deviations for one LOPES antenna, as computed from the relative phases of a TV transmitter. The three flagged spikes are where the algorithm failed e.g. due to excessive noise.

signal from a calibration transmitter [Hakenjos05]. As the first phase of LOPES used slightly different hardware this kind of calibration is not available for LOPES10.

Another way is to measure the effects of all parts separately and then combine them, which is what we did here.

2.4.1 A/D-Converter

To get the power at the ADC-inputs from the measured ADC-counts, one first has to calculate the voltage by scaling the measured counts with the ratio of the maximum voltage to the maximum counts. The power at the ADC-inputs for a single sample can then be calculated with the formula for DC-currents:

$$P_{ADC} = \frac{U_{ADC}^2}{R_{ADC}} = \frac{(\text{ADC counts}\frac{\text{max Voltage}}{\text{max counts}})^2}{R_{ADC}} \tag{2.2}$$

Here P_{ADC} is the power into the ADC, U_{ADC} is the voltage at the ADC-Inputs, R_{ADC} is the input impedance of the ADC, $ADC\,counts$ the value given by the ADC for this sample, and $max\,Voltage$ is the maximum Voltage at which the ADC generates the value $max\,counts$.

To ease the calculations we assume, that the input impedance of the ADC is $50\,\Omega$. In reality the impedance of the ADC-IC has a different value, but the ADC-Board has a $50\,\Omega$ input impedance. So any effects of this different impedance can be accounted for by choosing an appropriate calibration value for the amplifier on the ADC-Board. So although the "power into the ADC" is not the real power that goes into the ADC-IC, it is still a valid tool for our calculations.

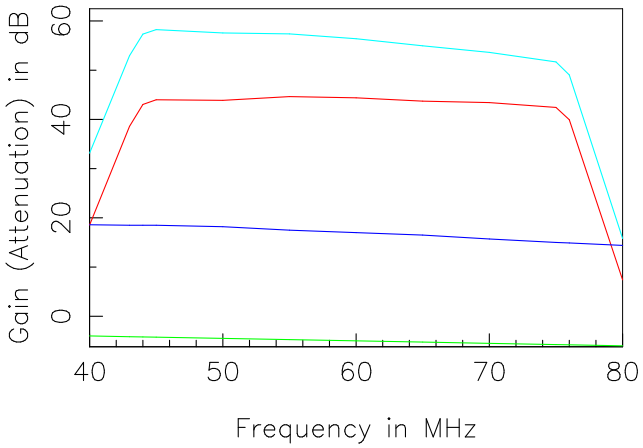

Figure 2.10: Gain of the different parts of the electronic chain: Receiver module (red), 100 m signal cable (green), active balun (dark blue), and total gain (light blue). The negative values for the signal cable marks it as an attenuator, the shape of the receiver module gain is dominated by the filter.

2.4.2 Electronic Gain

The next step is to consider the gain of the electronics in the signal chain. For the purpose of actual measurements the signal chain of LOPES can be separated into the following parts:

- the gain and attenuation of the parts inside the receiver module
- the attenuation of the signal cable
- the gain of the active balun at the antenna

The gain of the receiver module can be measured by applying a signal with known strength to the input of the receiver module and comparing it with the digital output. By measuring at different frequencies one can get the frequency dependent gain curve of the receiver modules. This gain curve is shown in figure 2.10 in red. The shape of this curve is dominated by the anti-aliasing filter inside the receiver-module.

Due to the relatively low frequencies the attenuation of the connectors and patch cables is negligible. The long signal cable does have some significant attenuation. This attenuation can either be measured, e.g., with a signal-generator and spectrum analyser, or be taken from the literature. The attenuation (i.e. negative gain) for a 100 m cable is shown in figure 2.10 in green.

Measuring the gain of the active balun is not as easy. As the gain of the active stage depends on the output impedance of the radiator, measuring with the 50 Ω impedance of standard test equipment would lead to false results. Better results can be obtained by putting an impedance converter between the test equipment and the input of the active balun, that changes the impedance seen by the balun to that

of the radiator. As the impedance of the radiator is only known from simulations and can only be approximately reconstructed with an impedance network, this is a major source of uncertainties. The results of the measurements with an impedance converter are shown in figure 2.10 in dark blue.

The total gain curve can be seen in figure 2.10 in light blue. This values can be used to convert the power as measured at the input of the ADC into the power into the input of the active balun. Assuming a good match of the impedances the latter is equal to the power available at the foot of the radiator.

2.4.3 Antenna Gain

Due to the reciprocity theorem the directivity or gain of an antenna in a transmitting situation is the same as in a receiving situation [Rohlfs86]. The gain of a transmitting antenna $G_{(\theta,\phi)}$ in a given direction (θ, ϕ) is defined as the ratio of the power transmitted in that direction $P_{(\theta,\phi)}$ to the power an isotropic radiator would radiate in that direction P_{iso}:

$$G_{(\theta,\phi)} = \frac{P_{(\theta,\phi)}}{P_{iso}} = \frac{4\pi P_{(\theta,\phi)}}{P_{total}} \tag{2.3}$$

Here P_{total} is the total power transmitted by the antenna.

Measuring the gain of an antenna, requires having a transmitter in the far-field of the antenna. Using a known astronomical source as transmitter is prevented by the strong RFI at the site. It is planed to measure the antenna pattern with a calibrated transmitter but this has not been done yet. The antenna gain can also be calculated from the geometry of the antenna. This has been done [Arts05] and the resulting antenna pattern can be seen in figure 2.3. At the zenith it has a value of $G_{max} \approx 5$ with only little dependence on the frequency. Measurements with the LOFAR-ITS, that uses similar hardware but is placed at a site with very little RFI, have shown that these calculations are quite reliable [Spreeuw05].

Parts of the literature distinguish between the directivity as defined above and the gain of the antenna, which includes losses inside the antenna. Due to losses the power transmitted by the antenna can be less than the power fed into the antenna. In our case the antenna consists of two relatively thick copper wires surrounded by PVC piping, so we do not expect significant losses in the antenna. Additionally we cannot distinguish between losses in the antenna and less gain from the active balun.

2.4.4 Calculating the Field Strength

The power density of an electromagnetic wave is given by the Poynting vector $|\mathbf{S}|$. In the atmosphere (approximated as vacuum) this can be written as the square of the electric field [Rohlfs86]:

$$|\mathbf{S}| = \frac{1}{c\mu_0}|\mathbf{E}|^2 \tag{2.4}$$

The factor, that determines the amount of power an antenna extracts from this is called the effective aperture:

$$A_{eff} = \frac{P_{Ant}}{|\mathbf{S}|} \tag{2.5}$$

(Assuming that the radio wave is 100% polarised in the polarisation direction of the antenna.) The effective aperture is related to the antenna gain by:

$$A_{eff} = \frac{G\lambda^2}{4\pi} = \frac{Gc^2}{4\pi\nu^2} \tag{2.6}$$

(λ and ν being the observing wavelength and frequency.) Thus the power picked up by the antenna relates to the electric field by:

$$P_{Ant} = \frac{Gc}{4\pi\nu^2\mu_0}|\mathbf{E}|^2 \tag{2.7}$$

If the bandwidth of the signal is larger than the bandwidth of the receiver, one measures only parts of the signal, so the measured values depend on the receiver bandwidth and may depend on the receiver frequency. In the case of short time pulses one can make the assumption that the spectrum is flat over the limited receiver bandwidth.[7] Thus to get values that are comparable between experiments with different bandwidth, one can divide the measured peak field strength by the effective receiver bandwidth.

Together with the results from the previous sections one can calculate the field strength per unit bandwidth from the measured ADC values:

$$\varepsilon_\nu = \frac{|\mathbf{E}|}{\Delta\nu} = \frac{1}{\Delta\nu}\sqrt{\frac{4\pi\nu^2\mu_0}{G_{(\theta,\phi)}c}P_{Ant}} = \frac{1}{\Delta\nu}\sqrt{\frac{4\pi\nu^2\mu_0}{G_{(\theta,\phi)}c}K_{ele}\frac{V_{ADC}^2}{R_{ADC}}} \tag{2.8}$$

Here $\Delta\nu$ (= 33 MHz) is the bandwidth, ν (= 60 MHz) is the observing frequency, $G_{(\theta,\phi)}$ is the (direction dependent) gain of the antenna, K_{ele} is the (frequency dependent) correction factor for the electronics (i.e. the total gain of the electronics), V_{ADC} is the voltage measured by the ADC, and $R_{ADC}(= 50\,\Omega)$ is the input impedance of the ADC, that was used when calculating the correction values (In brackets the values for LOPES).

One has to keep in mind, that the field strength calculated that way is just the field strength in the polarisation direction of the antenna. To get information about the perpendicular polarisation direction, one has to use another channel in which the antenna is configured for the other polarisation direction.

[7] As the width of the observed pulses is the width of the impulse response of the anti-aliasing filter (see section 3.3.8) this assumption is valid for LOPES, while in general it is not.

Chapter 3

The LOPES Analysis Software

For the analysis and the visualisation of the LOPES data a new software was written [BährenLT]. It is based on AIPS++ [AIPS++] and is written mostly in Glish with a few computation intensive parts written in C++.

The software consists roughly of the following parts:

1. the data kernel. This is a kind of execution tree embedded in a data object where data can be put into, worked upon, and extracted afterwards. It also allows generation of new data sets, either with completely new data, or data referring to another dataset, e.g. the filtered or beamformed version of a dataset.

2. either seen as part of the kernel or as something behind the kernel, are routines that do the calculations inside the kernel. E.g. they define that the voltage values are derived from the raw ADC values and also implement the necessary calculations.

3. routines that use the database methods to access data. They can use the data either to produce output for the user or to calculate values that are again put into the kernel. One example for the latter is the function that calculates the delay calibration values from the TV transmitter.

4. the graphical user interface (see figure 3.1). It can display the data in many different combinations and can be used to initiate the common computing tasks.

5. and a myriad of small and not so small functions, that are called by the other parts.

Contributions within the scope of this thesis were the design of the software, a large part of the structure of the data kernel, most of the functions that do the calculations inside the kernel, many of the helper functions, and most of the routines for the analysis of cosmic rays.

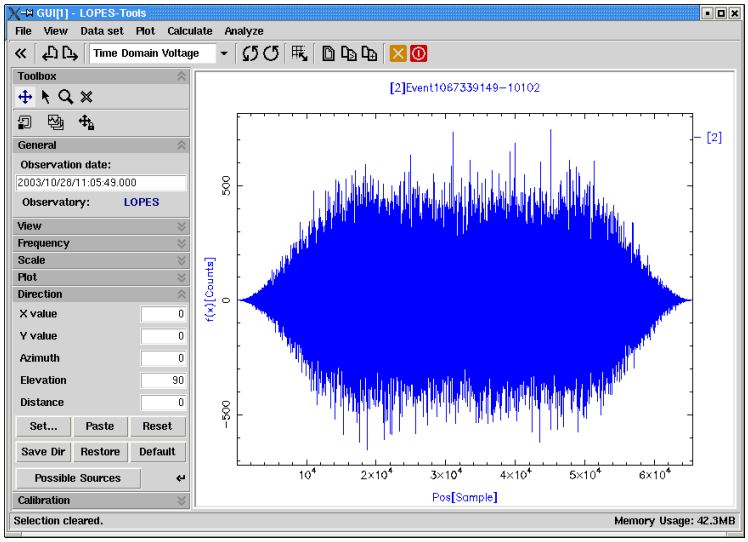

Figure 3.1: The GUI of the LOPES-Tools software. At the top it has a menu bar and then a tool bar with the most common tools. The major part of the GUI is taken by the plotter window, in which the selected data is displayed. Left of the plotter there are a number of tool panels. At the bottom there is a status bar with information about the current status of the software.

The software can load and work on data from different sources: the combination of external receiver and ADC-card we used for RFI measurements, the LOPES and ITS hardware, and from a Tektronix oscilloscope. The structure of the software makes it quite easy to adapt it to data from other sources, as long as the data is time domain data sampled on a regular grid.

This flexibility is also the cause for the drawback of the software. Being easily extended it has now evolved into a program with over 37000 lines of Glish code. Even with most of that code normally not executed some common tasks now take a long time to execute, not because of computing intensive tasks but just because of the amount of code the Glish interpreter has to execute. A major rewrite of the program is already planned, its goal is to implement most of the functionality not in Glish but in C++. Here I will not go into the details of the software, but describe the algorithms used.

3.1 Astronomical Maps

An astronomical map is a two-dimensional representation of the brightness distribution on the sky. As the LOPES antennas are sensitive to nearly all the sky above them and we store the whole waveform information for every antenna, it is possible to generate a map of the sky above the horizon from a single dataset (see figure 3.2).

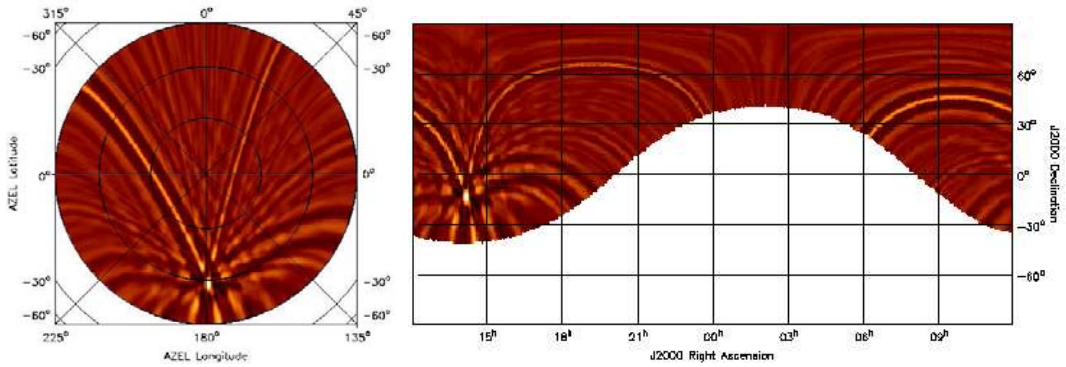

Figure 3.2: Left: Map of half the sky in AZEL (azimuth elevation) coordinates and ZEA (zenithal equal area) projection. Generated from a dataset taken during a solar burst. The bright spot at 179° azimuth 28° elevation is the sun, the lines in the map are generated by the sidelobes of LOPES. Right: The same image but in J2000 coordinates and CAR (plate carée) projection.

To get a flat two-dimensional representation one has to project the sphere of the sky onto a flat surface. For this there are many different projections in use [Calabretta02]. This is especially important for large maps, where a Cartesian approximation does not work anymore. There are also different coordinate systems, some are fixed on the sky and others giving directions relative to the telescope. Having our software based on an astronomical software package has the advantage that there are already routines for the conversion of directions from one set of projection & coordinate system to another, for the handling and display of the maps, etc. (The step from the left to the right image in figure 3.2 is essentially one call in AIPS++.) These routines can be used to convert the position of each pixel in a given map frame to the azimuth-elevation coordinates which we can use for the beam forming. The beam forming is then used to calculate the brightness of the pixel.

3.1.1 Beam Forming

The essence of beam forming is to add the signals from different antennas in order to achieve sensitivity to one direction. This direction is determined by time shifts of the signals from the antennas. Although beam forming is used for all kinds of signals it is easily depicted with radio pulses. As an example figure 3.3 shows the geometry of the source and two antennas. A pulse originating at the source will first arrive at antenna 2 and then at antenna 1. To have the pulse at the same position in both datasets the dataset of antenna 1 has to be shifted in relation to the one from antenna 2 by the delay that corresponds to the distance from antenna 1 to point A. If both datasets are then added up, the pulse will be enhanced in the resulting data, while a pulse from another direction will be smeared out. The same is true for continuous signals from a source. If one chooses not antenna 2 but a point in

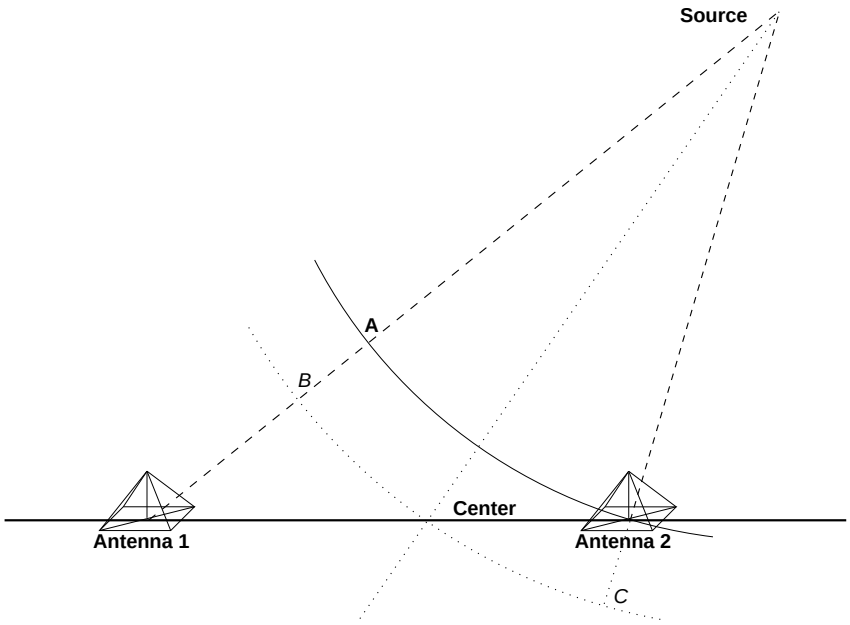

Figure 3.3: Geometry within the plane containing the source point and antennas 1 and 2. A radio pulse from the source point first arrives at antenna 2 and later at antenna 1.

between the antennas as the reference position, then the data from both antennas has to be shifted (e.g. antenna 1 by the delay ant. 1 to point B and antenna 2 by ant. 2 to point C in figure 3.3).

To calculate the geometric delays we first transform the antenna positions into the coordinate system aligned to the direction of the source:

$$\begin{pmatrix} x'_i \\ y'_i \\ z'_i \end{pmatrix} = \begin{pmatrix} -\sin(\phi) & \cos(\phi) & 0 \\ \sin(\theta)\cos(\phi) & \sin(\theta)\sin(\phi) & -\cos(\theta) \\ \cos(\theta)\cos(\phi) & \cos(\theta)\sin(\phi) & \sin(\theta) \end{pmatrix} \begin{pmatrix} x_i \\ y_i \\ z_i \end{pmatrix} \tag{3.1}$$

Here x_i, y_i, z_i are the antenna positions relative to a reference position; ϕ is the azimuth angle and θ the elevation of the given direction[1]; x'_i, y'_i, z'_i are the antenna positions in the source coordinate system, whose z-axis points in the direction of the source.

If the incoming signal is a plane wave (i.e. the source is far away) then the relative distance is z'_i and the delay is z'_i/c. If the signal is a spherical wave with a radius of curvature of R_{curv} (i.e. a signal like that from a point source at $(0, 0, R_{curv})$ in source coordinates), then the relative distances are:

$$r_i = \sqrt{x_i'^2 + y_i'^2 + (R_{curv} - z'_i)^2} - R_{curv} \tag{3.2}$$

[1]For close sources this is the direction from the phase center of the antenna array to the source.

With the delays being r_i/c.

To efficiently do shifts by sub-sample steps, the shift itself is done by Fourier transforming the time domain data to the frequency space and then multiplying a phase gradient to the data. Adding the data from all antennas together and squaring the result directly gives the spectral power distribution for this pixel:

$$P(\vec{\rho})[\omega] = |S(\vec{\rho})[\omega]|^2 = \left| \sum_{i=1}^{N_{Ant}} w_i(\vec{\rho})[\omega] s_i[\omega] \right|^2 \tag{3.3}$$

With $P(\vec{\rho})$ being the power in the direction $\vec{\rho}$, $S(\vec{\rho})$ the beam formed data, N_{Ant} the number of antennas, $w_i(\vec{\rho})[\omega] = e^{i\omega r_i/c}$ the weighting factor of the phase gradient, and $s_i[\omega]$ the frequency domain data of the single antennas.

3.1.2 Long Integrations

To get good sensitivity one wants to have long integration times, i.e. long datasets. To be able to handle these long datasets, they are divided into blocks and the spectral power distribution is averaged over all blocks:

$$P(\vec{\rho})[\omega] = \left\langle |S(\vec{\rho})[\omega]|^2 \right\rangle = \frac{1}{N_B} \sum_{k}^{N_B} |S_k(\vec{\rho})[\omega]|^2 \tag{3.4}$$

If this is done for all pixels in a map then the required computing time is proportional to: $T_{computing} \propto N_{Pixel} * N_{Block} * N_{Ant}$. That means computing a large map (large N_{Pixel}) with a long integration time (large N_{Block}) takes a lot of time. With 10 antennas, 1 GByte data per antenna, and a map of a few thousand pixels it takes from several days up to a few weeks.

A better way can be obtained by separating the dependencies on the block index and the direction (i.e. pixel index) in equation 3.4:

$$\begin{aligned}
P(\vec{\rho})[\omega] &= \frac{1}{N_B} \sum_{k}^{N_B} |S_k(\vec{\rho})[\omega]|^2 = \frac{1}{N_B} \sum_{k}^{N_B} \overline{S_k(\vec{\rho})[\omega]} S_k(\vec{\rho})[\omega] && (3.5)\\
&= \frac{1}{N_B} \sum_{k}^{N_B} \overline{\left(\sum_{i=1}^{N_{Ant}} w_i(\vec{\rho})[\omega]\, s_{ik}[\omega] \right)} \left(\sum_{j=1}^{N_{Ant}} w_j(\vec{\rho})[\omega]\, s_{jk}[\omega] \right) && (3.6)\\
&= \sum_{i,j}^{N_{Ant}^2} \left(\overline{w_i(\vec{\rho})[\omega]}\, w_j(\vec{\rho})[\omega] \right) \left(\frac{1}{N_B} \sum_{k}^{N_B} \overline{s_{ik}[\omega]}\, s_{jk}[\omega] \right) && (3.7)\\
&= \sum_{i,j}^{N_{Ant}^2} \mathbf{W}_{ij}(\vec{\rho})[\omega] * \langle \mathbf{C}_{ij}[\omega] \rangle && (3.8)
\end{aligned}$$

Thus one can in a first step calculate the (frequency dependent) cross-correlation matrix $\langle \mathbf{C}_{ij}[\omega] \rangle$ for all antennas and in a second step multiply it with the weighting

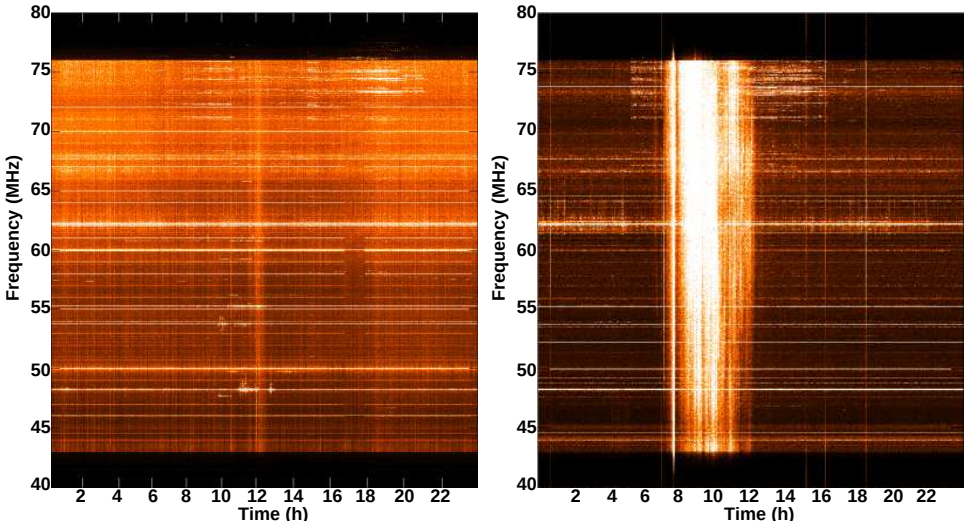

Figure 3.4: Left: Dynamic spectrum for one day (29. July 2004). Horizontal lines are caused by constant RFI transmitters, e.g. the TV-transmitter at $\sim 62\,\mathrm{MHz}$. The vertical lines are caused by the change in broadband noise, which is primarily pulsed RFI. Right: Dynamic spectrum for the 28. October 2003. The bright vertical band is caused by a massive solar burst.

matrix $\mathbf{W}_{ij}(\vec{\rho})[\omega]$ for each pixel. This makes the required computation time proportional to: $T_{computing} \propto N_{Pixel} * N_{Ant}^2 + N_{Block} * N_{Ant}^2$. If both $N_{Pixel} \gg N_{Ant}$ and $N_{Block} \gg N_{Ant}$ this can save a lot of computing time. In the case of the 10 antennas, 1 GByte per antenna example the calculation of the cross-correlation matrix is done over one night, and calculation a map of 300×300 pixels takes less than three hours. The theory behind this is the same that allows to time-integrate the visibility with a "classical" radio interferometer.

3.2 Dynamic spectra

A good way to get an overview of the RFI situation and its change over time is to plot the received power over frequency and time, like it is done in figure 3.4. In such a plot emitters at a constant frequency show up as horizontal lines, changes in the amount of broadband noise form vertical features.

We generate these dynamic spectra by calculating the spectral power density for each LOPES event we have recorded and plotting the data from the events next to each other [NiglDS]. This gives us a time axis that even if it is irregular on small time scales is quite regular on larger time scales.

In these plots it is possible to see when RFI transmitters are turned on or of. E.g. in the left panel of figure 3.4 between 17 and 18 hours a number of lines vanish, this makes it probable that they are emitted by the same source (e.g. in this case

the KASCADE hadron calorimeter). It is also possible to see transient events in this plots. In the right panel of figure 3.4 there is a bright vertical band that is caused by a solar burst.

3.3 Air Shower Events

The goal of the processing of air shower events is to reconstruct the radio field strength of the pulse emitted by the air shower. Processing of air shower events proceeds in the following steps:

1. Correlation between LOPES and KASCADE-Grande events
2. Selection of interesting events
3. Fourier transforming the data to the frequency domain
4. Correction of instrumental delays from the TV-transmitter
5. Frequency dependent gain correction
6. Suppression of narrow band RFI
7. Flagging of antennas with high noise
8. Correction of trigger delay
9. Beam forming in the direction of the air shower
10. Quantification of peak parameters
11. Optimising the radius of curvature
12. Identification of good events

3.3.1 Correlation between LOPES and KASCADE-Grande

A modified version of the KASCADE-Grande air shower reconstruction program was written that writes out text files containing the KASCADE-Grande time stamp and the results of the KASCADE array reconstruction. In these files only events that satisfy the conditions for the large event trigger for LOPES are written. These files contain for each event:

- event and run number
- exact event time (global time, time label, ns-offset, fit offset and time of day)
- position of the shower core
- azimuth and zenith angle

- electron number and truncated muon number
- the energy deposit in the detector stations close to some antennas

These files are then read by the LOPES software, and a list of all LOPES events is generated that spans the same time as the KASCADE-Grande events. These two lists are merged by stepping through the KASCADE-Grande events and searching for a LOPES event that was recorded at about the same time as the KASCADE-Grande event. If a LOPES event would match two KASCADE-Grande events, it is associated with the first one as the second trigger from KASCADE-Grande fell probably in the dead time of LOPES. This results in a list with the KASCADE-Grande data and the filename of the corresponding LOPES events.

3.3.2 Event selection

This off-line correlation is done for all events. The next steps (steps 3–11) are done in an automatic pipeline. As this pipeline takes a few minutes per event only selected events are processed. These events are selected by KASCADE-Grande data according to the goals of the analysis, see section 5.2.

3.3.3 Fourier Transform

Steps 4–6 take place in the frequency domain, so first the time domain data is Fourier transformed into the frequency domain. To reduce leakage the time domain data is scaled with a modified Hanning window. The modified Hanning consists of the first half of a Hanning in the first quarter, the second half of the Hanning in the last quarter and is flat in between. Figure 3.1 shows nearly flat noise scaled with this function in the plotter window of the GUI. This modified Hanning has the advantage of reducing the leakage while not changing the central part of our data with the pulse from the air shower.

3.3.4 Delay and Gain Correction

The algorithm used for the determination of instrumental delays is described in section 2.3.2. The delay corrections obtained this way are added to the other delays and applied during the beam forming process.

The gain calibration values from section 2.4.2 are multiplied to the data. In this step the frequencies outside our band are multiplied by a smaller number, thus effectively removing them.

3.3.5 Suppression of Narrow Band RFI

Narrow band RFI occupies only few channels in frequency space, while a short time pulse is spread over all frequency channels. So by flagging the channels with RFI one can greatly reduce the background without affecting the air shower pulse much. After gain calibration the noise floor inside our frequency band is nearly flat. So

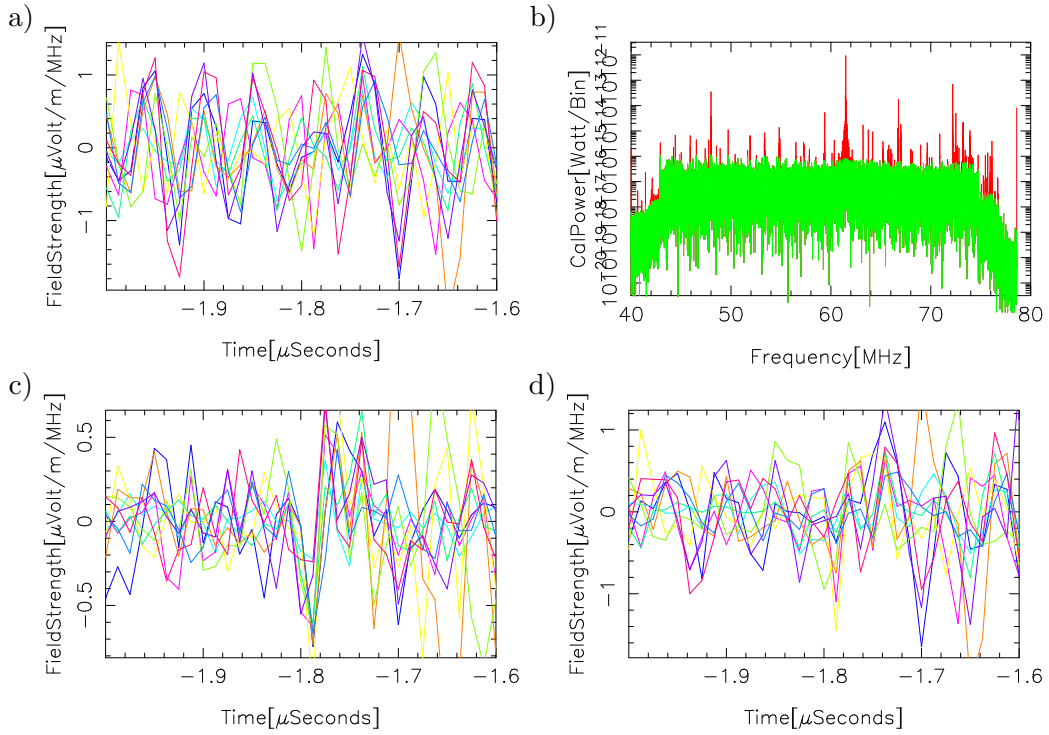

Figure 3.5: a) Section of the unfiltered data. The different colours show traces from different antennas. b) Gain calibrated power spectrum of one antenna with a blocksize of 65536 samples. The red spikes sticking out from the noise floor are narrow band RFI. In green the spectrum after filtering. c) Filtered data, after filtering with a blocksize of 65536 samples. A coherent pulse at $-1.78\,\mu$s is clearly visible. d) Filtered data, but with a blocksize of 128 samples (i.e. 4 times the plotted data). In contrast to c) the coherent pulse is not easily visible.

the amplitude spectrum is fitted with a line to determine the reference value at each point. All points that deviate more than $3\,\sigma$ from this are replaced by the reference value. The parts left and right outside our band are fitted extra, to remove RFI that otherwise would not be filtered. The whole process is done two times to reduce the effect that the RFI influences the fit and biases the reference values. The ratio between the filtered and unfiltered spectrum is used as a weight for the (complex) frequency space data.

Figure 3.5 illustrates the effect of this. Panel a) shows a section of unfiltered data with traces for all antennas. Panel b) shows the power spectrum of one antenna before and after the filtering. After filtering the RFI lines stay in the region of the noise. Panel c) shows the time domain data after the filtering. A coherent pulse at $-1.78\,\mu$s is clearly visible (i.e. all the traces fall onto each other). Panel d) shows the effect of insufficient frequency resolution. Less frequency resolution has two effects.

The first is that with each filtered line a greater portion of the radio pulse is cut away. The second is that RFI is more prone to be hidden in the noise and thus not filtered. In this example the second effect is dominant, the amplitude of the signals is only a little lower than in the unfiltered data.

3.3.6 Flagging of Antennas

Antennas are flagged and not used if:

- They have an unusual amount of noise, i.e. their peak value is significantly larger than those of the other antennas.
- They have an extremely small signal, e.g. because they were not connected.
- They are standing next to the muon tracing detector and the shower core falls on top it. In this case lots of particles penetrate the shielding of the detector and the detector generates a large amount of RFI.
- The antenna is manually deselected.

3.3.7 Beam Forming

The beam forming is done into the direction of the air shower given by KASCADE-Grande. The geometrical delays are calculated as described in section 3.1.1. As the reference position for the calculation of the geometric delays we choose the position of the shower centre. This shifts our data, so that the pulse is at a certain point in time. This point is given by the time it takes the KASCADE array to generate the large event trigger. This time can be determined by calculating when the shower front reached the tenth cluster. By subtracting this time from the delays the air shower pulse is usually at a fixed point in our data.[2]

The geometrical delays (see section 3.1.1), the trigger delay and the delay corrections are added to give the final delays. The shift itself is done by multiplying a phase gradient to the frequency space data before transforming it back to the time domain. From the shifted data we calculate several so called beams, that combine the data in different ways:

- The data from all antennas is added pixel by pixel, but then normalised by the number of antennas to have values comparable to a single antenna.

$$f[t] = \frac{1}{N} F[t] = \frac{1}{N} \sum_{i=1}^{N} s_i[t] \tag{3.9}$$

[2] A situation in which the air shower pulse is not at the expected point in our data can be, when the trigger signal begins while our veto is still active and the veto is removed while the trigger signal is still there. In this case the time of the synchronisation signal is not given by the trigger signal, but by the release of the veto. But these kinds of events are very rare, so one can either correct those manually, or handle them as a non-detection.

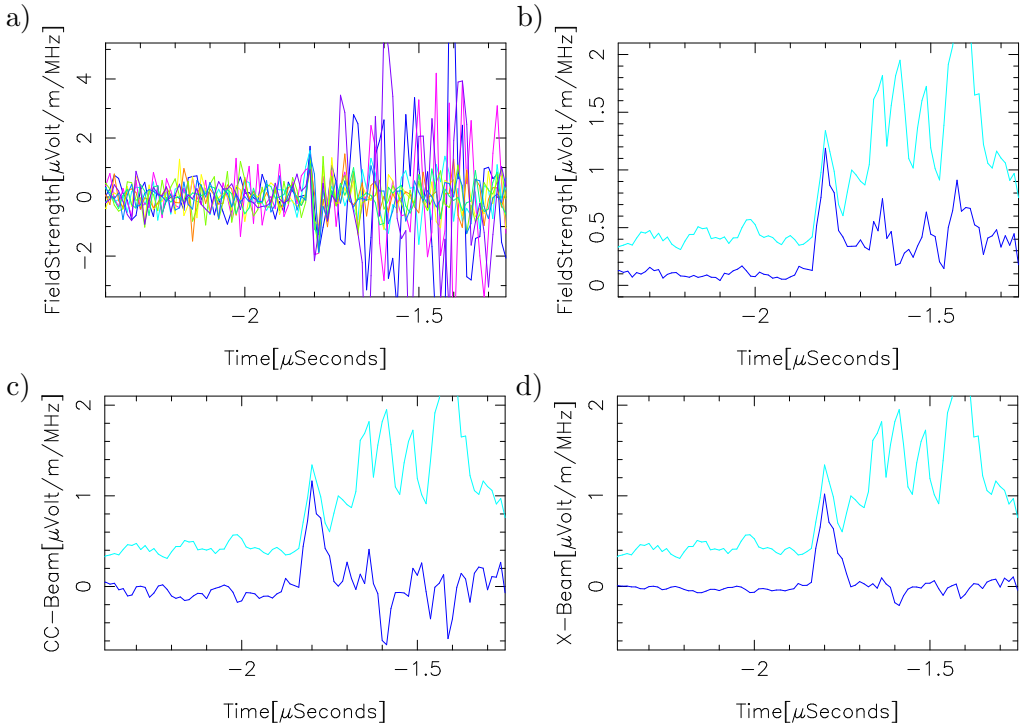

Figure 3.6: a) Section of the filtered data for all antennas. At $-1.8\,\mu$s a coherent pulse can be seen (all traces fall onto each other), between $-1.75\,\mu$s and $-1.3\,\mu$s there is incoherent noise in several antennas (noise from the particle detectors see section 4.3). b) Absolute values of the field strength after normal beam forming in dark blue. c) The cross-correlation beam. The coherent pulse stays the same, but some of the noise peaks have negative sign marking them as incoherent peaks. d) The so called X-Beam. The only remaining peak is the coherent peak from the air shower. For comparison the power-beam is plotted in light blue in panels b)-d), and all the beams are smoothed by block averaging over 3 samples.

Where $F[t]$ is the unnormalised field strength of the formed beam, $f[t]$ is the normalised field strength, N the number of antennas, $s_i[t]$ the time shifted field strength of the single antennas, and t the time or pixel index.

This is the normal beam forming process. With this the parts of a coherent pulse can have both positive and negative sign, so to see a peak one has to look at the absolute values.

- For comparison the squared values of all antennas are averaged and then the square root is taken, called the power-beam.

$$p[t] = \sqrt{\frac{1}{N}\sum_{i=1}^{N} s_i^2[t]} \tag{3.10}$$

This gives a peak if there is lots of power in the antennas, independent of it being coherent or incoherent.

- The data from each unique pair of antennas is multiplied, the resulting values are averaged, and then the square root is taken while preserving the sign.

$$cc[t] = \overset{+}{-}\sqrt{\left|\frac{1}{N_{Pairs}}\sum_{i=1}^{N-1}\sum_{j>i}^{N} s_i[t]s_j[t]\right|} \tag{3.11}$$

N_{Pairs} is the number of unique pairs of antennas, i.e. $N_{Pairs} = \frac{(N-1)N}{2}$. The negative sign is taken if the sum had a negative sign before taking the absolute values, and the positive sign otherwise.

We call this the cross-correlation beam or CC-beam. Seen as an interferometer the CC-beam is the real part of the visibility, averaged over all baselines but integrated over only one sample time. To understand it, one can also square the unnormalised part of equation 3.9 and then expand it:

$$\begin{aligned} F^2 &= \left(\sum_{i=1}^{N} s_i\right)^2 = \Big(s_1 + s_2 + \cdots + s_N\Big)\Big(s_1 + s_2 + \cdots + s_N\Big) \\ &= \underbrace{s_1^2 + s_2^2 + \cdots + s_N^2}_{\propto p^2} + \underbrace{2s_1s_2 + 2s_1s_3 + \cdots + 2s_{N-1}s_N}_{\propto cc^2} \end{aligned} \tag{3.12}$$

So the power of the normal beam consists of two parts, one is proportional to the squared power-beam and the other to the squared CC-beam. In other words, the CC-beam is the field strength minus the average total power (coherent or incoherent). As the power-beam is independent of the power being coherent or not, the coherence effects must be contained in the CC-beam. Thus the CC-beam is more sensitive to the difference between coherent and incoherent pulses. For the normalisation note that the sum is over N of the s_i^2 and $(N-1)N$ of the s_is_j (or $\frac{(N-1)N}{2}$ of the $2s_is_j$) summands, giving a total of N^2 summands. So normalising the field strength with $\frac{1}{N}$, the power-beam with $\sqrt{\frac{1}{N}}$ and the CC-beam with $\sqrt{\frac{1}{(N-1)N}}$ (or $\sqrt{\frac{2}{(N-1)N}}$ as we calculate only unique pairs) gives the same normalisation for all three beams. This is easily checked for the case of total coherence, where all the s_i have the same value. In this case all three beams also give the same absolute value. (The field strength may have a negative sign.)

The advantage of the CC-beam is that a peak from a coherent pulse always has a positive sign. Peaks from incoherent pulses can also have a negative sign, e.g., if one antenna has a large value but the other antennas have values with opposite sign. (Seen in terms of interferometry again: A coherent pulse would be a point source in the phase centre, so the visibility has a constant value over all baselines. Anything else will have different values for the different baselines and thus will give smaller or even negative values after averaging.)

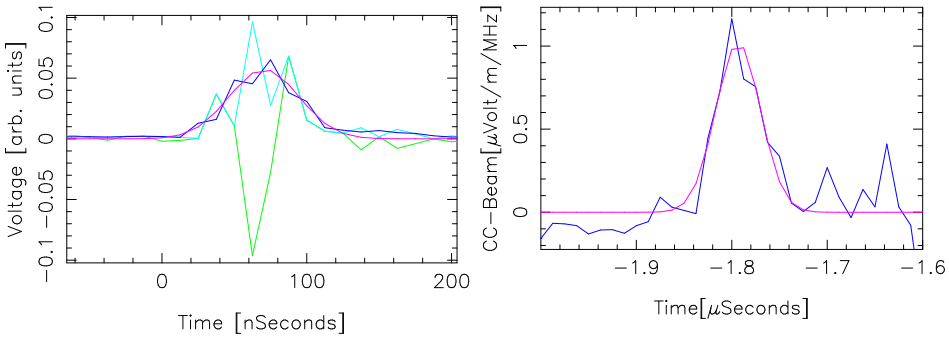

Figure 3.7: Left: Simulated impulse response of the anti-aliasing filter in green, absolute value in light blue, smoothed data in dark blue, and Gaussian fit to the smoothed data in pink. The unsmoothed data shows a lot of fine structure that is suppressed by the smoothing. Right: Smoothed CC-beam of an air shower pulse (dark blue) and a Gaussian fit to it (pink). The width of the fit to the simulated pulse is 56.9 ns, the width of the air shower pulse is 58.8 ns.

- To better bring out the significance of a pulse in the presence of rapidly changing noise, the CC-beam is weighted by the absolute value of the relation of the smoothed CC-beam to the smoothed power-beam.

$$x[t] = cc[t] \cdot \left| \frac{< cc[t] >}{< p[t] >} \right| = cc[t] \cdot \left| \frac{\mathrm{BA}\left(cc[t] - cc_0\right)}{\max\left(\mathrm{BA}\left(p[t] - p_0\right), p_{min}\right)} \right| \tag{3.13}$$

  Here BA() means block averaging over 3 samples, cc_0 is the zero offset of the CC-beam, p_0 is the zero offset of the power-beam, and p_{min} a small value to avoid dividing by zero. As there is noise but the noise is mostly incoherent, cc_0 normally has a small value but p_0 has a significant value.

  As coherent peaks have the same height in both beams they are not changed much, but incoherent peaks usually have a larger value in the power-beam than in the CC-beam, so they are reduced. This is called the excess-beam or X-beam.

Figure 3.6 shows the different kinds of beams. Panel a) shows the data from all antennas, while panels b)-d) show the field strength, the CC-beam, and the X-beam, all together with the power-beam. The peak from the coherent pulse at $-1.8\,\mu$s is seen in all panels with about the same height. The incoherent noise between $-1.75\,\mu$s and $-1.3\,\mu$s produces significant peaks in the field strength, smaller peaks in the CC-beam and no significant peaks in the X-beam.

3.3.8 Quantification of Peak Parameters

The response of the analogue electronics to a short pulse is an oscillation over a short time. The major contribution to this oscillation comes from the anti-aliasing

filter. Filtering of the lower frequencies causes an oscillation around zero, while the finite bandwidth broadens the pulse. Sampling such a signal with an ADC gives a certain fine structure inside the pulse that is not part of the original pulse but is caused by the electronics. The left side of figure 3.7 shows this fine structure. The green line shows the simulated[3] impulse response of the filter, and the light blue line its absolute value.

To suppress this fine structure the data is smoothed by block averaging over 3 samples. The result is shown in figure 3.7 in dark blue. Although the pulse shape is not really Gaussian (see right side of fig. 3.7), fitting a Gaussian to the smoothed data gives a robust value for the peak strength. Other methods, like ,e.g., the maximum of the peak or the sum over the pixels of the peak, can change their values when the data is shifted in time or suffer from problems in determining where the pulse starts and where it ends. As the width of a peak is determined by the electronics, the width of the fitted Gaussian does not vary much. So the height of the fit is a good measure of the peak strength. Figure 3.7 shows the Gaussian fits in pink. To remove the background noise in real data we first subtract the baseline from the data, i.e. the mean value outside the region of the pulse. As we have already accounted for the trigger delay in a previous step, the fit is done for a small region around $\sim -1.8\,\mu$s. The fit is first done for the X-beam to identify the dominant pulse. The results from this fit are then used as the start values for the fits to the field strength and the CC-beam.

3.3.9 Radius of Curvature

The radio pulse of an air shower does not arrive on the ground as a plane wave, but it has some curvature. For the distances of LOPES the shape of the wavefront can be represented by a sphere with a finite radius of curvature. This radius of curvature is optimised by calculating the peak height in the X-beam and iterating the radius of curvature until the peak is maximal. The left and middle panel in figure 3.8 show the difference between plane wave beam forming and beam forming with an optimised radius of curvature.

3.3.10 Event Identification

Not every selected air shower is accompanied by a radio pulse that is detectable by LOPES. If there is no pulse from the air shower there can be an incoherent noise peak that is as high as an average air shower peak, even in the X-beam. The right panel in figure 3.8 shows an event that has no air shower peak, but noise in two antennas that can produce a false peak. So one cannot select events with air shower

[3]The impulse response was calculated by measuring the frequency response of the filter including the phase, interpolating it on a grid that represents our sampling rate, and then Fourier transforming the data. This gives us the response of the filter to a delta peak at $t = 0$ s. (The fact that the peak is centred around $\sim +70$ ns shows us, that this is a real filter i.e. the output comes after the input. Using just the absolute values of the frequency response would give a pulse centred at 0 ns, i.e. part of the output coming before the input.)

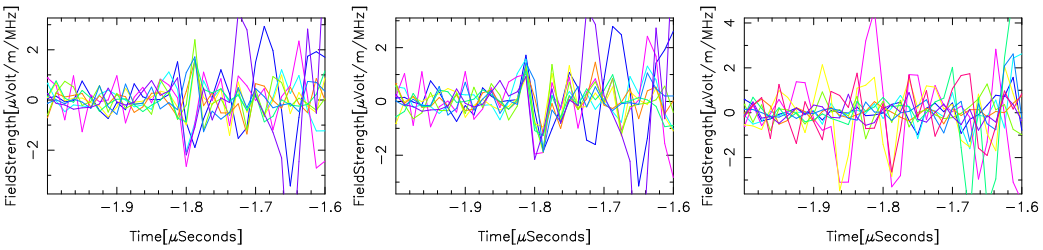

Figure 3.8: Left: Data of a good event but shifted for beam forming as a plane wave. The pulse at $-1.8\,\mu$s is not coherent. Middle: The same event, but with a radius of curvature of 2250 m. The coherent pulse is clearly visible. Right: A bad event. There is a peak at $-1.85\,\mu$s but this is due to a spike in only two antennas.

pulses just by the height of the fitted Gaussian, but has to classify events in an extra step. The criteria for this selection are: existence of a pulse, coherence of the pulse, position in time of the pulse, and approximately uniform pulse height in all antennas. Quantification of these parameters, so that the classification can be done automatically, is not easy. Simple methods using only a small number of parameters turned out to have a significant number of false classifications. The low absolute number of events makes it desirable to have the lowest number of false classifications that is possible. But it also allowed us to classify all selected events by eye, which turned out to be the most effective way for now.

Chapter 4

Radio Frequency Interference

Radio frequency interference (RFI) is every radio signal, that the receiving system picks up but is not the signal you are looking for. So in the case of LOPES the TV transmitter in our band, the emission of the KASCADE-Grande electronics, the FM band etc., are all considered RFI. On the other hand a TV viewer would consider atmospheric radio flashes, like those from air showers, as RFI. As LOPES is built in a populated area where its frequency band is commercially used and a lot of other electronics is present, it cannot avoid all RFI so it has to deal with RFI.

RFI can be roughly grouped into two kinds: (approximately) continuous, narrow band transmissions and short time, broad band pulses. Nearly all intentional transmissions are of the first kind, e.g TV and FM stations but also voice radio[1] etc. Unintentional transmissions can be of both kinds: The system clock leaking out of a computer is continuous and narrow band, while sparks in an electric motor cause short time pulses. As intentional transmissions tend to be stronger than unintentional, the biggest part of the total RFI power is in the form of narrow band transmissions. Narrow band RFI can be suppressed in frequency space, while short time pulses are suppressed in the beam forming process, see sections 3.3.5 and 3.3.7.

4.1 RFI Measurements before the Setup of LOPES

To assess whether the KASCADE-Grande site is usable for LOPES and to determine needed parameters for the design of the hardware, we had to conduct background measurements before setting up LOPES.

The first measurements at the KASCADE-Grande site were done by the RegTP, the *German Regulatory Authority for Telecommunications and Posts* on our behalf. This measurements were done in the centre of the KASCADE array and in two opposing corners of the array. The goals were to assess the frequency coverage at the site and determine whether and how much RFI is emitted by the KASCADE electronics.

[1] Even a short piece of a conversation over voice radio lasts long enough to be considered a continuous transmission for LOPES.

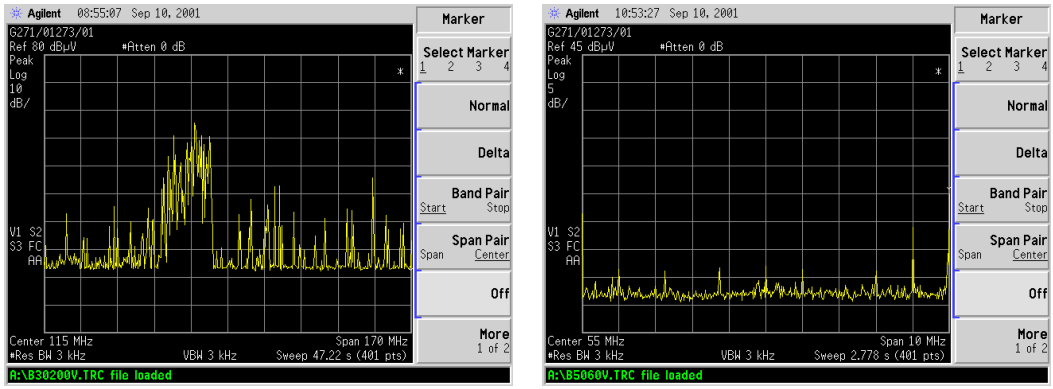

Figure 4.1: Results of the background measurements by the RegTP at the KASCADE-Grande site. The left panel shows the frequency coverage from 30 MHz to 200 MHz, the FM-band from 87 MHz to 108 MHz is clearly visible. The right panel shows the range from 50 MHz to 60 MHz, only a few lines are stronger than the system noise.

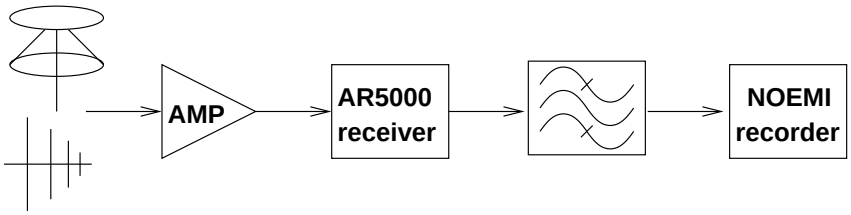

Figure 4.2: Sketch of the test setup with antenna (discone or logper), amplifier, AR5000 receiver, filters and NOEMI recorder.

Figure 4.1 shows the frequency coverage in the frequency range from 30 MHz to 200 MHz in the left panel. The FM-band between 87 MHz and 108 MHz is clearly visible. Outside the FM-band there is a number of transmitters present, but in between the transmitters there are regions that are dominated by the noise of the receiving system. Especially the range below the FM-band between 30 MHz and 80 MHz seems to be reasonably clean. The right panel of figure 4.1 shows the range from 50 MHz to 60 MHz, most of the band is dominated by the receiver noise with only a few lines sticking out. These measurements also showed that the KASCADE electronics do emit significant RFI. The most prominent part of this RFI are narrow band emissions at 40 MHz, 80 MHz and above the FM-band.

The measurements by the RegTP showed that while there is RFI present in all frequency bands, the range between 30 MHz and 80 MHz could be usable for cosmic ray measurements. To confirm this we conducted our own measurements at the KASCADE-Grande site. A sketch of the test setup is shown in figure 4.2. It

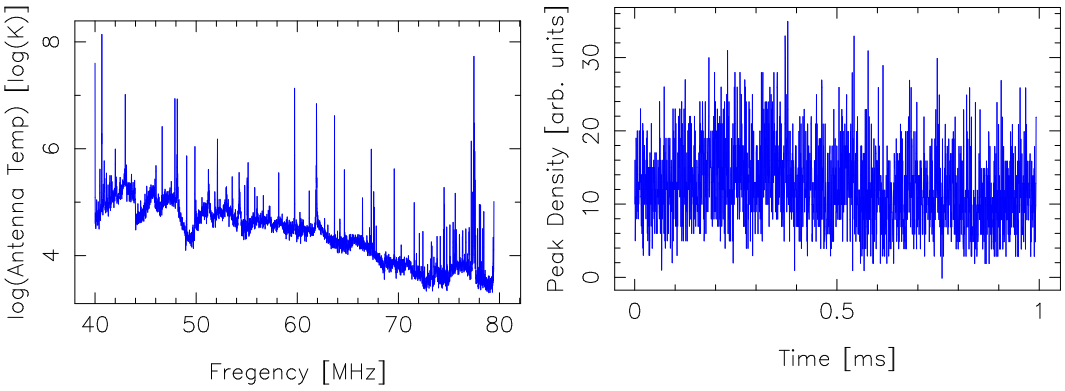

Figure 4.3: Left: Background noise spectrum at the KASCADE-Grande site, measured with the test setup and the discone antenna. It is composed out of 9 measurements centred around 40 MHz to 80 MHz in 5 MHz steps. The unevenness of the baseline at lower frequencies is caused by errors in the calibration of the AR5000 receiver which was done around 65 MHz. The rise of the system noise at lower frequencies is caused by the correction for the increasing mismatch between the antenna and the feed cable. Right: Density of 3σ-peaks in measurements with the test setup and the discone antenna triggered by the air shower trigger of the local KASCADE array cluster. The trigger time is in the middle of the data at 0.5 ms. There is no accumulation of peaks at this time, leading to the conclusion that the particle detectors produce no strong RFI.

consists of a discone or a log-periodic antenna connected to a combination of AR5000 receiver[2] and NOEMI recorder[3].

The results of these measurements can be summarised by figure 4.3. The left panel shows the combined spectrum for the whole frequency range of LOPES. It shows a number of narrow band lines of which many have been identified as being emitted from the electronics container. Most of the frequency range between the lines is quiet and dominated by the system noise. This data shows that a receiver with a dynamic range of at least 60 dB (i.e. a factor of 1000 in voltage) should be able to handle the combined noise while still being able to resolve the sky noise. The KASCADE electronics also emits pulsed RFI. To test whether there is pulsed RFI emitted by the KASCADE detectors we triggered the test setup with the internal air shower trigger of the local cluster of the KASCADE array. Using the local trigger ensured that the nearest particle detectors had seen at least a few particles at the time of the trigger. With this we took 130 datasets of 1 ms centred around the trigger. There are no obvious radio peaks visible at the time of the trigger. The result of a further analysis, measuring the density of 3σ-peaks relative to the

[2]This is a commercial receiver that is tunable from 10 kHz to 3 GHz and has a signal output at an intermediate frequency with 10 MHz bandwidth centred around 10.7 MHz.

[3]A data recorder with 12 bit ADCs running at 40 MSPS.

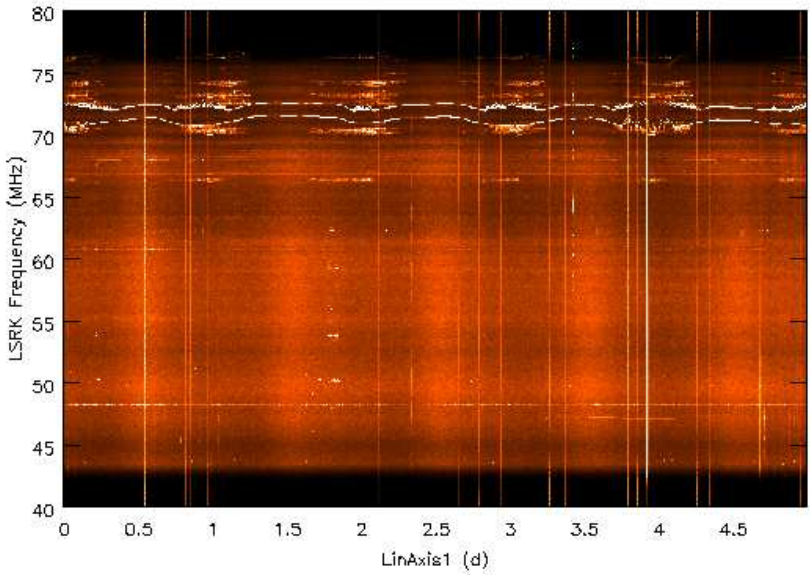

Figure 4.4: Dynamic spectrum taken with the LOPES system at Dwingeloo over several days during system tests. Corrupted data caused by a wrong setup of the optical data transmission causes bright vertical lines, but have been smoothed out to some extend. The daily rise and fall of the broadband background noise is due to the Galactic plane moving in and out of the antenna beam. The bright vertical line at 3.9 days is caused by a solar burst. Between 70 MHz and 75 MHz there are intermodulation products between the FM and the short wave band present. At 62 MHz and ca. 67 MHz are the video and the sound carriers of a TV station that is turned off at night.

trigger time is shown in the right panel of figure 4.3. Also there we did not see an accumulation of peaks at the time of the trigger. From this we conclud that the KASCADE particle detectors do not emit strong RFI when measuring normal air showers with a primary particle energy around 10^{15} eV.

4.2 RFI Measurements with the LOPES system

For test purposes the LOPES system was first set up at Dwingeloo. During this time we also took regular datasets over the Easter holidays. A dynamic spectrum of this data is shown in figure 4.4. Among other features this plot shows a daily rise and fall of the broadband background noise. This is caused by the Galactic plane moving in and out of the beam of the single antennas with the rotation of the earth. The fact that it is possible to see this effect tells us that the noise of the receiving system is at an acceptable level.

At the KASCADE-Grande site there is more RFI present than in Dwingeloo,

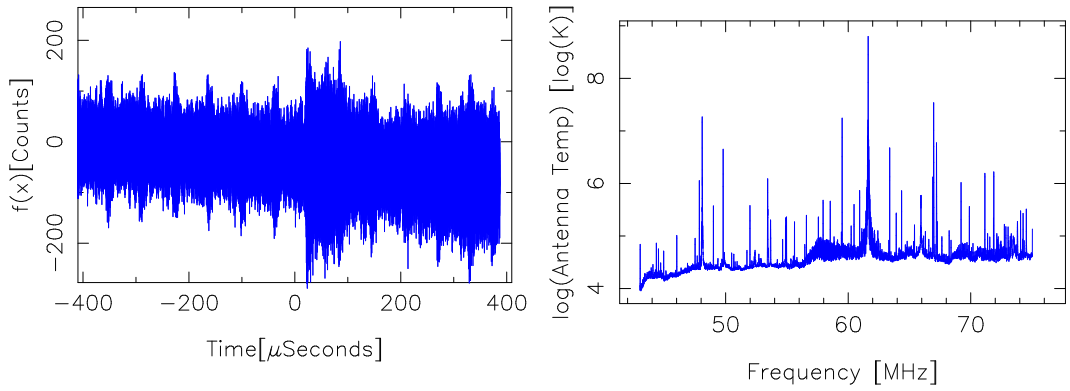

Figure 4.5: Left: Typical raw data of one antenna for a LOPES event. Right: Background spectrum of the KASCADE-Grande site measured with the LOPES system. The noise floor is higher than 10000 K which is larger than the average sky temperature of 2000 K (at 80 MHz) to 10000 K (at 40 MHz). The excess is mostly due to pulsed RFI.

so the rise and fall of the Galactic plane is mostly hidden in the noise (e.g. see figure 3.4). The left panel of figure 4.5 shows raw data of one antenna for a typical LOPES event. It covers the range of ca. ±200 ADC counts, less than the originally expected ±500 ADC counts. The pattern repeating every 66 μs is the horizontal blank of the TV transmitter, the rise in noise between $30 - 100\,\mu$s is RFI at 60 MHz from the KASCADE electronics while processing an event. The right panel shows a background spectrum taken with the LOPES system and averaged over 6.25 seconds. The TV transmitter at 62.2 MHz is stronger than in the measurements with the discone antenna. This is due to the fact that the discone antenna measures vertical polarised signals and thus is less sensitive to the horizontal polarised TV transmitter.

4.3 RFI from the Particle Detectors

After correlating the first LOPES events with KASCADE-Grande events we saw radio pulses in the LOPES data for the largest events with the following properties (see the left panel of figure 4.6):

- They arrive ca. 1.5 μs before the trigger.
- The pulses are less than a micro second wide.
- The pulse height rises with the air shower size and falls with distance to the shower centre.
- The relative arrival time of the pulses in the different antennas corresponds to the geometrical delay of a pulse from the direction of the air shower.

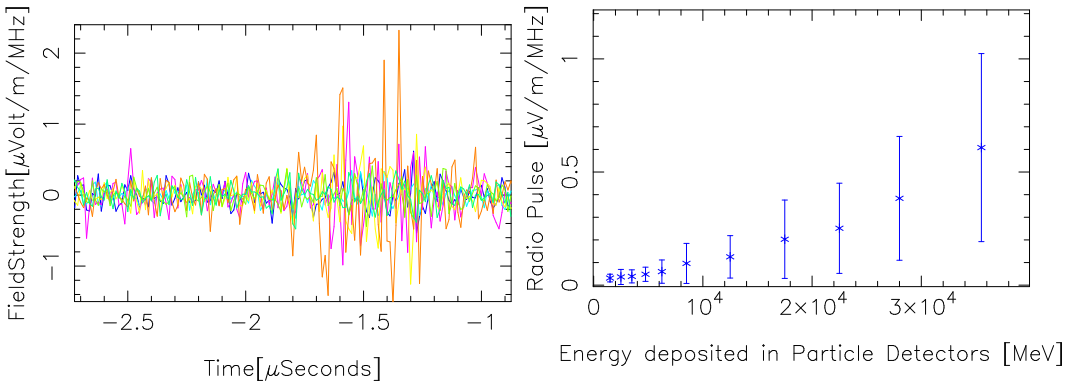

Figure 4.6: Left: Filtered and beamformed data for all antennas of a LOPES event. At $-1.8\,\mu$s a coherent pulse from the air shower can be seen. Between -1.7 and $-1.2\,\mu$s noise from the particle detectors is present. Right: Correlation of the height of the radio pulse emitted by the particle detectors to the sum of the energies deposited in the e/γ-detectors of the four nearest detector stations. (For the calculation of the field strength the gain of the LOPES antennas to the zenith was assumed, see section 2.4.4.)

These properties are roughly those that are expected from a radio pulse from the air shower. But in detail they are not really what we are expecting: They are still too wide, the height falls too fast with the distance to the shower centre, and while the beam forming moves the pulses closer together these are not coherent pulses. A measurement with the high voltage to the particle detectors in one cluster turned off showed that these pulses are gone when nearest particle detectors are not powered. Thus these pulses are not emitted by the air shower itself but are RFI from the particle detectors. Further examination showed that the height of the radio pulse is indeed well correlated to the sum of the energies deposited in the e/γ-detectors of the four detector stations nearest to a given antenna. The right panel of figure 4.6 shows this correlation for one of the LOPES antennas.

The reason these pulses were not detected during the test measurements is that they are only emitted when the particle detectors are hit by a particle density that only appears near the centre of large air showers. In the beginning we did not know that there is a time delay between the pulse from the air shower and the RFI from the particle detectors and the radio emission from the air showers itself is also strongest near the centre of large air showers. Thus it appeared possible that the air shower pulse would be completely masked by the RFI.

4.3.1 Shielding of Detector Stations

The first action to suppress the emission of the particle detectors was to cover complete detector stations of the KASCADE array with a wire mesh. The left panel of figure 4.7 shows one of the stations covered in a wire mesh. We covered a total of

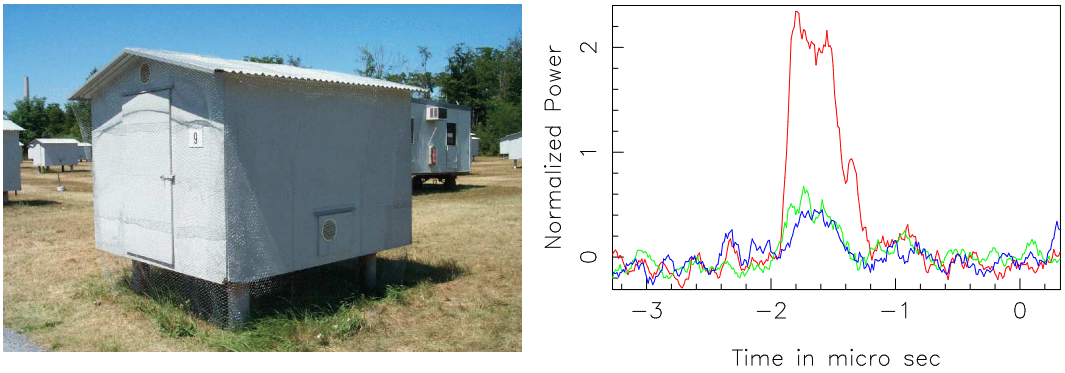

Figure 4.7: Left: One of the detector stations of the KASCADE array covered in wire mesh to shield the RFI emission of the detectors inside. Right: Pulse height of the radio pulse emitted by the particle detectors, normalised to the same background noise. Unshielded stations (red), stations covered in wire mesh (green) and stations where the wire mesh has been grounded (blue). While covering the stations in wire mesh reduces the RFI emission, grounding the mesh doesn't improve the effect.

eight detector stations, the four stations each that are closest to two antennas. This proved somewhat effective, reducing the emitted radio power by a factor of 5 to 6, as shown in the right panel of figure 4.7. The next step was to ground the wire mesh with an iron rod driven more than 50 cm into the ground. This did not improve the shielding effect much.

While shielding the detector stations reduces the power of the RFI pulse it does not change its other properties and these pulses are still the most prominent feature in our data. Also covering the detector stations in wire mesh interferes with the operation of the KASCADE array, as it prevents access to the detectors inside the stations.

4.3.2 Laboratory Measurements

Next we measured the radio emission of a spare e/γ-detector in a Faraday room at ASTRON in Dwingeloo. The setup is shown in the left panel of figure 4.8. The detector and the antenna were inside the Faraday cage and all the electronics outside. This ensures that the signal picked up by the antenna is emitted by the detector and not the electronics. These measurements confirmed that the e/γ-detector indeed emit radio pulses when triggered by a large signal.

The frame of an e/γ-detector detector consists of steel (see section 1.5.1). So it should be possible to seal the detector so that its frame acts as a Faraday cage, and no RFI is emitted by the detector. The holes in this Faraday cage are the connections of the three parts of the frame which are connected light tight but not tight against radio waves and the feed cables to the detector.

To seal the detector we put ferrite rings around the feed cables and we put copper

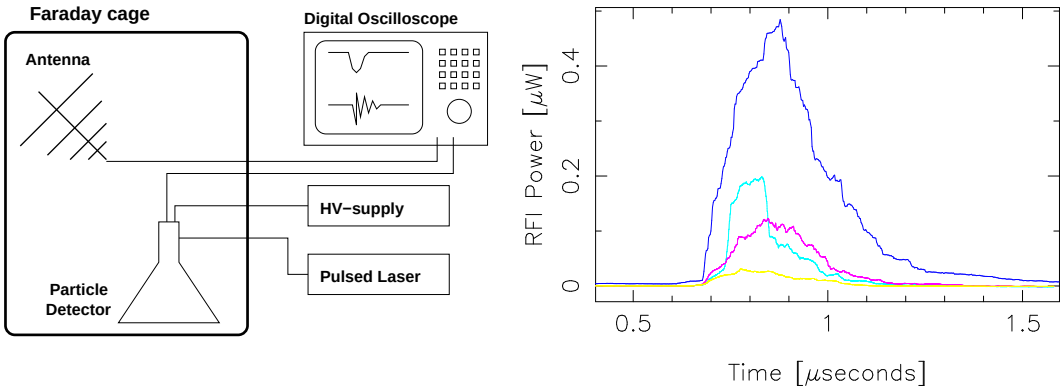

Figure 4.8: Left: Setup of the measurements of a single e/γ-detector in the Faraday room at ASTRON. The detector is triggered via a fibre optics cable by the laser, the oscilloscope is triggered by the signal output of the detector and records the signal from the antenna. Right: Strength of the radio emission by the detector. Unmodified detector (dark blue), with ferrite rings around the feed cables of the detector (light blue), with the shield of the feed cables taped to the detector frame (pink) and with both modifications (yellow).

tape around the connections of the frame and from the frame to the shield of the feed cables. The effect of this can be seen in the right panel of figure 4.8. Using both modifications the peak radio power is reduced by a factor of 15.

After it proved effective in the lab we put ferrite rings on the feed cables of the detectors around two antennas in the field. There we did not see a reduction of the RFI emitted by the particle detectors. The reason for this is not really understood. The two situations with detector and antenna in the close confines of the Faraday room on the one hand and both the detector and the antenna in the open on the other hand are different from each other. It may be possible that the transmission path from the detector to the antenna is different in both cases, making the ferrite rings effective in one situation and not effective in the other.

Fortunately we were able to show that the radio pulses from air showers and from the particle detectors are seperated in time. This made supressing the detector RFI a lower priority. A more detailed investigation of how to shield the particle detectors is currently being conducted.

Chapter 5

Cosmic Ray Event Analysis

5.1 Early Studies

The first unambiguous radio pulse from an air shower detected with LOPES was taken on the 12. January 2004. Figure 5.1 shows the field strength of the single antennas and the block averaged CC-Beam for this event. In this event the radio pulse from the air shower is stronger than the expected signal from the particle detectors (see section 4.3). It showed, that the contribution between $-1.7\,\mu$s and $-1.\,\mu$s matches the noise expected from the particle detectors and that at $-1.8\,\mu$s there is an additional, coherent signal that was then identified as the radio pulse from the air shower itself. This event was taken during a thunderstorm which increased its radio signal (see [Buitink05], [Buitink06]). This made this particular event unusable for a quantitative analysis, but it showed us how to distinguish air shower pulses from detector RFI.

An analysis based on this discovery was published in Nature [Falcke05]. It used a rather restrictive set of events with relatively high signal to noise. Using events from the first half year of operation, starting January 2004, all events were selected with a shower core within 70 m of the centre of LOPES, a zenith angle $< 45°$, and the muon number $N_\mu > 4 \times 10^5$, selecting 15 events in total. In all of those events we detected a radio pulse from the air shower, proving that indeed there are indeed radio pulses associated with air showers and that it is possible to measure them, even in radio loud environments, with a digital radio telescope. The analysis of the pulse heights of these events showed that there is a dependence of the pulse height on the angle of the air shower axis to the geomagnetic field and an independent, nearly linear dependence on the muon number.

5.2 Event Selection

The first phase of LOPES with 10 antennas was fully set up and calibrated in January 2004. In September 2004 measurements stopped for the upgrade to the second phase with 30 antennas. In the period from January to September 2004 LOPES collected

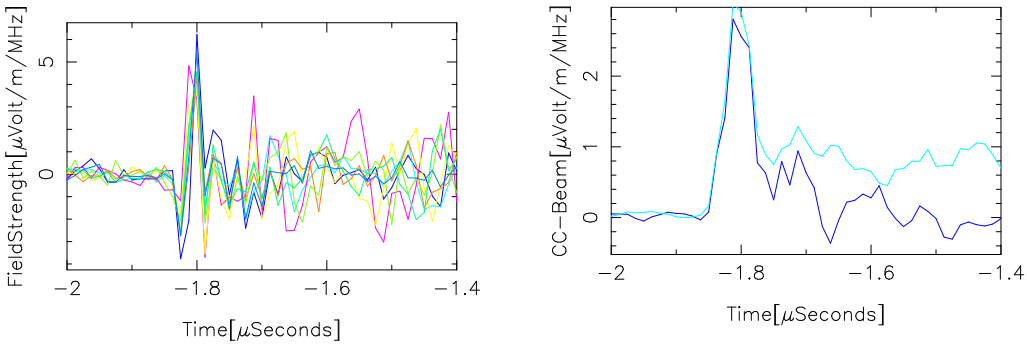

Figure 5.1: Left: Field strength of the single antennas of the first unambiguous radio pulse from an air shower detected with LOPES. Right: The formed beam of this event. One can clearly distinguish between the coherent radio pulse at $-1.8\,\mu$s and the detector RFI between $-1.7\,\mu$s and $-1.4\,\mu$s.

about 630 000 events. All events have been correlated with KASCADE events, and for 556 626 of those good data from the KASCADE array has been found.

As I am exclusively interested in the largest events that the KASCADE array measures, I have selected those events according to the following criteria:

A the KASCADE array processor did not fail

B the distance of the shower core to the array centre was less than 91 m

C the electron number was greater than 5×10^6 **or** the truncated muon number was greater than 2×10^5

The first two criteria are needed to ensure that the reconstructed data from the KASCADE array is reliable, the third criterion then picks the largest events. This selects 412 events.

These events were then processed with the complete pipeline as described in section 3.3, including the discrimination between events that have a radio peak from the air shower (called "good" events) and those that do not ("bad" events). This resulted in 228 out of the 412 events being considered good events. Three good events were flagged because they were taken during thunderstorms, one bad event was flagged because the delay calibration did not work properly.

Figure 5.2 shows the good and the bad events on a log(muon number) vs. $1 - \cos$(geomagnetic angle) plane[1]. The fraction of good to bad events rises both with rising muon number and with rising angle to the geomagnetic field. By defining stricter cuts on muon number and/or geomagnetic angle it is possible to get selections that contain only good events.

[1]Whenever in the course of this thesis the term "muon number" or N_μ is used it refers to the truncated muon number of KASCADE.

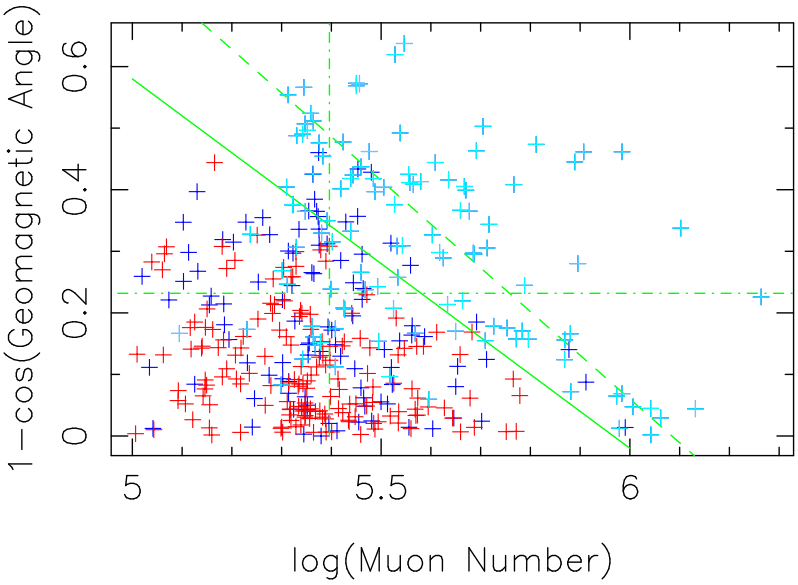

Figure 5.2: Good events in which a coherent pulse from the air shower was detected (blue), well detected events with a pulse larger than 4σ (light blue), and bad events that were selected but in which no pulse from the air shower was detected (red). The fraction of good to bad events rises with muon number and angle to the geomagnetic field. The solid green line separates the selected from the not selected events for selection 2, the two dash-dotted lines separate the selected events for selection 3, and the dashed line separates the selected events for selection 4.

To get reliable values for the radio pulse height two more cuts were introduced. To make sure that a value is based on sufficient data, events that had less than 6 antennas with good data are deselected. To avoid reconstruction problems of KASCADE and uncertainties of the antenna gain at high zenith angles, events with a zenith angle greater than 50° are deselected. To remove scatter from small, undetected events, a tail of undetected events with muon numbers less that 1×10^5 was deselected as well.

This left 375 selected events out of which 212 are detected. For the analysis I also made three selections with cuts on KASCADE data that had 100% detection efficency, i.e. that contain only good events. One with a cut to the geomagnetic angle that depends on the muon number (= events above and right of the solid green line in Figure 5.2), one with straight cuts to muon number and geomagnetic angle, and one in which again the cut to the geomagnetic angle depends on the muon number but with the values chosen so that only well detected events with a signal larger than 4σ are selected (= events above and right of the dashed green line in Figure 5.2). All cuts for the selections are summarised in Table 5.1.

Selection 1	Selection 2	Selection 3	Selection 4
KASCADE array processor did not fail			
R(shower core $\leftrightarrow$array centre) $< 91\,\mathrm{m}$			
$N_e > 5 \times 10^6$ **or** $N_\mu > 2 \times 10^5$			
$N_{\text{good antennas}} \geq 6$			
zenith angle $< 50^\circ$			
$\log(N_\mu) > 5$	$3.58 - 0.6\log(N_\mu)$	$\log(N_\mu) > 5.396$	$4.32 - 0.71\log(N_\mu)$
	$< 1 - \cos(\alpha_B)$	$\alpha_B > 39.8^\circ$	$< 1 - \cos(\alpha_B)$
375 selected 212 good	92 selected 92 good	62 selected 62 good	40 selected 40 good

Table 5.1: Summary of the selections used for the statistical analysis. The first selection contains all events, the others are different ways of selecting events with 100% detection efficency.

5.3 Discussion of Error Sources

The value used for the radio pulse heigh is the height of the Gaussian fitted to the CC-beam as described in section 3.3.8. This value is affected by a number of errors. One source of errors are errors of the KASCADE data we use, other sources are systematic and statistical errors inherent to the radio measurement.

5.3.1 Errors of the KASCADE Data

The air shower data we get from the KASCADE array is not only affected by shower fluctuations, but also by errors during the measurement and during the reconstruction of the air shower parameters. By simulating the detector response to simulated air showers and comparing the reconstructed parameters to the true parameters it is possible to assess the errors.

At the energies that are of interest for LOPES (i.e. at the highest energies of the KASCADE array) the reconstruction of the electron number has a systematical error of up to 45% (i.e. $\Delta\log(N_e) = 0.16$), and the truncated muon number of up to 60% (i.e. $\Delta\log(N_\mu) = 0.2$). This systematical error has been parameterised and thus can be accounted for [Ulrich05]. The statistical error of the reconstruction (i.e. ignoring shower fluctuations) is $\sim 5\%$ for the electron number and $\sim 10\%$ for the muon number [Antoni03].

The reconstruction of the air shower direction has no known systematical error. The statistical error is $\sim 0.1^\circ$ around the zenith, but rises with increasing zenith angle to $\sim 0.6^\circ$ at a zenith angle of 60° [Maier03].

The position of the shower core in the KASCADE array is reconstructed with an error of less than 1 m.

An estimated value for the primary particle energy can be calculated from the electron number, muon number and the zenith angle [Glasstetter05a], [Glasstetter05b].

In this the electron and muon numbers are first corrected for the attenuation in the atmosphere and then the logarithm of the energy is calculated as linear combination of the logarithms of the corrected electron and muon numbers. This estimated energy is not only affected by the errors of the input values, but also by the unknown mass of the primary particle, the air shower fluctuations, and the inadequacies of the function itself. Reasons for the latter include the limited number of simulated air showers (due to the available computing time) that forces one to extrapolate from showers simulated at low energies to higher energies, the dependence on the used model for the nuclear interactions, and the fact that it is only a linear approximation. Combined the error of the energy is estimated to be up to 50% (i.e. $\sigma(\log(E)) = 0.17$).

5.3.2 Systematic Errors

Systematic errors in the determination of the height of the radio pulse are caused by the calibration values as described in section 2.4 being incorrect. This can have several causes:

- The laboratory measurements of the electronic parts in the signal chain can be wrong. As these measurements are done in a controlled environment with standard laboratory equipment these errors are assumed to be small, i.e. less than 2%.

- The gain of the electronics in the signal paths of different antennas differs from the averaged value. The measured values of the receiver modules differ by $\sim 30\%$. As the beam forming process averages over all used antennas, the effect of this on the final pulse height can be up to $\sim 14\%$.

- The gain of the active balun is measured with an impedance converter instead of the real antenna. As both the signal transfer into the active balun and its gain depend on the impedance of the antenna, this value is not very reliable. It can be off by a factor of up to a few hundred percent.

- The gain of the antennas is only simulated. These simulations do not include the environment at the KASCADE-Grande site, e.g. the detector stations 9.2 meters away from the antennas, and they make assumptions about the conductivity of the ground, which can change with weather conditions. So the real gain of the antennas can differ from the simulations. These changes are more pronounced for large zenith angles, where reflections at the ground away from the pedestals and the surroundings play a larger role. Simulations of the antennas in different surroundings (with and without the pedestals) show that for zenith angles less than 50° the effect on the pulse height is less than 10%.

- The curvature of the radio front of an air shower is only approximated by a sphere. This affects the relative delays of the antennas and can degrade the

coherence of the pulse and thus reduce the measured pulse height. The effect of this is estimated to be less than 5%.

Errors of the determination of the electronic gain and the gain and impedance match of the active balun are the same for all events. So the large uncertainty of the gain of the active balun changes the absolute values of the measured pulse height, but does not change the relative pulse height of the different events.

5.3.3 Statistical Errors

The statistical errors of the measured pulse height include:

- As the calibration value for the antenna gain depends on the direction, the error of the direction from KASCADE translates into an error of the radio pulse height. For its calculation a constant error of 0.3° is assumed for the KASCADE direction. As the antenna gain drops faster with increasing zenith angle this error increases with zenith angle. For large zenith angles this can be larger than 10% of the pulse height but for the small zenith angles used in this analysis this error is negligible (smaller than 0.5%).

- The fit-routine returns a value for the error in the fitted height. This is the deviation of the fitted value from the true height of the assumed Gaussian. It does not include the uncertainty of the data that is being fitted in the first place. The average of this error is 13% of the pulse height, but it is usually smaller than the other errors.

- The air shower pulse is also affected by the background noise. Its strength is measured by calculating the spread of the beamformed data outside the time window of the air shower. The average of this error is 21% of the pulse height. For pulses with low signal to noise this is the dominating contribution.

- Slight errors in the relative delay of the antennas can degrade the coherence of the pulse and thus reduce the measured pulse height. The delay errors are due to errors of the delay calibration, errors in the determination of the radius of curvature, and the direction error from KASCADE. This effect is assumed to be 5% of the pulse strength. For strong pulses with high signal to noise this is usually the dominating contribution.

The values from all those sources are added in quadrature to give the resulting statistical error for an event.

5.3.4 Discrimination Errors

There are two kinds of discrimination errors. The first occurs in events that contain a strong radio pulse but are not detected. Events that contain only a weak radio pulse (i.e. with less than 3σ height) and are not detected are considered correctly discriminated as this is what I expect from not detected events. The second kind of

discrimination error contains events in which a noise spike was mistaken for a radio pulse. This also includes events with an air shower radio pulse that would normally be visible but in which a noise spike was fitted to get the pulse height.

Per definition only the first selection can be affected by errors of the first kind. This error would have the effect that the assumed pulse height of an event would be lower than the real pulse height. This is more than offset by the selection effect introduced by not adding the weak, undetected events to the analysis.

Errors of the second kind can affect all selections. They would also increase the assumed pulse height, which in turn adds to the selection effect in the statistical analysis. They are more probable if there is only a weak air shower pulse where random noise can be mistaken for a radio pulse. If there already is a strong pulse from an air shower then it is probably detected and distinguished from a nearby, even stronger noise pulse. So again in the stricter selections there are less errors of this kind. The fact that in unselected events usually no radio pulse that would be designated as an air shower pulse is found leads to the estimation[2] that the probability for this error even in the first selection is less than a few percent.

5.4 Event Statistics

5.4.1 Unmodified Pulse Height

Figure 5.3 shows the unmodified radio pulse height plotted against several air shower parameters. For the purpose of clarity, the statistical errors are not shown in the plots. As already explained in section 5.3.2 the absolute value of the pulse height has a large uncertainty so the units on the y-axes of the plots are arbitrary. As the relative height of the pulses is not affected by this it is still possible to determine the change of the pulse height with the different air shower parameters.

As expected from general considerations the pulse height rises with the shower size, i.e. with the electron and muon number. Similarly it declines with increasing distance to the shower axis. Of these the dependence on the muon number is the most pronounced.

The radio pulse height also rises with increasing angle to the geomagnetic field and with zenith angle. The average pulse height is also higher for showers from the north (azimuth angle around $0°, 360°$) than for showers from the south (azimuth angle around $180°$).

These dependencies are not independent. Electron and muon number are closely correlated, as well as the geomagnetic angle and zenith or azimuth angle. But also the average primary energy rises with zenith angle, because the air shower is more strongly attenuated and thus smaller air showers do not match the selection cuts. So for the interpretation of the results these dependencies need to be separated.

[2]For a systematic assessment of the probability of these errors one would have to generate a large set of noise data and grade it with our discrimination process. As the discrimination is done by hand this would take a lot of work and it is hard to do an unbiased evaluation when one already knows that one looks at noise data.

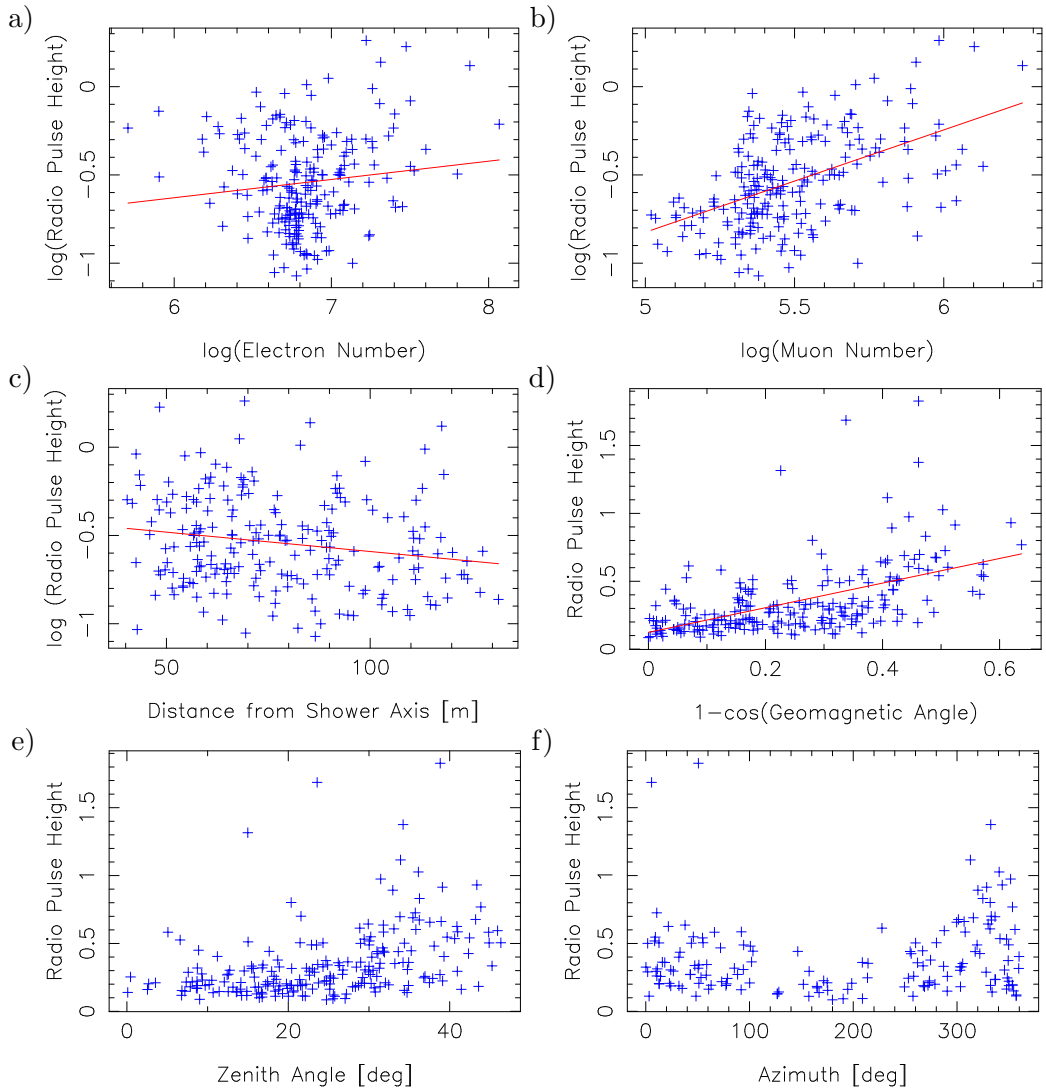

Figure 5.3: Unmodified radio pulse height plotted against a) the number of electrons, b) the muon number, c) the distance of the shower axis to the antennas, d) the angle to the geomagnetic field, e) the zenith angle and f) the azimuth angle. The red lines are linear fits to the plotted data, without implying any significance. To get a significant difference in direction in panel f) only events with a zenith angle $> 17°$ are plotted.

5.4.2 Separation of Parameters

The dependence of the radio pulse height can be separated into a dependence on the angle of incidence, an exponential dependence on the distance to the shower axis and a power law dependence on the shower size. To separate these parameters they are fitted separately in three iteration steps. In each fit the other dependencies are removed by dividing by the results of the fit from the previous iteration step. The fit functions are chosen so that they have one parameter that is a common factor for all events and can be used to account for an unknown systematic offset.

By trying different values for the shower size (electron number, muon number or primary particle energy, see section 5.4.5) and different functions for the angular dependence one can choose a combination that gives the best fit (see section 5.4.3).

So for the combination of muon number for the shower size and just the cosine of the geomagnetic angle for the angle of incidence, the procedure goes as follows:

1) In the first iteration the pulse height is divided by the muon number to account for the shower size.

   1.a) The first fit is a linear fit to the cosine of the geomagnetic angle:

   $$\epsilon_{\text{raw}} \frac{10^6}{N_\mu} = F_{\text{B1}}(\alpha) = s_{\text{B,1}}(1 + q_{\text{B,1}} - \cos\alpha) \tag{5.1}$$

   (With: ϵ_{raw} the radio pulse height, N_μ the muon number, α the geomagnetic angle, $F_{\text{B1}}()$ the fitted function, and $s_{\text{B,1}}, q_{\text{B,1}}$ the two fitted parameters.)

   1.b) The pulse height is then normalised with the results of the fit and a linear fit of the results to the logarithm of the distance to the shower axis is done, i.e. an exponential decrease with distance is assumed:

   $$\ln\left(\epsilon_{\text{raw}} \frac{10^6}{N_\mu} \frac{F_{\text{B1}}(90°)}{F_{\text{B1}}(\alpha)}\right) = F_{\text{D1}}(\text{R}_{\text{SA}}) = s_{\text{R,1}} - \frac{\text{R}_{\text{SA}}}{\text{R}_{\text{0,1}}} \tag{5.2}$$

   (With: R_{SA} the mean distance of the antennas to the shower axis, $F_{\text{D1}}()$ the fitted function, and $s_{\text{R,1}}, \text{R}_{\text{0,1}}$ the two fitted parameters.)

   1.c) Then the pulse height is normalised with the results of the two fits (but not with the muon number) and is fitted to a power law of the muon number:

   $$\epsilon_{\text{raw}} \frac{F_{\text{B1}}(90°)}{F_{\text{B1}}(\alpha)} \frac{\exp\left(F_{\text{D1}}(100\,\text{m})\right)}{\exp\left(F_{\text{D1}}(\text{R}_{\text{SA}})\right)} = F_{\text{M1}}(N_\mu) = s_{\mu,1} * (N_\mu)^{\text{p}_{\mu,1}} \tag{5.3}$$

   (With $F_{\text{M1}}()$ the fitted function and $s_{\mu,1}, p_{\mu,1}$ the two fitted parameters.)

2) In the second iteration the same fits are done, but instead of simply dividing by the muon number the results of the fit from the first iteration are used:

2.a)

$$\epsilon_{\mathrm{raw}} \frac{F_{\mathrm{M1}}(10^6)}{F_{\mathrm{M1}}(N_\mu)} \frac{\exp\left(F_{\mathrm{D1}}(100\,\mathrm{m})\right)}{\exp\left(F_{\mathrm{D1}}(\mathrm{R_{SA}})\right)} = F_{\mathrm{B2}}(\alpha) = s_{\mathrm{B},2}(1 + q_{\mathrm{B},2} - \cos\alpha) \quad (5.4)$$

2.b)

$$\ln\left(\epsilon_{\mathrm{raw}} \frac{F_{\mathrm{M1}}(10^6)}{F_{\mathrm{M1}}(N_\mu)} \frac{F_{\mathrm{B2}}(90^\circ)}{F_{\mathrm{B2}}(\alpha)}\right) = F_{\mathrm{D2}}(\mathrm{R_{SA}}) = s_{\mathrm{R},2} - \frac{\mathrm{R_{SA}}}{\mathrm{R}_{0,2}} \quad (5.5)$$

2.c)

$$\epsilon_{\mathrm{raw}} \frac{F_{\mathrm{B2}}(90^\circ)}{F_{\mathrm{B2}}(\alpha)} \frac{\exp\left(F_{\mathrm{D2}}(100\,\mathrm{m})\right)}{\exp\left(F_{\mathrm{D2}}(\mathrm{R_{SA}})\right)} = F_{\mathrm{M2}}(N_\mu) = s_{\mu,2} * (N_\mu)^{p_{\mu,2}} \quad (5.6)$$

3) The third iteration repeats the steps from the second iteration with the new fit results. The fit results from the second and the third iteration differ only slightly and less than their errors. The shows that this iterative procedure converges.

For other combinations the fitted functions have to be changed accordingly. So for the combination of primary particle energy and an angular dependence on the cosine of the geomagnetic angle and the cosine of the zenith angle the corresponding functions for the third iteration step are:

3.a)

$$\epsilon_{\mathrm{raw}} \frac{F_{\mathrm{E2}}(10^8\mathrm{GeV})}{F_{\mathrm{E2}}(\mathrm{E_p})} \frac{\exp\left(F_{\mathrm{D2}}(100\,\mathrm{m})\right)}{\exp\left(F_{\mathrm{D2}}(\mathrm{R_{SA}})\right)} = F_{\mathrm{B3}}(\alpha,\theta) = s_{\mathrm{B},3}(1 + q_{\mathrm{B},3} - \cos\alpha)\cos\theta \quad (5.7)$$

3.b)

$$\ln\left(\epsilon_{\mathrm{raw}} \frac{F_{\mathrm{E2}}(10^8\mathrm{GeV})}{F_{\mathrm{E2}}(\mathrm{E_p})} \frac{F_{\mathrm{B3}}(90^\circ, 0^\circ)}{F_{\mathrm{B3}}(\alpha,\theta)}\right) = F_{\mathrm{D3}}(\mathrm{R_{SA}}) = s_{\mathrm{R},3} - \frac{\mathrm{R_{SA}}}{\mathrm{R}_{0,3}} \quad (5.8)$$

3.c)

$$\epsilon_{\mathrm{raw}} \frac{F_{\mathrm{B3}}(90^\circ, 0^\circ)}{F_{\mathrm{B3}}(\alpha,\theta)} \frac{\exp\left(F_{\mathrm{D3}}(100\,\mathrm{m})\right)}{\exp\left(F_{\mathrm{D3}}(\mathrm{R_{SA}})\right)} = F_{\mathrm{E3}}(N_\mu) = s_{\mathrm{E},3} * \left(\frac{\mathrm{E_p}}{10^8\mathrm{GeV}}\right)^{p_{\mathrm{E},3}} \quad (5.9)$$

(With: $\mathrm{E_p}$ the primary particle energy, α the geomagnetic angle, θ the zenith angle, $\mathrm{R_{SA}}$ the mean distance of the antennas to the shower axis, the Fs the fitted functions and the ss, $q_{\mathrm{B},3}$, $\mathrm{R}_{0,3}$, and $p_{\mathrm{E},3}$ the fitted parameters.)

The values of the fitted parameters from the third iteration are shown in table 5.3. The form of the fitted functions in equations 5.1, 5.4, and 5.7 is chosen so that the q_{B} parameters can be interpreted as a value for the contribution of non geosynchrotron emission processes. If the air shower is exactly parallel to the geomagnetic field this is the field strength that remains. The additional factor $\cos\theta$ in equ. 5.7 is explained

	Selection 1	Selection 2	Selection 3	Selection 4
Muon Number				
$(1-\cos\alpha)$	2.05	2.68	1.82	2.55
$\sin\alpha$	2.98	3.31	1.92	3.85
$(1-\cos\alpha)\cos\theta$	2.35	3.15	2.25	3.1
$\sin\alpha\cos\theta$	3.78	5.14	4.48	5.6
Primary Particle Energy				
$(1-\cos\alpha)$	2.19	3.07	2.66	3.08
$\sin\alpha$	2.32	2.94	2.59	2.75
$(1-\cos\alpha)\cos\theta$	2.03	2.77	2.33	2.58
$\sin\alpha\cos\theta$	2.47	2.88	2.28	2.7

Table 5.2: The χ^2/ndf for the fits of the radio pulse height to functions of the geomagnetic angle (α) and the zenith angle (θ) for the four selections and for scaling with the muon number (top) or the primary particle energy (bottom. When scaling with the muon number the fit to $(1-\cos\alpha)$ is the best fit in all selections. When scaling with the primary particle energy the fit to $(1-\cos\alpha)\cos\theta$ is the best.

in section 5.4.3. The R_0 parameter is the typical size of the footprint of the air shower. The p_μ and p_E parameters are the indices of the power laws for the shower size dependencies. The values of the "s"-parameters denoting a common factor for all events are not given as their value depends on the normalisation of the pulse height.

5.4.3 Angular Dependence

Figure 5.4 shows the normalised pulse height in the third iteration step of section 5.4.2 after scaling with the muon number and the distance to the shower axis (i.e. the data used in step 3.a) plotted against the cosine and the sine of the geomagnetic angle. The pulse height shows a better correlation with the cosine than with the sine of the geomagnetic angle. This is also reflected by the fact that the linear fit to the data gives a better χ^2/ndf for the cosine than for the sine. The χ^2/ndf values for the fits to all four selections are shown in table 5.2. The fact that the fit to the cosine gives a slightly better χ^2/ndf value than the fit to the sine is also present in all other selections I have done, not only those presented here.

Figure 5.5 shows the pulse height after removing the dependence on the geomagnetic angle (i.e. data scaled with all three fits of the third iteration in section 5.4.2) plotted against the zenith and the azimuth angle. In these plots no significant dependence of the pulse height on those angles can be found.

The case for the zenith angle is different if the value that is used for the shower size is not the muon number but the "guesstimate" for the primary particle energy. As the calculation of the primary particle energy introduces a $1/\cos\theta$ factor, this factor is then visible in the angular dependence. Table 5.2 shows the χ^2/ndf value for

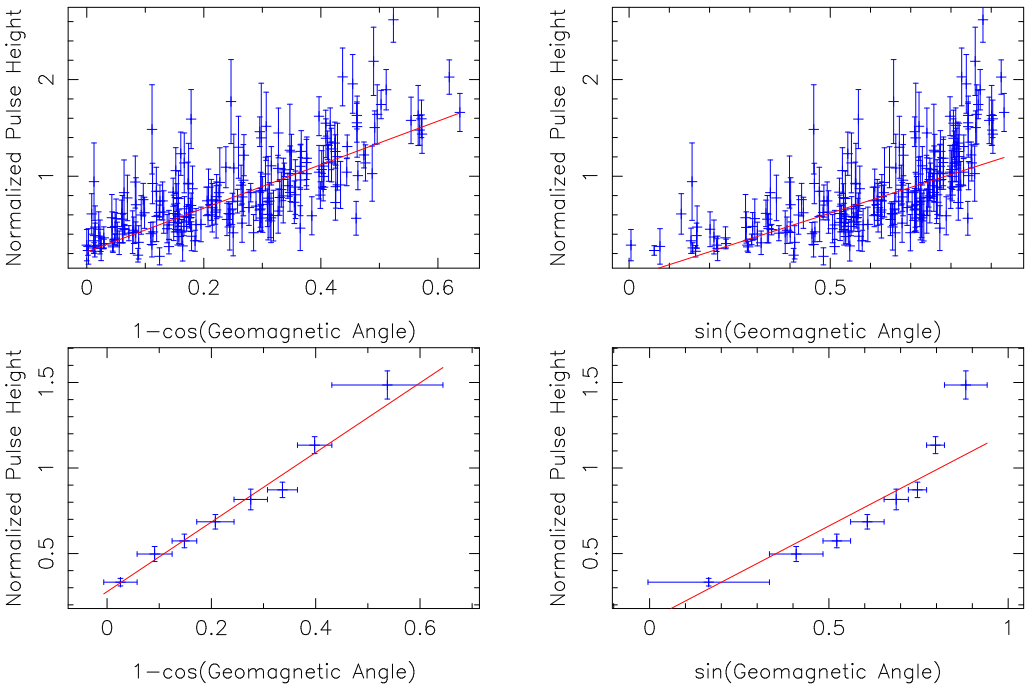

Figure 5.4: Radio pulse height normalised with muon number and distance to the shower axis plotted against the cosine (left) and sine (right) of the angle to the geomagnetic field. (top: single events; bottom: binned data, with equal number of events per bin. The error bars on the single events are the statistical errors from sec. 5.3.3) The fit to the cosine gives a slightly better χ^2/ndf value than the fit to the sine (see table 5.2).

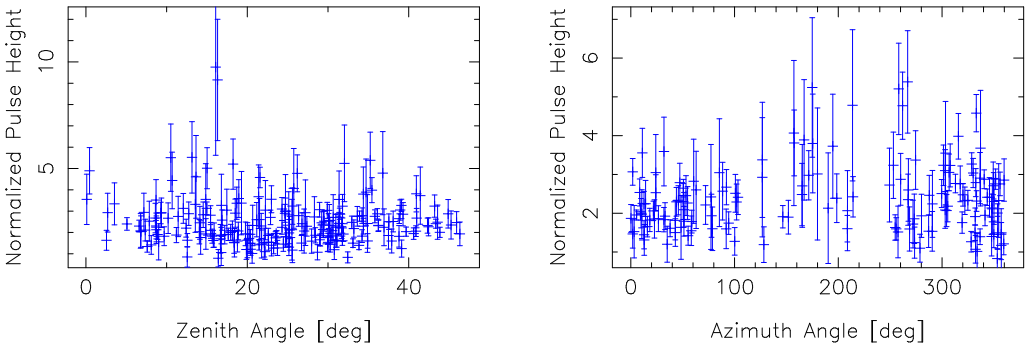

Figure 5.5: Normalised radio pulse height plotted against the zenith angle (left) and against the azimuth angle (right, zenith angle $> 17°$). (The error bars are the statistical errors from sec. 5.3.3.) After scaling with the muon number and taking out the effect of the geomagnetic angle the pulse height no longer depends on zenith or azimuth angle.

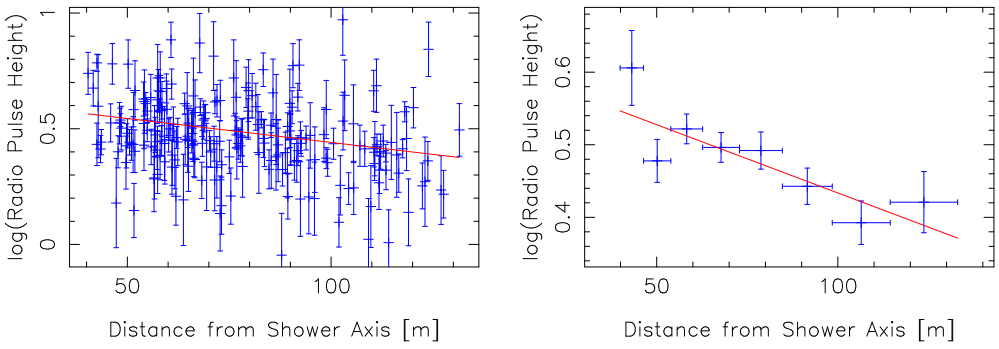

Figure 5.6: Normalised radio pulse height plotted against the distance to the shower axis. (left: single events; right: binned data. The error bars on the single events are the statistical errors from sec. 5.3.3)

fits of the radio pulse height to functions of the geomagnetic angle and the cosine of the zenith angle. The relation of these values is independent of the selection used: If the data is scaled with the muon number the fit to just the cosine of the geomagnetic angle gives the smallest χ^2/ndf, and if the data is scaled with the primary particle energy the fit to $(1 - \cos\alpha)\cos\theta$ is the best.

So our data suggests that the the radio pulse height depends on the cosine of the geomagnetic angle and has no further dependence on the azimuth angle. This is in contrast to the historical results that concluded that the radio pulse height depends on the sine of the geomagnetic angle, and to the theoretical predictions. There is also no indication from theory that the pulse height should depend on the cosine of the geomagnetic angle. Further studies, including polarisations measurements and a detailed comparison of simulations and measurements, are needed to resolve this.

5.4.4 Distance to the Shower Axis

Figure 5.6 shows the normalised radio pulse height (the data used in step 3.b in section 5.4.2) plotted against the distance of the antennas to the shower axis. It is in agreement with an exponential decrease of the pulse height with increasing distance. But the data has too much scatter for a detailed analysis of the shape. Also the distance range is small, so a steepening of the function at larger distances would not be visible. This will be possible when a similar analysis is done in correlation with data from the Grande array which includes larger distances and thus will be more significant.

5.4.5 Shower Size

Figure 5.7 shows the normalised radio pulse height (the data used in step 3.c in section 5.4.2) plotted against the electron number (a), muon number (b), and the estimated primary particle energy (c). It shows that the radio pulse height is better

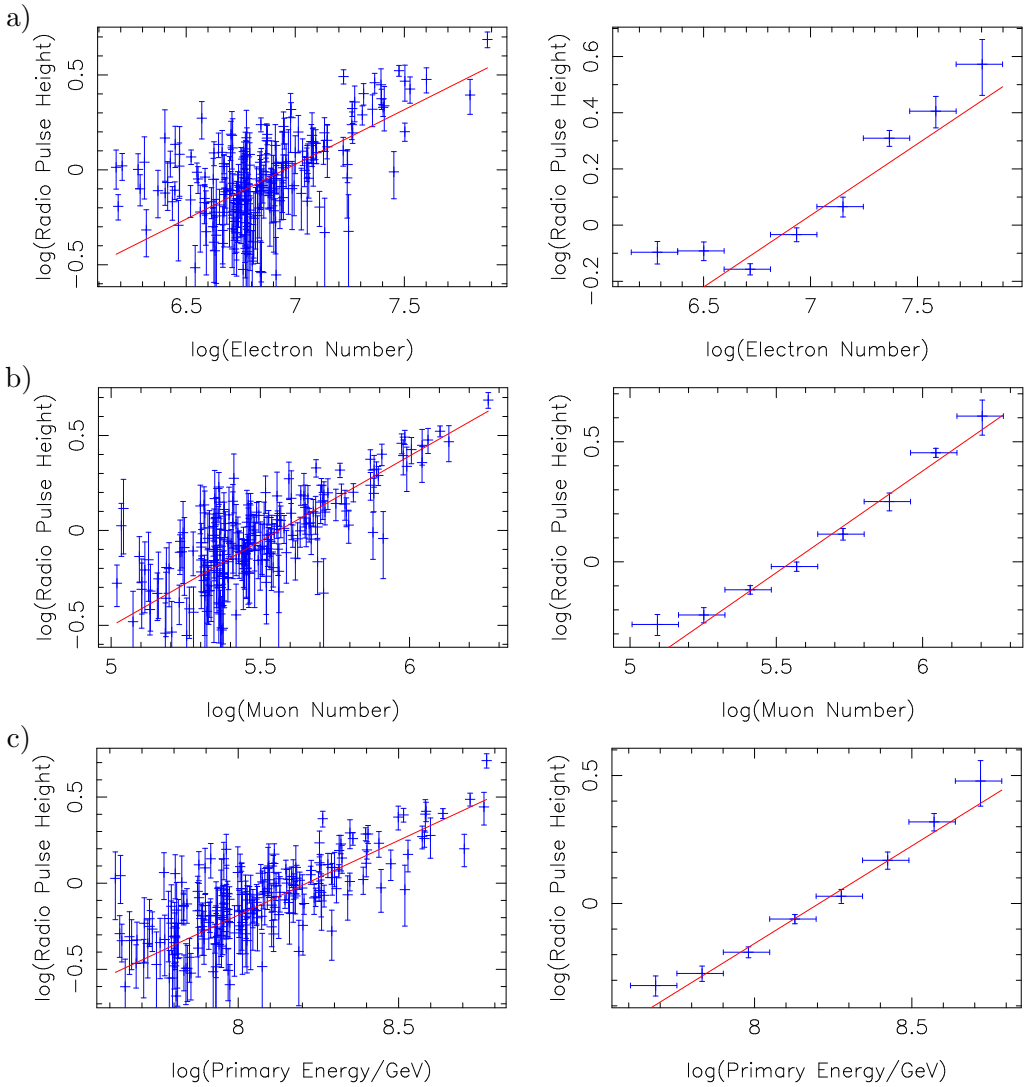

Figure 5.7: Normalised radio pulse height plotted against a) electron number, b) muon number, and c) primary particle energy. (left: single events; right: binned data. The error bars on the single events are the statistical errors from sec. 5.3.3)

correlated with the muon number than with the electron number. This is expected as for the observed primary energy range and at the atmospheric height of the KASCADE-Grande experiment the air shower is already dying out, giving a large dependence on the zenith angle. That makes the muon number a better tracer for the total number of particles during the shower evolution than the electron number at the detection level.

Combining electron and muon number to a value for the primary particle energy does not improve the correlation compared to the muon number alone, although it should be an even better tracer of the number of particles integrated over the shower evolution. A possible reason for this is that the calculated value for the primary particle energy has large systematic errors as it includes the extrapolation of parametrisations to large energies and large zenith angles. Another reason might be the error due to the unknown primary particle mass. These errors can then introduce more spread into the data, e.g. by weighting electron number and muon number wrong.

So for comparing the radio data with KASCADE-Grande data the muon number is the better value for the shower size. But for comparison to other experiments that do not measure the muon number (in the same way as KASCADE-Grande) the primary particle energy may be more useful.

5.4.6 Combined Fit and Parametrisation of the Field Strength

With the lessons learned from the separate analysis of the dependencies and using the results from the fits as starting points a combined fit of all dependencies is possible. The function for the combined fit based on the muon number is:

$$F_\mu\left(\alpha, \mathrm{R_{SA}}, \mathrm{N}_\mu\right) = s_\mu \left(1 + q_\mathrm{B} - \cos\alpha\right) \exp\left(\frac{-\mathrm{R_{SA}}}{\mathrm{R}_0}\right) \left(\frac{\mathrm{N}_\mu}{10^6}\right)^{p_\mu}. \tag{5.10}$$

The function for the combined fit based on the primary particle energy is:

$$F_\mathrm{E}\left(\alpha, \theta, \mathrm{R_{SA}}, \mathrm{E_p}\right) = s_\mathrm{E} \left(1 + q_\mathrm{B} - \cos\alpha\right) \cos\theta \exp\left(\frac{-\mathrm{R_{SA}}}{\mathrm{R}_0}\right) \left(\frac{\mathrm{E_p}}{10^{17}\,\mathrm{eV}}\right)^{p_\mathrm{E}}. \tag{5.11}$$

Fitting all parameters together has the advantage that the "s"-parameters get a meaningful value, they give the absolute scale of the pulse height. But one has to keep in mind that their value still depend on the normalisation of the other parameters, e.g. as a moun number of 10^6 does not equal a primary particle energy of 10^{17} eV one does expect different values for s_μ and s_E. The value is also affected by the large uncertainty of the electronic gain as described in section 5.3.2.

The results from the fits are shown in table 5.3 together with the results from the separate fits. The differences between results of the separate fits and of the combined fits is only small.

The difference of the parameters between the selections is rather small and generally inside the errors, but a few discrepancies remain. In selection 1 not all selected

	Selection 1	Selection 2	Selection 3	Selection 4
Separate Fits, Muon Number, $(1-\cos\alpha)$				
$q_{B,3}$	0.097±0.013	0.064±0.013	-0.032±0.033	0.065±0.021
$R_{0,3}$[m]	208±48	185±47	312±187	208±77
$p_{\mu,3}$	0.896±0.035	0.986±0.048	1.003±0.055	0.917±0.057
Separate Fits, Primary Particle Energy, $(1-\cos\alpha)\cos\theta$				
$q_{B,3}$	0.133±0.156	0.087±0.017	0.133±0.078	0.08±0.025
$R_{0,3}$[m]	217±46	192±52	256±114	217±86
$p_{E,3}$	0.861±0.033	0.967±0.051	0.95±0.059	0.929±0.068
Combined Fit, Muon Number, $(1-\cos\alpha)$				
q_B	0.097±0.013	0.064±0.015	-0.032±0.034	0.067±0.025
R_0[m]	198±43	200±60	260±110	236±105
p_μ	0.897±0.037	0.985±0.054	1.025±0.057	0.913±0.067
$s_\mu \left[\frac{\mu V}{m\,MHz}\right]$	3.7±0.33	4.3±0.49	5.2±0.73	4.04±0.57
Combined Fit, Primary Particle Energy, $(1-\cos\alpha)\cos\theta$				
q_B	0.137±0.016	0.096±0.018	0.161±0.089	0.098±0.03
R_0[m]	183±35	175±45	218±85	205±83
p_E	0.864±0.033	0.961±0.055	0.955±0.061	0.911±0.077
$s_E \left[\frac{\mu V}{m\,MHz}\right]$	1.18±0.09	1.23±0.12	1.01±0.2	1.23±0.15

Table 5.3: The values of the fitted parameters from the third iteration as described in section 5.4.2 (upper part) and the results of the combined fit (lower part). The given error is the statistical error of the fit.

events are also detected. So for low shower sizes and at low angles to the geomagnetic field it is biassed to high pulse heights. This leads to an higher value for q_B as the fitted events at small geomagnetic angles are on average too high. Overestimated pulse heights at low shower sizes also flatten the pulse height vs. shower size distribution, which leads to lower p_μ and p_E values. Selection 3 does not contain events at small geomagnetic angles. As the q_B value is especially sensitive to events at small geomagnetic angles this parameter is not well determined in this selection.

Selection 2 and selection 4 both contain events out of the whole range of geomagnetic angles and shower sizes. The difference between them is that selection 4 contains fewer events but events with a higher signal to noise. This leads to an higher statistical error but a lower systematic error.

To combine the values I averaged the value of q_B over the selections 2 and 4 and averaged the other parameters over the selections 2, 3, and 4. This results in the following formulas for the estimated, expected field strength per unit bandwidth:

$$\epsilon_{est} = (4.5 \pm 0.6) \left[\frac{\mu V}{m\,MHz}\right] f\,(1 + (0.07 \pm 0.02) - \cos\alpha)$$

$$\times \exp\left(\frac{-\mathrm{R_{SA}}}{(230 \pm 90)\,\mathrm{m}}\right)\left(\frac{\mathrm{N}_\mu}{10^6}\right)^{(0.97\pm0.06)} \tag{5.12}$$

(With: α the geomagnetic angle, $\mathrm{R_{SA}}$ the mean distance of the antennas to the shower axis, N_μ the truncated muon number, and f being a fudge factor to account for the systematic uncertainties.)

$$\begin{aligned}\epsilon_{\mathrm{est}} &= (1.2 \pm 0.2)\left[\frac{\mu\mathrm{V}}{\mathrm{m\,MHz}}\right] f\,(1 + (0.1 \pm 0.02) - \cos\alpha)\cos\theta \\ &\quad \times \exp\left(\frac{-\mathrm{R_{SA}}}{(200 \pm 70)\,\mathrm{m}}\right)\left(\frac{\mathrm{E_p}}{10^{17}\mathrm{eV}}\right)^{(0.94\pm0.06)}\end{aligned} \tag{5.13}$$

(With: α the geomagnetic angle, θ the zenith angle, $\mathrm{R_{SA}}$ the mean distance of the antennas to the shower axis, $\mathrm{E_p}$ the primary particle energy, and f being a fudge factor to account for the systematic uncertainties.)

The fudge factor f is set to $f = 1$ for the LOPES10 data with the current calibration. For a correct absolute calibration its value may change by a significant factor.

Whenever possible equation 5.12 should be used, e.g., when calculating the expected field strength from KASCADE-Grande data, as it is not affected by the problems of estimating the primary particle energy. When no KASCADE-style value for the truncated muon number is available, e.g. when comparing with data from other events, equation 5.13 can be used.

5.4.7 Discussion of the Results

Compared with the Monte Carlo simulation results and with historical data these results show some discrepancies. The most obvious is the dependence on the angle to the geomagnetic field. While here a $\epsilon_{\mathrm{est}} \propto 1 - \cos\alpha$ dependence is suggested, the historical papers report a $\epsilon_{\mathrm{est}} \propto \sin\alpha$ dependence, and the simulation results show no monotonic dependence on the geomagnetic angle but rather two systematically different dependencies on azimuth and zenith angle. The discrepancy between this results and the historical data is probably due to polarisation effects. LOPES currently measures only the east-west polarised emission and not the total signal strength. The fact that the experimental data shows a monotonic dependence on the geomagnetic angle while the simulation results do not has a greater significance. The theory predicts that total signal strength is largely independent of azimuth but the polarisation of the signal changes. Thus the east-west polarised component which is measured by LOPES is expected to be large for showers from the north or south and small for showers from east or west (see section 1.3.2). To explicitly test the azimuth dependence events from a zenith angle range that is $\pm 8^\circ$ around the inclination of the geomagnetic field were selected, i.e. $17^\circ < \theta < 33^\circ$. Figure 5.8 shows the radio pulse height of these events plotted against the azimuth angle. To avoid any contamination of the assumption of an geomagnetic angle dependence the pulse height was only divided by the muon number. Both the pulse height and

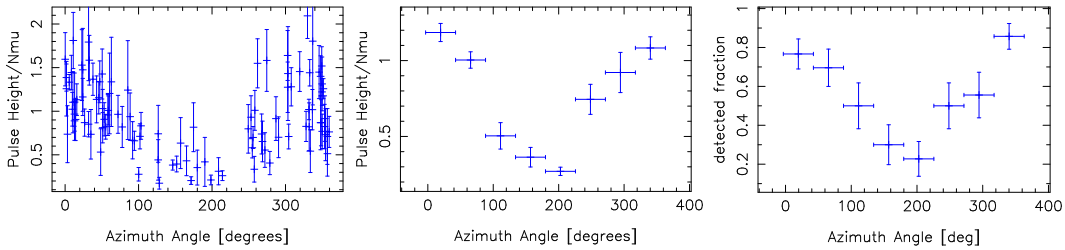

Figure 5.8: Radio data for events from zenith angle range ±8° around the inclination of the geomagnetic field of 25° (i.e. $17° < \theta < 33°$). Radio pulse height divided by the muon number plotted against the azimuth angle, left: single events; middle: binned data. Right: fraction of detected to selected events against azimuth angle.

the fraction of detected events show a clear north – south gradient, but no north-south – east-west gradient. Currently there is no satisfactory explanation why the experimental data differs from the theoretical prediction. This has to be studied further with simulations including a realistic shower model on the theoretical side and polarisation measurements on the experimental side.

Here also a rather large scale factor for the dependence on the distance to the shower axis is found. As this data spans only a rather small region close to the shower axis this result is not very significant.

The dependence of the measured field strength on the primary particle energy agrees well between my results, the historical data, and the simulation results. All three show that the field strength rises nearly linearly with the primary particle energy. This means that the emission is mostly coherent. That the exponent is slightly smaller than unity shows that in larger air showers a larger fraction of the primary energy is lost for the radio emission, e.g. because it is carried by particles into the ground.

Chapter 6

Summary and Outlook

Within the scope of this thesis we have set up the LOPES experiment – a digital radio telescope designed for the measurement of radio pulses from air showers, and located at the site of the KASCADE-Grande experiment –, developed the techniques to measure radio pulses from air showers, and analysed the first year of data taken with LOPES, thus achieving the first radio detection of air showers in modern times and verifying some long standing predictions.

The LOPES experiment consists of 30 dipole antennas (10 antennas in the first stage) that are read out with a digital receiver. This receiver digitises the 40–80 MHz band in the second Nyquist domain of an analogue to digital converter running at 80 MHz. It has functioned as a prototype station for LOFAR, expediting the development of the prototype electronics and testing them in a real production environment. To measure air showers LOPES uses an external trigger which it gets from the KASCADE array and writes 0.8 ms of raw ADC data onto hard disk for every event. For astronomical observations it can record up to 6.25 seconds of raw data onto hard disk. This allows us to do extensive processing of this data with modern computers.

To work with the data from LOPES we wrote the necessary, new software. With this software we can visualise and manipulate a dataset in time and frequency domain, or it can process a number of selected events in a batch mode. We also included the algorithms for delay and gain calibration of the data, filtering of narrow-band RFI, and beam forming. The reference values for the delay calibration can be obtained by cross correlating the antenna signals during a solar burst. The delay calibration for normal events is then done by comparing the phases from a TV transmitter signal. The gain calibration is done by measuring the electronics gain "in the lab", simulating the antenna gain, and then applying the frequency dependent gain curve to the frequency domain data.

At the site of KASCADE-Grande there is significant RFI present. This RFI comes in two kinds: narrow-band emission that is nearly continuous on LOPES timescales, and short time pulses. The narrow-band RFI can be suppressed by filtering in frequency space. This filter detects spikes in the frequency domain data

and suppresses the corresponding frequency bins. Short time pulses, that are not coming from the direction of the air shower are suppressed in the beam forming process. We form a so called cross-correlation beam. This is more sensitive to the difference between coherent emission from the direction of the formed beam on the one hand and emission from other directions or incoherent emission on the other hand. A special problem has been posed by radio pulses emitted by the particle detectors of the KASCADE array. In timing and relative pulse height they have many similarities to the radio pulses from air showers. Fortunately these pulses are not coherent and arrive in our antennas a little after the air shower pulses, so they can be distinguished from them.

LOPES and KASCADE events are currently recorded separately but they can be correlated offline. Thus LOPES can make use of a number of air shower parameters reconstructed from data from the KASCADE array. In my analysis the beam forming is done into the arrival direction of the air shower as given by KASCADE array. The interesting events for the analysis are selected mainly by the shower size (i.e. electron and muon numbers).

We have shown that with these techniques it is possible to detect radio pulses from air showers even in a radio loud environment [Falcke05]. The data from the first stage of LOPES has already been analysed and has yielded scientific results. In this thesis the dependence of the radio pulse height on air shower parameters is analysed. For this analysis the 412 largest events with good LOPES and KASCADE data were selected. Qualitatively the unmodified radio pulse height rises with increasing shower size, increasing angle to the geomagnetic field, decreasing distance of the antennas to the shower axis, increasing zenith angle, and a more northerly azimuth angle. The air shower parameters are not independent, e.g. the geomagnetic angle is calculated from the zenith and azimuth angle. A separation of the parameters showed that the radio pulse height can be well estimated by the distance to the shower axis, the geomagnetic angle, and either the muon number or the guessed primary particle energy and zenith angle. This has been quantitatively summarised in equations 5.12 and 5.13. Two results are especially noteworthy. The dependence on the primary energy is nearly linear, with a power law index of 0.94 ± 0.06. This means that the emission is largely coherent, which is what makes radio measurements of air showers possible. An unexpected result is that there is a monotonic dependence on the geomagnetic angle and that the data favours a $1 - \cos\alpha$ dependence. In the historical publications usually a $\sin\alpha$ was assumed, and the theoretical studies done within the scope of the LOPES project predict that there should be a zenith and azimuth angle dependence but no monotonic dependence on the geomagnetic angle.

To solve the issue of the angular dependence of the radio pulse strength we need precision measurements with high statistics and including polarisation on the experimental side and better simulations that include a more realistic air shower model on the theoretical side. With the now 30 antennas and stable operation LOPES will provide the statistics. Work on the absolute calibration of the radio antennas has already started, and it is planned to configure a few of the LOPES antennas for full polarisation measurement. The theoretical studies are also continuing [Huege05c].

For the design of large experiments to measure the highest energy cosmic rays it is important to know the radial dependence of the radio emission, at large distances and high primary energies. These values can be obtained from LOPES by analysing the data not only in conjunction with data from the KASCADE array but also together with data from the Grande array.

With the measurement of radio pulses is on the best way to become an established technique for cosmic ray measurements. The round the clock measurement capability and the fact that the radio pulse is integrated over the air shower evolution makes it complementary to the existing air shower measurement techniques. Its potential for precise direction measurements may be decisive for the establishment of cosmic ray astronomy. This makes it interesting to integrate radio measurements into the giant air shower experiments that are currently being built, e.g., the Pierre Auger Observatory. The combination of particle measurements on the ground with the bolometric nature of radio measurements would allow for composition measurements with high statistics. The ability to measure highly inclined air showers could be invaluable for the measurement of neutrino induced air showers. LOPES is a pioneering experiment for this technique and will go on and deliver precision measurements to calibrate the radio emission of air showers.

Appendix A

Glossary

ADC **A**nalog to **d**igital **c**onverter.

anti-aliasing filter A filter that selects signals out of only one Nyquist domain of an ADC.

balun **Bal**anced **un**balanced converter. A device that converts a symmetric signal (e.g. from a dipole or a twisted pair cable) to an asymmetric signal (e.g. on a coaxial cable) or vice versa.

beam forming Getting more sensitivity and greater directionality by adding the signals from different antennas. Sections 3.1.1 and 3.3.7 give an overview how beam forming is done for LOPES.

clean map An astronomical image in which the effects of the antenna pattern are removed. → *dirty map*

DAQ Abbreviation for **d**ata **aq**uisition.

dB $10 \times \log_{10}(\text{value})$ for power, $20 \times \log_{10}(\text{value})$ for voltage. E.g. 20 dB gain gives 100× the power and 10× the voltage.

dBm dB of the power in mW. E.g. $30\,\text{dBm} = 1000\,\text{mW} = 1\,\text{W}$.

dirty map A raw astronomical image, still including the effects of the antenna pattern. E.g. having false peaks due to sidelobes of the antenna. The effects of the antenna pattern can be removed e.g. by the clean algorithm [Högbom74] to get the so called clean map.

FT Short for Fourier transform. A short but useful introduction into the properties of the Fourier transform can be found in [Press92].

FFT Short for fast Fourier transform. An algorithm for the fast computation of the Fourier transform. The needed computation time is $\propto n^2$ for a naive implementation of the FT and $\propto n \log(n)$ for the FFT.

heterodyne receiver In a heterodyne receiver the signal is converted from the original frequency to another frequency by combining it with a reference frequency (from the local oscillator). Thus one can tune the receiver to different frequencies by changing the reference frequency and the following stages in the receiver can work at a conveniently fixed frequency. Complex receivers can have several stages of frequency conversion.

intermediate frequency Frequency of a signal inside a heterodyne receiver after frequency conversion.

jitter The short time variability of regular signal, e.g., a clock frequency, i.e. the spread of the time between two clock signals around the mean value.

leakage (during FTs) Transfer of power from one frequency to a range of frequency bins during Fourier transforms. E.g., if one has time domain data with only one sine wave in it, but with the frequency of the sine not a multiple of $\frac{\text{Nyquist freq.}}{\text{number of samples}}$, then the FT would transfer power from the sine not only to the bin next to its frequency but also to a range of frequency bins around that.

local oscillator Part of a heterodyne receiver, a receiver which at some stage converts a signal from one frequency range to another frequency range.

LOFAR **Lo**w **F**requency **Ar**ray,

LOPES **LO**FAR **P**rototyp**e** **S**tation

radiator In this paper: the part of an antenna, that actually transmits or receives the radio wave.

Nyquist domain An ADC has a Nyquist frequency of half its sampling clock (Nyquist theorem) [Press92]: $f_{\text{Ny}} = \frac{1}{2} f_{\text{ADC}}$. The first Nyquist domain goes from 0 Hz to f_{Ny} the second from f_{Ny} to $2\,f_{\text{Ny}}$ etc. It is impossible to determine from which Nyquist domain a signal comes just from the ADC data and without further knowledge. → *anti-aliasing filter*

OIP2 Output intercept point 2. The power at which the signal and the second order distortion products (e.g. at $f_{\text{out}} = 2\,f_{in}$) would have the same strength in the output of an active device, e.g., an amplifier, i.e. a measurement for the nonlinearities of such a device, a higher value means that the device has a better performance.

RegTP Short for *Regulatory Authority for Telecommunications and Posts*, the German government agency that among other things regulates and monitors frequency usage. Recently it has been renamed to *Federal Network Agency*.

RFI For **r**adio **f**requency **i**nterference. Any radio signal that is not what you are looking for. E.g., for LOPES the TV transmitter is RFI.

Bibliography

[Aglietta90] M. Aglietta, G. Badino, L. Bergamasco, C. Castagnoli, and A. Castellina. The EAS-TOP detector at Gran Sasso. *Nuovo Cimento C Geophysics Space Physics C*, 13:353–364, April 1990.

[AIPS++] AIPS++ Consortium. AIPS++ the Astronomical Information Processing System.

[Alkhofer75] O. C. Alkhofer. *Introduction to Cosmic Radiation.* Verlag Carl Thiemig, 1975.

[Allan71] H. R. Allan. *Prog. in Element. part. and Cos. Ray Phys.*, Vol. 10:171, 1971.

[Antoni03] T. Antoni, W. D. Apel, F. Badea, K. Bekk, A. Bercuci, H. Blümer, H. Bozdog, I. M. Brancus, C. Büttner, A. Chilingarian, K. Daumiller, P. Doll, J. Engler, F. Feßler, H. J. Gils, R. Glasstetter, R. Haeusler, A. Haungs, D. Heck, J. R. Hörandel, A. Iwan, K.-H. Kampert, H. O. Klages, G. Maier, H. J. Mathes, H. J. Mayer, J. Milke, M. Müller, R. Obenland, J. Oehlschläger, S. Ostapchenko, M. Petcu, H. Rebel, M. Risse, M. Roth, G. Schatz, H. Schieler, J. Scholz, T. Thouw, H. Ulrich, A. Vardanyan, J. Weber, A. Weindl, J. Wentz, J. Wochele, J. Zabierowski, and S. Zagromski. The cosmic-ray experiment KASCADE. *Nuclear Instruments and Methods in Physics Research A*, 513:490–510, November 2003.

[Antoni05] T. Antoni, W. D. Apel, A. F. Badea, K. Bekk, A. Bercuci, J. Blümer, H. Bozdog, I. M. Brancus, A. Chilingarian, K. Daumiller, P. Doll, R. Engel, J. Engler, F. Feßler, H. J. Gils, R. Glasstetter, A. Haungs, D. Heck, J. R. Hörandel, K.-H. Kampert, H. O. Klages, G. Maier, H. J. Mathes, H. J. Mayer, J. Milke, M. Müller, R. Obenland, J. Oehlschläger, S. Ostapchenko, M. Petcu, H. Rebel, A. Risse, M. Risse, M. Roth, G. Schatz, H. Schieler, J. Scholz, T. Thouw, H. Ulrich, J. van Buren, A. Vardanyan, A. Weindl, J. Wochele, and J. Zabierowski. KASCADE measurements of energy spectra for elemental groups of cosmic rays: Results and open problems. *Astroparticle Physics*, 24:1–2, September 2005.

[Ardouin05a] D. Ardouin, A. Belletoile, D. Charrier, R. Dallier, L. Denis, P. Eschstruth, T. Gousset, F. Haddad, J. Lamblin, P. Lautridou, A. Lecacheux,

D. Monnier-Ragaigne, and O. Ravel. Radio Detection of Extensive Air Showers with CODALEMA. Proc. ICRC 2005, 2005.

[Ardouin05b] D. Ardouin, A. Bellétoile, D. Charrier, R. Dallier, L. Denis, P. Eschstruth, T. Gousset, F. Haddad, P. Lautridou, A. Lecacheux, D. Monnier-Ragaigne, and O. Ravel. Features of radio-detected Extensive Air Shower with CODALEMA. In *SF2A-2005: Semaine de l'Astrophysique Francaise*, page 495, December 2005.

[Arts05] M. Arts. EM simulations of a LOFAR LBH antenna. *ASTRON-Report*, 2005.

[Askaryan62] G. A. Askaryan. *Soviet Phys. JETP*, 14:441, 1962.

[Askaryan65] G. A. Askaryan. *Soviet Phys. JETP*, 21:658, 1965.

[Atrashkevich78] V. B. Atrashkevich, O. V. Vedeneev, and H. R. Allan et al. *Soviet Phys. JETP*, 28:366, 1978.

[Badea05] A. F. Badea et al. First determination of the reconstruction resolution of an EAS radio detector. Proc. ICRC 2005, 2005.

[BährenLT] L. Bähren, H. Falcke, A. Horneffer, S. Lafebre, and A. Nigl. The LOPES-tools Software Package Manual.

[Baltrusaitis88] R. M. Baltrusaitis, G. L. Cassiday, R. Cooper, B. R. Dawson, J. W. Elbert, B. E. Fick, D. F. Liebing, E. C. Loh, P. Sokolsky, and D. Steck. The Fly's Eye detector: Present and future. *Nuclear Instruments and Methods in Physics Research A*, 264:87–92, February 1988.

[Bonifazi05] C. Bonifazi et al. Angular resolution of the Pierre Auger Observatory. Proc. ICRC 2005, 2005.

[Borione94] A. Borione, C. E. Covault, J. W. Cronin, B. E. Fick, K. G. Gibbs, H. A. Krimm, N. C. Mascarenhas, T. A. McKay, D. Müller, B. J. Newport, R. A. Ong, L. J. Rosenberg, H. Sanders, M. Catanese, D. Ciampa, K. D. Green, J. Kolodziejczak, J. Matthews, D. Nitz, D. Sinclair, and J. C. van der Velde. A large air shower array to search for astrophysical sources emitting γ-rays with energies $= 10^{14}$ eV. *Nuclear Instruments and Methods in Physics Research A*, 346:329–352, July 1994.

[Bruyn02] A. G. de Bruyn, R. P. Fender, J.M.E. Kuijpers, G. K. Miley, R. Ramachandran, H.J.A. Röttgering, B.W. Stappers, and M.P. van de Weygaert, M.A.M. and. van Haarlem. Exploring the Universe with the Low Frequency Array. 2002.

[Budnev05] Budnev et al., N. M. The tunka experiment: Towards a 1-km**2 cherenkov eas array in the tunka valley. 2005.

[Buitink05] S. Buitink et al. Electric field influence on the radio emission of air showers. Proc. ICRC 2005, 2005.

[Buitink06] S. Buitink et al. Amplified radio emission of air showers in thunderstorms. *A&A*, in prep.

[Calabretta02] M. R. Calabretta and E. W. Greisen. Representations of celestial coordinates in FITS. *A&A*, 395:1077–1122, December 2002.

[Chiavassa03] A. Chiavassa and KASCADE-Grande Collaboration. KASCADE-Grande: The Grande Array. In *International Cosmic Ray Conference*, page 989, July 2003.

[Chiba92] N. Chiba et al. Akeno Giant Air Shower Array (AGASA) covering 100 km^2 area. *Nuclear Instruments and Methods in Physics Research A*, 311:338–349, 1992.

[Falcke03] H. Falcke and P. W. Gorham. Detecting Radio Emission from Cosmic Ray Air Showers and Neutrinos with a Digital Radio Telescope. *Astropart. Physics*, 19:477, 2003.

[Falcke05] H. Falcke et al. Detection and imaging of atmospheric radio flashes from cosmic ray air showers. *Nature*, 435:313–316, May 2005.

[Fermi49] E. Fermi. *Phys. Rev.*, 75:1169, 1949.

[Geich-Gimbel89] C. Geich-Gimbel. *Int. J Mod. Phys.*, A4:1527, 1989.

[Glasstetter01] R. Glasstetter, 2001. private communication.

[Glasstetter05a] R. Glasstetter, 2005. Cosmic Ray Energy And Mass Estimator (V1.0).

[Glasstetter05b] R. Glasstetter et al. Shower Size reconstruction at KASCADE-Grande. Proc. ICRC 2005, 2005.

[Green03] K. Green, J. L. Rosner, D. A. Suprun, and J. F. Wilkerson. A Prototype System for Detecting the Radio-Frequency Pulse Assisoated with Cosmic Ray Air Showers. *Nucl. Instr. Meth.*, 498:256, 2003.

[Greisen56] K. Greisen. *Prog. Cosmic Ray Physics 3*, 1, 1956.

[Greisen66] K. Greisen. *Phys. Rev. Lett.*, page 748, 1966.

[Hakenjos05] A. Hakenjos. Kalibration eines Astronomischen Radioantennenfeldes durch eine externe Quelle, 2005.

[Haungs03a] A. Haungs et al. The KASCADE-Grande Experiment. Proc. ICRC 2003, 2003.

[Haungs03b] A. Haungs, H. Rebel, and M. Roth. Energy spectrum and mass composition of high-energy cosmic rays. *Reports of Progress in Physics*, 66:1145–1206, July 2003.

[Haungs04] A. Haungs et al. KASCADE: Astrophysical results and tests of hadronic interaction models. In *Proc. of the XIII ISVHECRI*, Nucl. Phys. B (Proc. Suppl.), 2004.

[Hayashida99] N. Hayashida, M. Nagano, D. Nishikawa, H. Ohoka, N. Sakaki, M. Sasaki, M. Takeda, M. Teshima, R. Torii, T. Yamamoto, S. Yoshida, K. Honda, N. Kawasumi, I. Tsushima, N. Inoue, E. Kusano, K. Shinozaki, N. Souma, K. Kadota, F. Kakimoto, K. Kamata, S. Kawaguchi, Y. Kawasaki, H. Kitamura, Y. Matsubara, K. Murakami, Y. Uchihori, and H. Yoshii. The anisotropy of cosmic ray arrival directions around 10^{18} eV. *Astroparticle Physics*, 10:303–311, May 1999.

[Hess12] V. Hess. *Physikalische Zeitschrift*, 13:1084, 1912.

[Hinton04] J. A. Hinton. The status of the HESS project. *New Astronomy Review*, 48:331–337, April 2004.

[Högbom74] J. A. Högbom. Aperture Synthesis with a Non-Regular Distribution of Interferometer Baselines. *Astron. Astrophys. Suppl.*, 15:417, June 1974.

[Huege03] T. Huege and H. Falcke. Radio emission from cosmic ray air showers. Coherent geosynchrotron radiation. *A&A*, 412:19–34, December 2003.

[Huege04] T. Huege. *Radio Emission from Cosmic Ray Air Showers*. PhD thesis, Universität Bonn, 2004.

[Huege05a] T. Huege and H. Falcke. Radio emission from cosmic ray air showers. Monte Carlo simulations. *A&A*, 430:779–798, February 2005.

[Huege05b] T. Huege and H. Falcke. Radio emission from cosmic ray air showers: Simulation results and parametrization. *Astroparticle Physics*, 24:116–136, September 2005.

[Huege05c] T. Huege et al. Fluctuations in the EAS radio signal derived with improved Monte Carlo simulations based on CORSIKA. Proc. ICRC 2005, 2005.

[Jelley65] J. V. Jelley, J. H. Fruin, N. A. Porter, T. C. Weekes, F. G. Smith, and R. A. Porter. *Nature*, 205:327, 1965.

[Kahn66] F. D. Kahn and I. Lerche. Radiation from Cosmic Ray Air Showers. *Royal Society of London Proceedings Series A*, 289:206–213, January 1966.

[Kamata58] K. Kamata and Nishimura J. *Prog. Theor. Phys. (Kyoto) Suppl. 6*, 93, 1958.

[Kampert04] K. H. Kampert et al. The Pierre Auger Observatory -Status and Prospects-. Proc. XIII ISVHECRI, Pylos (Greece), 2004.

[Karle95] A. Karle, M. Merck, R. Plaga, F. Arqueros, V. Haustein, G. Heinzelmann, I. Holl, V. Fonseca, E. Lorenz, S. Martinez, V. Matheis, H. Meyer, R. Mirzoyan, J. Prahl, D. Renker, M. Rozanska, and M. Samorski. Design and performance of the angle integrating Cerenkov array AIROBICC. *Astroparticle Physics*, 3:321–347, August 1995.

[Kopmann05] A. Kopmann, 2005. "RADAC Trigger Module", private communication.

[Maier03] G. Maier. *Suche nach Anisotropie in der kosmischen Strahlung mit dem KASCADE Experiment.* PhD thesis, Universität Karlsruhe, 2003.

[Matthews01] J. N. Matthews et al. Description of the High Resolution Fly's Eye Detector. Proc. ICRC 2001, 2001.

[NiglDS] A. Nigl. LOPES Daily Dynamic Spectra
URL `http://www.astro.kun.nl/~anigl/dslopes.html`.

[Petrovic05] J. Petrovic et al. Radio emission of highly inclined cosmicray air showers measured with LOPES. Proc. ICRC 2005, 2005.

[Prah71] J. H. Prah. M.Phil. thesis, University of London, 1971.

[Press92] W. H. Press et al. *Numerical Recipes.* Cambridge University Press, 1992.

[Rohlfs86] K. Rohlfs. *Tools of Radio Astronomy.* Springer Verlag, 1986.

[Saltzberg01] D. Saltzberg and P. Gorham. Radio Detection of High Energy Particles. In *AIP Conf. Proc. 579: Radio Detection of High Energy Particles*, 2001.

[Schieler95] H. Schieler. *Konzeption, Entwicklung und Test des lokalen Datenerfassungssystems für das strukturierte Detektor-Array von KASCADE.* PhD thesis, Universität Karlsruhe, 1995.

[Shaviv05] N. J. Shaviv. On climate response to changes in the cosmic ray flux and radiative budget. *Journal of Geophysical Research (Space Physics)*, 110:8105, August 2005.

[Spencer69] R. E. Spencer. *Nature*, 222:460, 1969.

[Spreeuw05] H. Spreeuw. Gain properties of the inner 25 antennae of Lofar's ITS. *ASTRON-Report*, 2005.

[Takeda99] M. Takeda, N. Hayashida, K. Honda, N. Inoue, K. Kadota, F. Kakimoto, K. Kamata, S. Kawaguchi, Y. Kawasaki, N. Kawasumi, E. Kusano, Y. Matsubara, K. Murakami, M. Nagano, D. Nishikawa, H. Ohoka, S. Osone, N. Sakaki, M. Sasaki, K. Shinozaki, N. Souma, M. Teshima, R. Torii, I. Tsushima, Y. Uchihori, T. Yamamoto, S. Yoshida, and H. Yoshii. Small-Scale Anisotropy of Cosmic Rays above 10^{19} eV Observed with the Akeno Giant Air Shower Array. *ApJ*, 522:225–237, September 1999.

[Ulrich05] H. Ulrich. *Untersuchungen zum primären Energiespektrum der kosmischen Strahlung im PeV-Bereich mit dem KASCADE-Experiment.* PhD thesis, Universität Karlsruhe, 2005.

[Watson06] A. A. Watson. The mass composition of cosmic rays above 10^{17}-ev. *Nucl. Phys. Proc. Suppl.*, 151:83–91, 2006.

[Wefel91] J. P. Wefel. Cosmic Rays, Supernovae and the interstellar Medium. volume 337 of *NATO ASIC Proc.*, page 29, 1991.

[Zatsepin66] G. T. Zatsepin and V. A. Kuzmin. *JETP Lett.*, 4, 1966.

Acknowledgements

Setting up an experiment like LOPES is always the work of many. Regardless how much a single person contributed to it, the work would not have been possible without the help of others. I like to thank:

- Heino Falcke, for inviting me to investigate a strange new (or old) way to look at old acquaintances of mine together with him. For all the help and suggestions, the discussions we had, and that he never lost faith even when I nearly did.
- Uli Klein, for all the things he taught me about radio astronomy, for the work of reviewing my thesis, and for always being welcome on his side of the "blue door".
- Anton Zensus for all the help and support I got while working on this thesis in his group at the MPIfR.
- Tim Huege, Elmar Körding and Andreas Brunthaler for the discussions and suggestions we had and entertaining me during boring office hours.
- Arno Witzel and the all the others of the VLBI group for the nice atmosphere in the group.
- Jürgen Moarwitz, Dion Kant, Gijs Schonderbeek, Yde Koopman, Harm-Jan Pepping, and all the others at the technical labs at ASTRON for teaching me about HF-electronics and the great work they did with the hardware we used.
- Reinhard Keller and the staff from the HF-lab at the MPIfR for the help with all the tiny details of assembling LOPES and for always being there when I had a question.
- Jan Kuijpers for bearing up with me while I finished my thesis.
- Christoph Böttner, Ylva Schubert, Claudia & Chrstian Brüns and all the other members of the Café RAIUB for all the pleasant breaks and the excited discussions about science, the world, and the human nature.
- Andreas Nigl, Sven Lafebre, Jelena Petrovic, Sijn Buitink, and the others at the astronomy group in Nijmegen for the nice reception.

- Harald Schieler, Andreas Haungs, Steffen Nehls, Andreas Weindl, Bernd Hoffmann and all the others at the Forschungszentrum Karlsruhe who helped with setting up and running LOPES
- All the secretaries and accountants, like Beate Naunheim, Cisca Custers, and Sylvia Mertens, without whom no science institute would work.
- The RegTP (even if they are now called differently) for their initial RFI survey.
- And my family who is always there for me even when I am being spleenish.